

UNIVERSITY OF CALIFORNIA

Los Angeles

Study and optimization of turbulence and transport in mirror configurations in the Large Plasma
Device

A dissertation submitted in partial satisfaction
of the requirements for the degree
Doctor of Philosophy in Physics and Astronomy

by

Philip N. Travis

2024

ABSTRACT OF THE DISSERTATION

Study and optimization of turbulence and transport in mirror configurations in the Large Plasma
Device

by

Philip N. Travis

Doctor of Philosophy in Physics and Astronomy
University of California, Los Angeles, 2024

Professor Troy Carter, Chair

Abstract

The dissertation of Philip N. Travis is approved.

Paulo Alves

Christoph Niemann

Jacob Bortnik

Troy Carter, Committee Chair

University of California, Los Angeles

2024

TABLE OF CONTENTS

1	Introduction	1
1.1	Nuclear fusion: brief introduction	2
1.1.1	Mirror machines as a faster way to fusion power	2
1.2	The Large Plasma Device at UCLA	2
1.2.1	Diagnostics at the LAPD	2
1.2.2	Data acquisition	2
1.3	Analysis techniques	2
1.3.1	Spectral analysis	2
1.3.2	Correlation techniques	2
1.3.3	Machine learning	2
2	Turbulence and transport in mirror geometries in the Large Plasma Device	3
2.1	Introduction	4
2.2	Device configuration	6
2.2.1	The Large Plasma Device (LAPD)	6
2.2.2	Diagnostics	7
2.3	Mirror-induced changes	11
2.3.1	Profile modification	11
2.3.2	Reduced particle flux	12
2.3.3	Compensating for the Te profile	21
2.3.4	Drift waves	25
2.3.5	Turbulence modification	29

2.3.6	Magnetic fluctuations	30
2.4	2d Structure	40
2.5	Discussion	45
2.5.1	Lack of mirror-driven instabilities	45
2.5.2	Instabilities driving turbulence	47
2.5.3	Causes of particle flux reduction	48
2.5.4	Differences between DR1 and DR2	51
2.6	Conclusions and future work	55
3	Optimizing mirror configurations in the LAPD using machine learning	56
3.1	Introduction	57
3.2	Data collection and processing	59
3.2.1	The Large Plasma Device (LAPD)	59
3.2.2	Data collection and processing of I_{sat} signals	61
3.2.3	Dataset distribution and bias	63
3.3	Model development, training	63
3.3.1	Initial training details	63
3.3.2	Baselines for mean-squared error	64
3.3.3	Effects of reducing the training set	64
3.3.4	Improving performance with machine state flags	66
3.4	Uncertainty quantification	67
3.4.1	β -NLL loss and learning rate scheduling	67
3.4.2	Cross-validation MSE	68
3.4.3	Model calibration via weight decay	68

3.5	Evaluating model performance	72
3.5.1	Checking geometrical intuition	72
3.5.2	Directly comparing prediction to measurement	74
3.6	Inferring trends	76
3.7	Optimizing profiles	79
3.8	Discussion	86
3.8.1	Key achievements	86
3.8.2	Current limitations	86
3.8.3	Future directions	87
3.9	Conclusion	88
3.10	The open dataset and repository	91
3.11	Data bias	91
3.12	Data and training pipeline validation	94
3.13	Effect of I_{sat} calibration	94
4	Reconstructing missing diagnostics using energy-based models	95
4.1	Brief introduction to energy-based models (EBMs)	95
4.2	Building a 15 million shot dataset	95
4.3	Training the model	97
4.4	Unconditional sampling	97
4.5	Reconstructing missing diagnostics via conditional sampling	97
4.6	Inferring trends and outlook	97
5	Conclusions	98

5.1 Future Directions	98
A 0D mirror optimization	99
A.1 List of assumptions / conditions	100
A.2 User specified parameters	101
A.2.1 Simple mirror endplug	101
A.2.2 Tandem mirror	102
A.2.3 Engineering parameters	102
A.3 Fusion	103
A.3.1 Reactivity	103
A.3.2 Fusion power	104
A.4 General formulae	107
A.5 Radial particle transport	109
A.5.1 Classical diffusion	110
A.5.2 Bohm diffusion	110
A.5.3 Gyro-Bohm diffusion	111
A.5.4 ETG-driven transport	111
A.6 Mirror-specific derived quantities	112
A.6.1 Temperatures and confinement time in a beam-heated mirror from Egedal et al 2022 [?]	112
A.6.2 Confinement time given by classical transport	114
A.6.3 End Cells/Plugs	115
A.6.4 Tandem mirror central cell	119
A.6.5 Overall power balance and plant power estimates	121

A.6.6	Instabilities	122
A.7	Costs and economics	123
A.7.1	Heating	123
A.7.2	Magnets	123
A.8	Optimization constraints	124
A.8.1	Midplane fields regularization via alpha particle confinement penalties . .	124
A.8.2	Kunal’s suggestions	125
A.9	Optimizing mirror configurations	126
A.9.1	Gradient descent using SymPy and JAX	126
A.9.2	Example: optimizing Q in a simple mirror	127
B	Automated Langmuir sweep analysis using machine learning	131
C	Wisdom acquired	132
References	133

LIST OF FIGURES

2.1	Cartoon of the Large Plasma Device and the coordinate system used. Only four of the eleven mirror configurations studied are plotted for clarity (mirrors of the same length have similar shapes and simply scale with mirror ratio). Diagnostic set varied by datarun; unlabeled diagnostics were used in both dataruns.	7
2.2	Raw data and basic processing steps for LAPD probe diagnostics as demonstrated by an I_{sat} trace from a DR1, $M = 1$ mirror at 26 cm. Data are truncated from 4.8 to 11.2 ms (a) and detrended (b). Power spectral density is calculated (c), and a power profiles can be constructed (d). The shaded regions are excluded from this analysis.	9
2.3	Shot-to-shot variation of I_{sat} profiles	12
2.4	Midplane I_{sat} profile, shot-averaged and time-averaged from 4.8 to 11.2 ms (assumed of $T_e = 4.5$ eV based on triple probe and Langmuir sweep measurements). Effective area was calibrated using a nearby interferometer. Profile shape remains similar in the core and gradient region when mapped to the cathode radius x_c . The dips in profiles at higher M below $x = x_{\text{PF}}$ are of unknown origin and are not the focus of this study. Shot-to-shot variation is less than 5% for $x \leq 0.95x_c$ and less than 9% for $x \leq 1.4x_c$ for all cases.	13
2.5	Line-integrated density as measured by a 56 GHz heterodyne interferometer as a function of mirror ratio, taken from four discharges for each mirror configuration. Density increases up to a mirror ratio of 2.3 where it appears to level off. The interferometer is located in the mirror cell bad-curvature region at 9.59m, 1.3m closer to the cathode from the midplane.	14

2.6	T_e from Langmuir sweeps (DR2) at the midplane. Triple probe results are nearly identical. The increased temperatures directly at the plasma edge, indicated by dotted portions of the curves, are likely artifacts caused by sheath expansion in lower densities. Changes in mirror ratio lead to at most 25% change in T_e . The plasma is collisional and isotropic.	15
2.7	Plasma potential (a) and derived $\mathbf{E} \times \mathbf{B}$ velocity profiles (b) from Langmuir sweeps at the midplane. $x/x_c > 1.2$ has been excluded from the graph for greater clarity in the core and gradient region. The electric field was calculated by taking the gradient of the spline-smoothed plasma potential profile. The Mach number (in percent) is calculated using the approximate sound speed evaluated at $x = x_{PF}$ (tab. 2.2). The overall structure of the flows does not appreciably change when mirror ratio is varied.	16
2.8	I_{sat} (a) and B_{\perp} (b) fluctuation power profiles for signals 2 kHz and up at $z=8.3\text{m}$ (mid-plane) and $z=7.7\text{m}$, respectively. The lower frequency components in I_{sat} are associated with bulk profile evolution, dominate the core region, and are not the focus of this study.	18
2.9	Cross-field, $\tilde{\mathbf{E}} \times \mathbf{B}$ fluctuation-based particle flux (calculated using eq. 2.1) with respect to mirror ratio. A monotonic decrease in particle flux is observed with increasing mirror ratio at the midplane. Particle flux is normalized by plasma circumference to the $M = 1$ case to account for the geometry-induced decrease in particle flux caused by a larger-diameter plasma.	19
2.10	Phase (a) and coherency (b) of I_{sat} current and Vf near x_{PF} at the midplane, smoothed. Positive phase means I_{sat} leads Vf. Peaks in coherency occur between 3-5 kHz and at the drift-Alvén wave peaks between 12 and 25 kHz. These coherency peaks tend to have larger phase shifts than other nearby frequencies.	20
2.11	Swept vs triple probe measurements	22
2.12	Triple probe Te and Te fluctuation profiles	22

2.13	Diffusivity relative to D_B	23
2.14	Diffusivity with T_e compensation relative to D_B	24
2.15	I_{sat} gradients under varying profile smoothing methods	24
2.16	I_{sat} (density) fluctuation power averaged over a 1 cm region around x_{PF} at the midplane. The fluctuation power is largely featureless below 2 kHz and beyond 40 kHz aside from electronics noise.	25
2.17	k_{\parallel} (a) and coherency γ (b) as a function of frequency. Only results from the $M = 1$ case are available, but it is clear that there are long ($\gtrsim 34$ m) wavelength modes at 3 and 12 kHz. The probes used for calculating k_{\parallel} were located at the midplane ($z=8.31$) and $z=12.14$ m, 3.83 m apart.	26
2.18	Normalized density fluctuations vs ρ_s/L_n	27
2.19	I_{sat} scaled by L_n^2/n^2	28
2.20	Fluctuation power summed for each k_y for frequencies up to 100 kHz, smoothed. The contribution to fluctuation power is negligible past 100 kHz. The fluctuation power decreases substantially when a mirror configuration is introduced, but no trend is seen otherwise and the k_y spectra remain exponential. Note the logarithmic scale.	29
2.21	B_{\perp} fluctuation power averaged at the core from 0 to 3 cm (a) and around the peak fluctuation point ($x \sim x_{PF}$) (b). Fluctuation power decreases across the board with mirror ratio except for core frequencies close to Ω_{ci} . Peaks around 10 – 30 kHz at x_{PF} are consistent (region 2) with drift-Alfvén waves and the near-cyclotron frequency features in the core may be resonating Alfvén waves created by the magnetic mirror. Frequencies below 2 kHz and dominated by instrumentation noise and thus excluded.	31
2.22	B_{\perp} fluctuation power profiles for the three regions shown in fig. 2.21: region 1 (6 kHz) (a), region 2 where frequencies are taken from the peaks of the drift-Alfvén waves for each mirror ratio (b), and region 3 (114 kHz) (c).	33

2.23 Summed fluctuation power of B_{\perp} in the core ($x/x_c \leq 0.3$) as a function of mirror length and ratio. Top (a): the fluctuation power is normalized by the sum of the full-spectrum summed power. Bottom(b): the frequency of the power distribution > 50 kHz weighted by the fluctuation power.	34
2.24 B_{\perp} , flat field 500G vs 400G	35
2.25 B_{\perp} fluctuations at $x=0$ for different mirror lengths	36
2.26 B_z fluctuations in the core and x_{PF}	37
2.27 B_{\perp} fluctuation power profiles for low frequencies	38
2.28 B_z fluctuation power profiles for low frequencies	39
2.29 Perpendicular magnetic field and the derived current density for the flat-field ($M = 1$) case using a Bdot probe with an axially-separated I_{sat} reference (DR2). The x-y plane was centered near x_{PF}	41
2.30 Perpendicular magnetic field and the derived current density for the $M = 1.9$ and $M = 2.68$ cases computed in the same manner as fig. 2.29. The x-y planes were centered near x_{PF} , and the view size was kept constant across the plots. The structure is much less obvious in the mirror cases, but all exhibit the expected Alfvèn wave pattern . . .	42
2.31 Azimuthal mode number m amplitudes calculated from two axially-separated, correlated, I_{sat} probes. Increasing mirror ratio (a to e) leads to increased m at higher frequencies. (DR2)	43
2.32 k_y averaged about x_{PF} and smoothed for each mirror ratio calculated using two vertically-separated Vf tips on the same probe. Little change is seen in k_y at lower frequencies but higher frequencies tend towards larger k_y at higher mirror ratios.	44
2.33 Gradient scale length L_n and the associated term in the drift wave growth rate L_n^{-2} . This scale length was calculated over a 3 cm region around x_{PF} (peak fluctuation region) at the midplane. Increasing the mirror ratio increases the gradient scale length, which suggests weakening of the underlying instability driver.	48

2.34	Particle flux: breakdown into components	49
2.35	I_{sat} decorrelation time	50
2.36	ExB shearing rate	51
2.37	Discharge power vs mirror ratio	52
2.38	I_{sat} profiles (M=1), DR1 vs DR2	53
2.39	Line integrated density, DR1 vs DR2	53
2.40	I_{sat} calibration factor over runs	54
3.1	size=12	60
3.2	size=12	70
3.3	size=12	71
3.4	size=12	73
3.5	size=12	75
3.6	size=12	77
3.7	size=12	78
3.8	size=12	80
3.9	size=12	84
3.10	size=12	89
3.11	size=12	90
3.12	size=12	92
A.1	DT reactivities	104
A.2	DD reactivities	105
A.3	DT, DD, and D-He3 reactivity comparison	105
A.4	Simple mirror: cost function and gradient magnitude for each step	128

A.5	Simple mirror: magnetic fields for each step	129
A.6	Simple mirror: fusion power and Q for each step	129
A.7	Simple mirror: temperatures for each step	130

LIST OF TABLES

2.1	Magnetic mirror lengths and ratios. The lengths are measured where the curvature changes sign and the ratio is the maximum divided by the minimum. Approximately 3.5m must be added to the length if the good-curvature region is included. In the case of small asymmetries, the field strengths were averaged before calculation of the mirror ratio.	8
2.2	LAPD machine information and plasma parameters in the core and peak-fluctuation region ($x = x_{PF}$) at the midplane in this study. Dashed quantities are assumed to be identical to core quantities.	10
2.3	x_c and x_{PF} locations for each mirror ratio when scaled by the expected magnetic expansion.	11
3.1	Summary of test set losses for different training data and ensembles	65
3.2	Machine inputs and actuators for model inference	81
3.3	Machine inputs and actuators for optimized axial profiles	83
3.4	Data breakdown by class and dataset (percent)	93

ACKNOWLEDGMENTS

I acknowledge peeps

VITA

- 2017 B.S. (Engineering Physics), University of Illinois at Urbana-Champaign
- 2018 Masters (Physics), University of California, Los Angeles
- 2024 Ph.D. (Plasma Physics), University of California, Los Angeles

PUBLICATIONS

Pubs

CHAPTER 1

Introduction

1.1 Nuclear fusion: brief introduction

1.1.1 Mirror machines as a faster way to fusion power

1.2 The Large Plasma Device at UCLA

1.2.1 Diagnostics at the LAPD

1.2.1.1 Langmuir probes: I_{sat} , sweeps, triple probes

1.2.1.2 The 288 GHz heterodyne interferometer

1.2.1.3 Thomson scattering

1.2.1.4 Fast framing camera

1.2.2 Data acquisition

1.3 Analysis techniques

1.3.1 Spectral analysis

1.3.2 Correlation techniques

1.3.3 Machine learning

1.3.3.1 Neural networks

CHAPTER 2

Turbulence and transport in mirror geometries in the Large Plasma Device

Thanks to advances in plasma science and enabling technology, mirror machines are being reconsidered for fusion power plants and as possible fusion volumetric neutron sources. However cross-field transport and turbulence in mirrors remains relatively understudied compared to toroidal devices. Turbulence and transport in mirror configurations were studied utilizing the flexible magnetic geometry of the Large Plasma Device (LAPD). Multiple mirror ratios from $M = 1$ to $M = 2.68$ and three mirror-cell lengths from $L = 3.51\text{m}$ to $L = 10.86\text{m}$ were examined. Langmuir and magnetic probes were used to measure profiles of density, temperature, potential, and magnetic field. The fluctuation-driven $\tilde{E} \times B$ particle flux was calculated from these quantities. Two probe correlation techniques were used to infer wavenumbers and two-dimensional structure. Cross-field particle flux and density fluctuation power decreased with increased mirror ratio. Core density and temperatures remain similar with mirror ratio, but radial line-integrated density increased. The physical expansion of the plasma in the mirror cell by using a higher field in the source region may have led to reduced density fluctuation power through the increased gradient scale length. This increased scale length reduced the growth rate and saturation level of rotational interchange and drift-like instabilities. Despite the introduction of magnetic curvature, no evidence of mirror driven instabilities interchange, velocity space, or otherwise were observed. For curvature-induced interchange, many possible stabilization mechanisms were present, suppressing the visibility of the instability.

2.1 Introduction

Historically, mirror research has prioritized the main issues with mirror confinement: stabilizing the interchange instability, stabilizing velocity-space (loss-cone-driven) instabilities, and minimizing axial electron heat losses. Nevertheless cross-field transport remains an important topic in magnetic-confinement fusion reactor development, in both linear and toroidal geometries. Insight into edge-relevant turbulence, and its coupling to interchange and other mirror-driven instabilities, performed in a basic plasma science device may be useful for a mirror-based reactor. Although not at fusion-relevant core temperatures or densities, the Large Plasma Device (LAPD) operates at conditions similar to the edge of fusion devices and can provide insight into the physical processes in that region. Mirror machines are once again rising in prominence as a candidate for commercial fusion reactors with the advent of highly-funded commercial ventures and high-field high-temperature superconducting magnets [EAB23, FAE24], so development of a functional understanding of cross-field transport in mirrors is imperative. A characterization of edge fluctuations has been undertaken, with emphasis on interpreting these fluctuations within the context of mirror.

Non-classical cross-field particle transport is often caused by low-frequency, large-amplitude fluctuations. These fluctuations are the result of various instabilities. One such process is the "universal" drift instability, which appears in the presence of a density gradient and finite resistivity. Drift wave turbulence and the effect on transport has been extensively studied in the past [Hor99, TFM09]. In the presence of sufficiently high rotation or sheared flow, rotational interchange and the Kelvin-Helmholtz instabilities also contribute or couple to these fluctuations.

Various gradient-, rotation-, and shear-driven instabilities (and suppression of such) have been studied previously in the LAPD experimentally [SCR12, SCR13, Sch13] and in simulations using BOUT, a 3d fluid turbulence code, and an eigenvalue solver [PUC10]. The LAPD has a sufficiently high spontaneous rotation rate that rotation-driven instabilities may be excited without artificial drive. Simulations using BOUT++ [FCU13] have also suggested that a rapidly growing nonlinear instability may dominate over all other linear instabilities.

Imposing a magnetic mirror configuration introduces magnetic curvature. The alignment of the curvature vector with a pressure gradient vector component causes the flute-like interchange instability if no stabilization mechanism is present. This interchange mode could couple to finite k_{\parallel} drift waves. The coupling of drift waves to curvature-induced interchange modes has been studied in toroidal devices such as TORPEX [PBD06, FLM06], where curvature was seen as the driving component for the unstable drift-interchange modes. Drift-like fluctuations have also been observed in the GAMMA-10 mirror [MII91, YMM10]. Flute-like modes and drift waves have been studied in other linear devices, such as Mirabelle [BGB05], where the appearance of flute-like modes or drift waves were controlled by varying the field and limiter diameter.

The rotational interchange and curvature interchange can both be flute-like modes. Rotational interchange (also called the “centrifugal instability”) is driven by the aligned centrifugal force and pressure gradient vectors, but curvature-driven interchange is instead driven by magnetic curvature and is typically referred to as simply the “flute” or “interchange” instability. Rotational interchange [Jas72] has been observed in the LAPD in the past [SCR12, Sch13], and the curvature-driven interchange instability has been observed in many other mirror machines [WV82, FWD83, Pos87].

Biassing or modifying the electrical connection of the plasma with the end wall has proven to be an important actuator in many mirror machines such as TMX-U [HBF84], GAMMA-10 [MII91], and GDT [BLZ03, BBS07, BBC10], and will be utilized on WHAM [EAB23]. Active biassing was not attempted in this study, but the intrinsic rotation and strong electrical connection to the source region may provide a useful analog for edge biassing in other mirror machines.

The LAPD exhibits a high degree of turbulence so it is difficult to identify the dispersion relation of the modes that are present. Nevertheless, the LAPD has good coverage of perpendicular spectra using correlation-plane techniques, and some measure of parallel spectra using the correlation between two axially-separated probes. A space-time spectral characterization of the many instabilities present in this low beta, moderate aspect ratio, gas-dynamic trap regime is attempted.

This goal of this study was to investigate the changes to turbulence and transport in LAPD mirror configurations. Of particular interest were the potential coupling of the interchange instability

with drift waves or other modes, and the effect of the mirror geometry on cross-field particle flux. Presented is a characterization of the observed modes and the effect of introducing a mirror geometry. This paper is organized as follows. Sec. 2.2 discusses the configuration of the LAPD and the diagnostics used. Sec. 2.3 covers the changes seen when imposing a magnetic mirror configuration on profiles, particle flux, drift waves, turbulence, and magnetic fluctuations. Sec. 2.4 explores the changes in 2d (x-y plane) structure. Sec. 3.8 discusses the active and expected instabilities and reasons for their modification. Sec. 3.9 summarizes the study and discusses the requirements for a deeper investigation.

2.2 Device configuration

2.2.1 The Large Plasma Device (LAPD)

The Large Plasma Device (LAPD) is a 20 meter long, 1 meter diameter basic plasma device at UCLA [GPL16]. The LAPD has a variable magnetic field, from 250G to 1.6 kG and can be varied axially. Probes inserted into the plasma can collect high-resolution, temporal information on density, temperature, potential, and magnetic field fluctuations. In this study, the plasma was formed using an emissive, 72 cm diameter barium-oxide (BaO) cathode (mapped to 60 cm in a flat field) and a 72 cm diameter, 50% transparent molybdenum anode that accelerate electrons across a configurable 40 – 70V potential; voltages of 60 and 63V were used in this study. The source has since been upgraded to a lanthanum hexaboride (LaB₆) cathode [QGP23] that enables access to higher-density, higher-temperature regimes, but all the data in this study are from plasma formed by a BaO cathode.

The flexible magnetic geometry of the LAPD was used to construct a variety of magnetic mirror configurations. The discharge current, fill pressure, and other machine parameters were held constant. The typical plasma parameters observed in this study can be seen in table 2.2. Data in several mirror ratios and lengths were collected (see table 2.1) but emphasis is placed on the short cell because the highest mirror ratio possible ($M = 2.68$) with a 500 Gauss midplane field

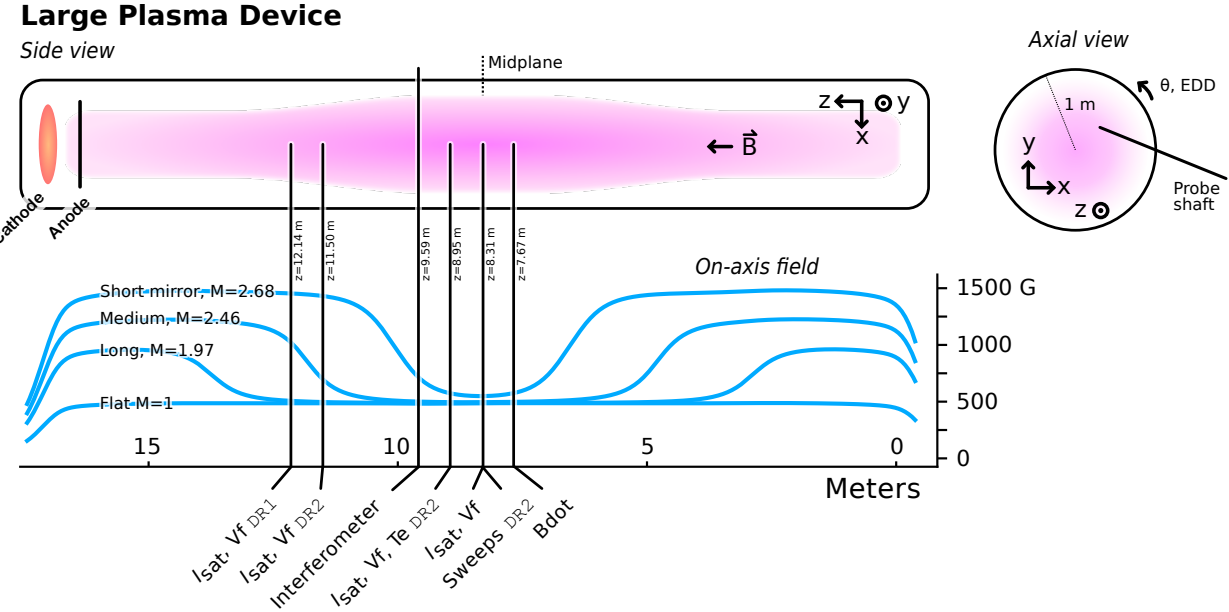


Figure 2.1: Cartoon of the Large Plasma Device and the coordinate system used. Only four of the eleven mirror configurations studied are plotted for clarity (mirrors of the same length have similar shapes and simply scale with mirror ratio). Diagnostic set varied by datarun; unlabeled diagnostics were used in both dataruns.

could be accessed and probes were able to be placed outside of the mirror cell. An overview of the axial magnetic field for the the short mirror configurations and probe locations can be seen in fig. 2.1. 2- or 3-cell mirror configurations were also explored but are not examined in this study. All results presented below are from the short mirror cell configuration unless otherwise specified.

2.2.2 Diagnostics

All diagnostics were recorded with a effective sampling rate of 6.25 MHz (16-sample average at 100 MSPS) and a spatial resolution of 0.5 cm. When necessary, averaging over time is done in the approximate steady-state period of the plasma discharge (4.8 to 11.2 ms from the 1 kA trigger signal). Unless otherwise noted, all data presented will be from probes inside the mirror region ($z \approx 7\text{m}$). An example of a raw I_{sat} signal and processing steps can be seen in fig. 2.2. The raw

Mirror length	Mirror ratios (M)
Flat	1
3.51 m (short)	1.47 1.90 2.30 2.68
7.03 m (medium)	1.49 1.98 2.46
10.86 m (long)	1.47 1.97 2.44

Table 2.1: Magnetic mirror lengths and ratios. The lengths are measured where the curvature changes sign and the ratio is the maximum divided by the minimum. Approximately 3.5m must be added to the length if the good-curvature region is included. In the case of small asymmetries, the field strengths were averaged before calculation of the mirror ratio.

signals are detrended by subtracting the mean across shots to obtain the fluctuations only. FFTs are then taken of these fluctuations for calculating power spectra and cross-correlated quantities. Frequencies above 200 kHz are dominated by electronics and instrumentation noise and thus are also ignored. Fluctuation power profiles can then be constructed.

The data presented were collected in two phases. The first phase ("datarun"), DR1, collected Langmuir probe (I_{sat} and V_f) and magnetic fluctuation ("Bdot") [EPC09] traces. 50 shots were taken at each position for every configuration. The second phase, DR2, was conducted with a similar set of diagnostics focused on temperature measurements (swept and triple probe) and 2d x-y structure. 15 shots were taken at each position, except for Langmuir sweeps with 64 shots. When appropriate, all data for each position were shot-averaged. " I_{sat} " will be used interchangeably with "density" and be presented with units of density (assuming a flat $T_e = 4.5$ eV profile).

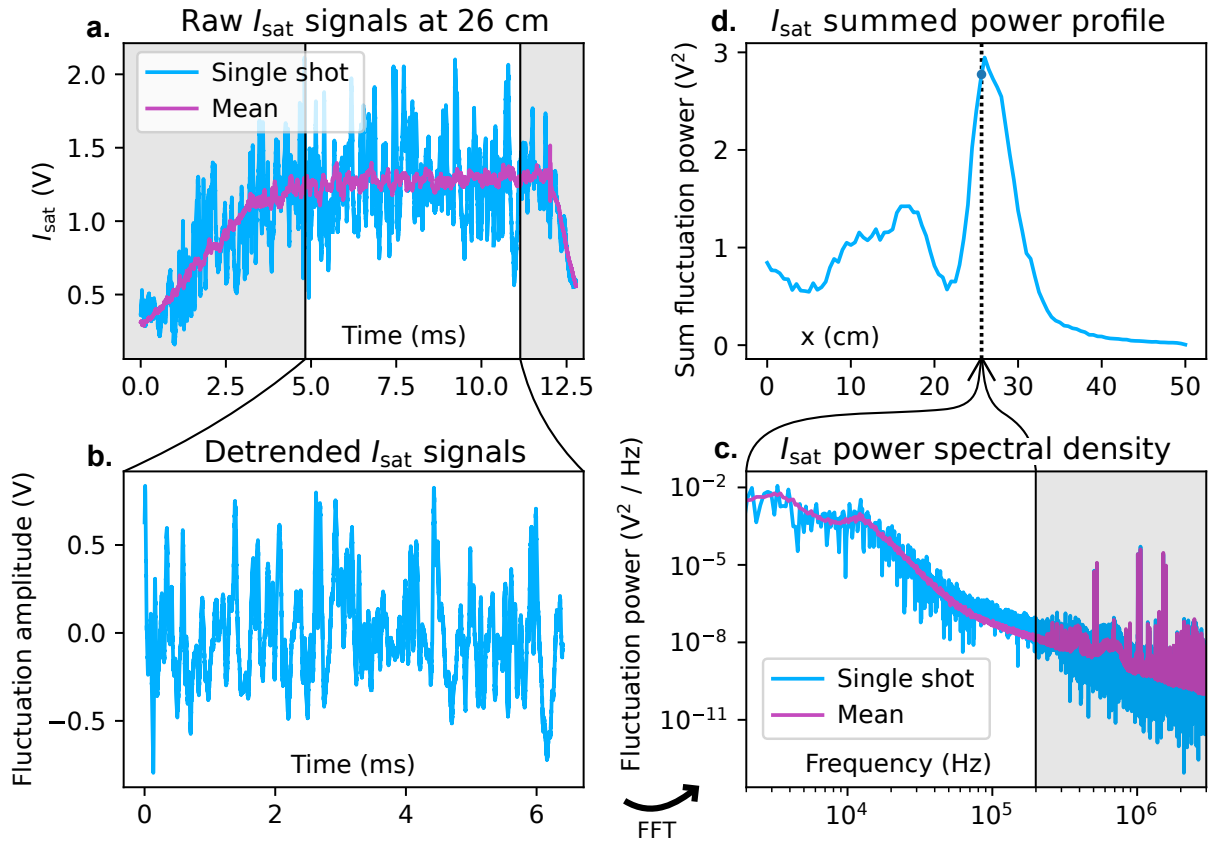


Figure 2.2: Raw data and basic processing steps for LAPD probe diagnostics as demonstrated by an I_{sat} trace from a DR1, $M = 1$ mirror at 26 cm. Data are truncated from 4.8 to 11.2 ms (a) and detrended (b). Power spectral density is calculated (c), and a power profiles can be constructed (d). The shaded regions are excluded from this analysis.

Cathode radius (M=1)	x_c	30	cm
Machine radius	R	50	cm
Plasma length	L	~ 17	m
Primary species		He-4 1+	
Electron-helium mass ratio		1.37×10^{-4}	
Neutral pressure		$6 - 20 \times 10^{-5}$	Torr
Quantity		Core	$x = x_{\text{PF}}$
Density	n_e	1.25×10^{12}	0.6×10^{12} cm $^{-3}$
Ion temperature	T_i	~ 1	eV
Electron temperature	T_e	4	5
Beta (total)	β	9×10^{-4}	6×10^{-4}
Midplane magnetic field	B_{mid}	500	G
Plasma freq	Ω_{pe}	10	7.1
Ion cyclotron freq	Ω_{ci}	200	kHz
Electron cyclotron freq	Ω_{ce}	1.4	GHz
Debye length	λ_D	0.013	0.021
Electron skin depth	λ_e	30	43
Ion gyroradius	λ_{ci}	5.8	mm
Electron gyroradius	λ_{ce}	0.13	0.15
Ion thermal velocity	\bar{v}_i	6.94	km/s
Electron thermal velocity	\bar{v}_e	1190	1330
Sound speed	c_s	13.0	13.9
Alfvén speed	v_a	446 – 1140	-1620
Ion sound radius	ρ_s	65	69
Ion-ion collision freq	ν_{ii}	730	380
Electron-ion collision freq	ν_{ei}	6.77	2.59
Electron collision freq	ν_{ee}	9.57	3.66
Ion mean free path	$\lambda_{i,\text{mfp}}$	26	50
Electron mean free path	$\lambda_{e,\text{mfp}}$	$10^{10} 175$	512
Spitzer resistivity	η	192	$\mu\Omega \text{ m}$

Table 2.2: LAPD machine information and plasma parameters in the core and peak-fluctuation

Mirror ratio	1	1.47	1.90	2.30	2.68
Scale factor	1	1.21	1.38	1.52	1.64
x_c (cm)	30	36	41	45	49
x_{PF} (cm)	26	32	36	40	43

Table 2.3: x_c and x_{PF} locations for each mirror ratio when scaled by the expected magnetic expansion.

2.3 Mirror-induced changes

2.3.1 Profile modification

Because the field at the plasma source increases with M , the midplane plasma expands by a factor of \sqrt{M} . The physical locations of the peak fluctuation region – x_{PF} (maximum gradient) – and the cathode radius x_c can be seen in tab. 2.3. This expansion leads to broader plasma profiles and decreased core density but are similar in the core and at x_{PF} when magnetically-mapped to the cathode radius x_c as seen in fig. 2.4. Dips between the core ($x/x_c = 0$) and the peak fluctuation region ($x = x_{PF}$) are seen, but fluctuation power from this region ($x/x_c = 0.5$ to 0.7) is not significant (fig. 2.8) so this region is not the focus of this study. The line-integrated density as measured by a 56 GHz heterodyne interferometer increases up to $\sim 35\%$ from the M=1 case of $\approx 8 \times 10^{13} \text{ cm}^{-2}$ (fig. 2.5) but does not increase past a mirror ratio of 2.3.

The error of on the I_{sat} profiles as represented by the standard deviation (scaled by the time-averaged profiles) can be seen in fig. 2.3. The error is relatively small and should not play a factor in our analysis – rarely are differences between quantities of the different mirror ratios that small.

Discharge power increases only slightly (3%) at higher mirror ratios suggesting negligible impact on density. Langmuir sweeps and triple probe measurements of T_e (DR2) show slightly (less than 25%) depressed core and slightly elevated edge T_e with increasing mirror ratio (fig. 2.6) but otherwise remains unaffected. The temperature affects I_{sat} measurements through the $\sqrt{T_e}$ term so

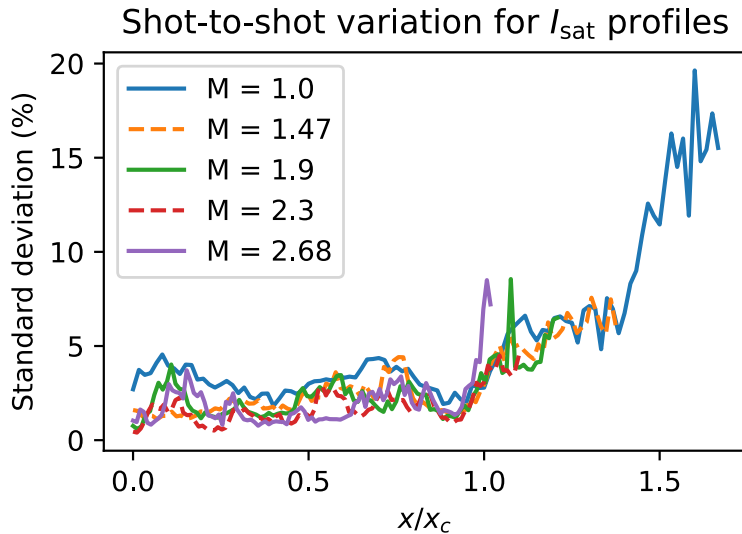


Figure 2.3: Shot-to-shot variation of I_{sat} profiles

small changes are insignificant. The low temperatures indicate that the plasma is collisional given the length scales of the system (as seen in table 2.2) and isotropic. Plasma potential decreases across the plasma (fig. 2.7) when the mirror ratio exceeds 1.9. This drop in plasma potential may be caused by the grounding of the anode to the wall, which should begin at $M = 1.93$ given the 72 cm anode and 100 cm vessel diameters. The reason for the local minimum in the $M=2.68$ is unknown. This potential profile creates a sheared $\mathbf{E} \times \mathbf{B}$ velocity profile (fig. 2.7) limited to 500 m/s in the core and exceeding ~ 3 km/s at the far edge. The flow does not exceed 4% of the sound speed (tab. 2.2) in the core or gradient ($x = x_{PF}$) region. The mirror ratio does not appear to significantly alter azimuthal flow. The floating potential (V_f) profile also exhibits similar behavior to the plasma potential (fig. 2.7), but is modified by the presence of primary electrons.

2.3.2 Reduced particle flux

The density fluctuation power peaks at the steepest gradient region ($x_{PF} = x/x_c \sim 0.88$) as expected as seen in fig. 2.8. x_{PF} occurs at nearly the same magnetically-mapped coordinate for each mirror

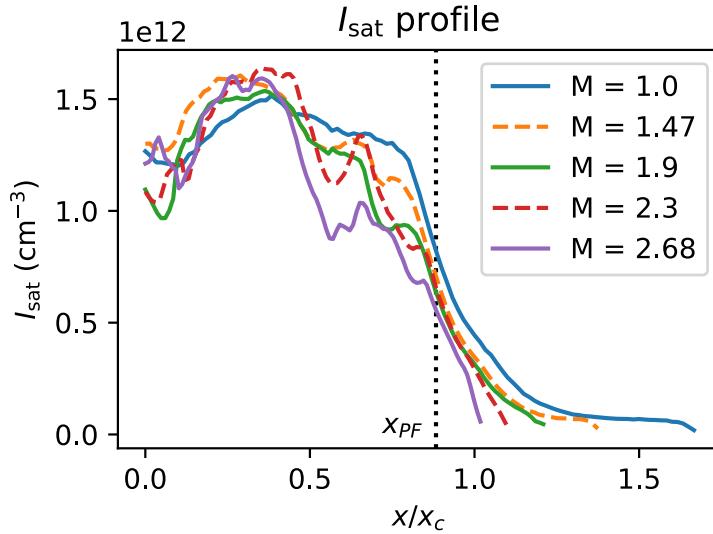


Figure 2.4: Midplane I_{sat} profile, shot-averaged and time-averaged from 4.8 to 11.2 ms (assumed of $T_e = 4.5$ eV based on triple probe and Langmuir sweep measurements). Effective area was calibrated using a nearby interferometer. Profile shape remains similar in the core and gradient region when mapped to the cathode radius x_c . The dips in profiles at higher M below $x = x_{PF}$ are of unknown origin and are not the focus of this study. Shot-to-shot variation is less than 5% for $x \leq 0.95x_c$ and less than 9% for $x \leq 1.4x_c$ for all cases.

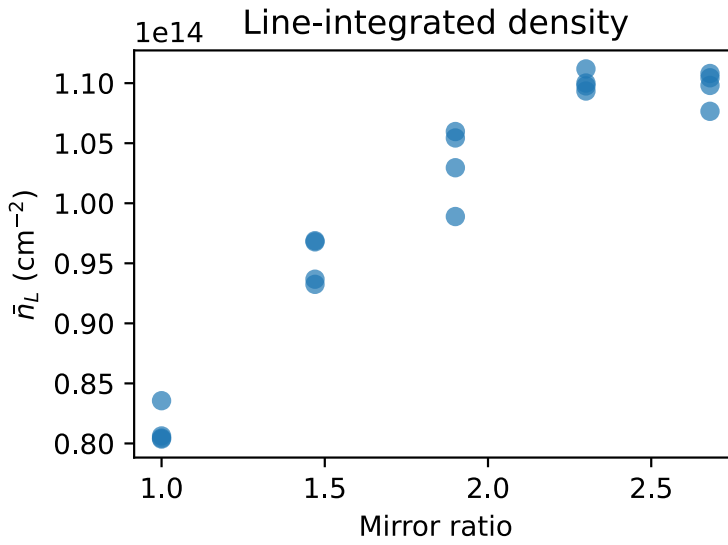


Figure 2.5: Line-integrated density as measured by a 56 GHz heterodyne interferometer as a function of mirror ratio, taken from four discharges for each mirror configuration. Density increases up to a mirror ratio of 2.3 where it appears to level off. The interferometer is located in the mirror cell bad-curvature region at 9.59m, 1.3m closer to the cathode from the midplane.

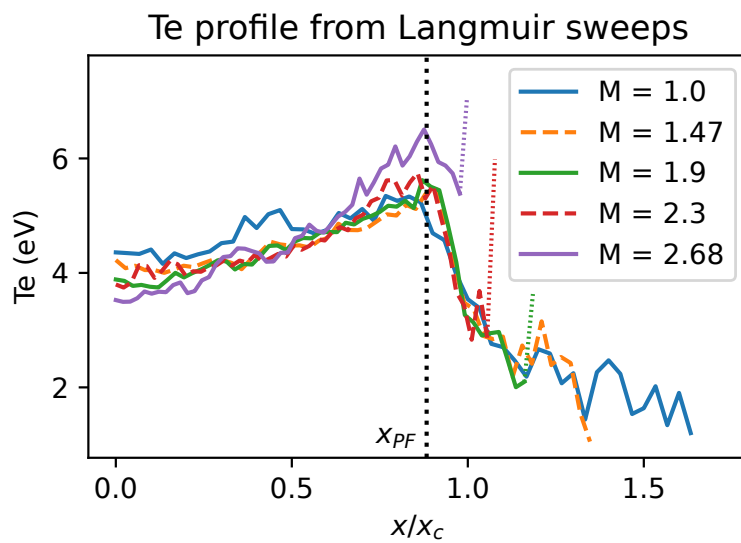


Figure 2.6: T_e from Langmuir sweeps (DR2) at the midplane. Triple probe results are nearly identical. The increased temperatures directly at the plasma edge, indicated by dotted portions of the curves, are likely artifacts caused by sheath expansion in lower densities. Changes in mirror ratio lead to at most 25% change in T_e . The plasma is collisional and isotropic.

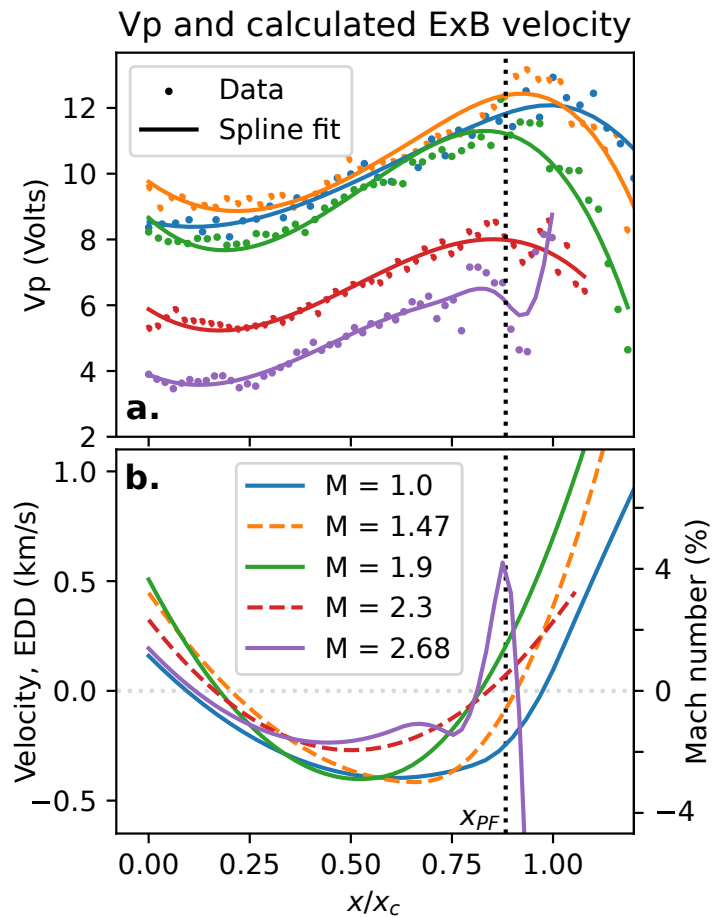


Figure 2.7: Plasma potential (a) and derived $\mathbf{E} \times \mathbf{B}$ velocity profiles (b) from Langmuir sweeps at the midplane. $x/x_c > 1.2$ has been excluded from the graph for greater clarity in the core and gradient region. The electric field was calculated by taking the gradient of the spline-smoothed plasma potential profile. The Mach number (in percent) is calculated using the approximate sound speed evaluated at $x = x_{PF}$ (tab. 2.2). The overall structure of the flows does not appreciably change when mirror ratio is varied.

ratio. These density fluctuations are a large driver of changes in the cross-field particle flux (eq. 2.1). Vf fluctuations also peak at the same location, but the total power across mirror ratios are similar and, relative to density fluctuations, much lower in the core. Core density fluctuations below 2 kHz are substantial in the core at lower mirror ratios, possibly caused by hollow profiles, nonuniform cathode emissivity, or probe perturbations, but are outside the scope of this study.

A spectral decomposition technique is used to calculate the time-averaged particle flux [Pow74] as seen in fig. 2.9:

$$\Gamma_{\tilde{E} \times B} = \langle \tilde{n} \tilde{v} \rangle = \frac{2}{B} \int_0^{\infty} k(\omega) \gamma_{n\phi}(\omega) \sin(\alpha_{n\phi}) \sqrt{P_{nn}(\omega) P_{\phi\phi}(\omega)} d\omega \quad (2.1)$$

where k is the azimuthal wavenumber, γ is the coherency, α is the cross-phase, and P the power spectrum. This method is more robust than the naive time-integration of $n(t)\tilde{E}(t)$ because it accounts for the coherency of the density-potential fluctuations. This representation also enables inspection of each contributing term in the event of surprising or problematic results. A plot of the I_{sat} -Vf phase can be seen in fig. 2.10. The flattened particle flux in the core is likely caused by primary electrons emitted by the cathode. These electrons have long mean free paths (greater than a few meters) and sample fluctuations along the length of the machine, mixing the phases of these fluctuations. Since floating potential is set by the hotter electron population, the measured Vf fluctuations are no longer related to the local plasma potential fluctuations of a wave by bulk T_e [CM09]. These primary electrons have a significant effect in the core within the region mapped to the cathode $x \lesssim x_c$. I_{sat} fluctuations are not affected.

Azimuthal wave number is measured by two Vf probe tips 0.5 cm apart. This wavenumber estimation technique yields good agreement with correlation plane measurements (fig. 2.31). Note that \tilde{E} is not directly measured – it is instead calculated through the $k(\omega)\sqrt{P_{\phi\phi}(\omega)}$ terms. The $\tilde{E} \times B$ particle flux clearly decreases with mirror ratio; most of this decrease is attributed to the decrease in density fluctuation power. The particle flux for each mirror ratio was normalized to the $M = 1$ case via the plasma circumference to compensate for the increased plasma surface area at the same magnetically-mapped coordinate x/x_c . This particle flux is on the order of Bohm diffusion $D_B = \frac{1}{16} \frac{T_e}{B} \approx 6.25 \text{ m}^2 \text{s}^{-1}$ as observed in other transport studies [MCT07].

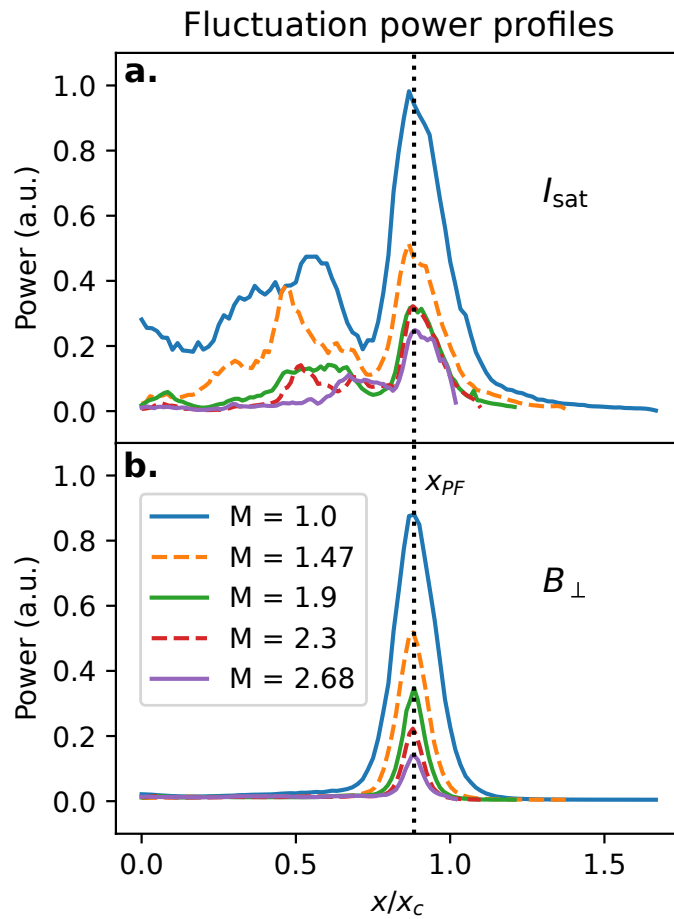


Figure 2.8: I_{sat} (a) and B_{\perp} (b) fluctuation power profiles for signals 2 kHz and up at $z=8.3\text{m}$ (midplane) and $z=7.7\text{m}$, respectively. The lower frequency components in I_{sat} are associated with bulk profile evolution, dominate the core region, and are not the focus of this study.

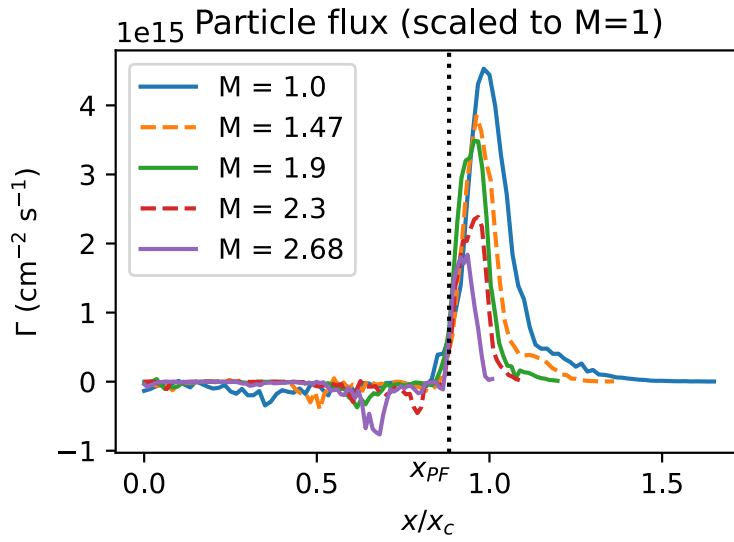


Figure 2.9: Cross-field, $\tilde{E} \times B$ fluctuation-based particle flux (calculated using eq. 2.1) with respect to mirror ratio. A monotonic decrease in particle flux is observed with increasing mirror ratio at the midplane. Particle flux is normalized by plasma circumference to the $M = 1$ case to account for the geometry-induced decrease in particle flux caused by a larger-diameter plasma.

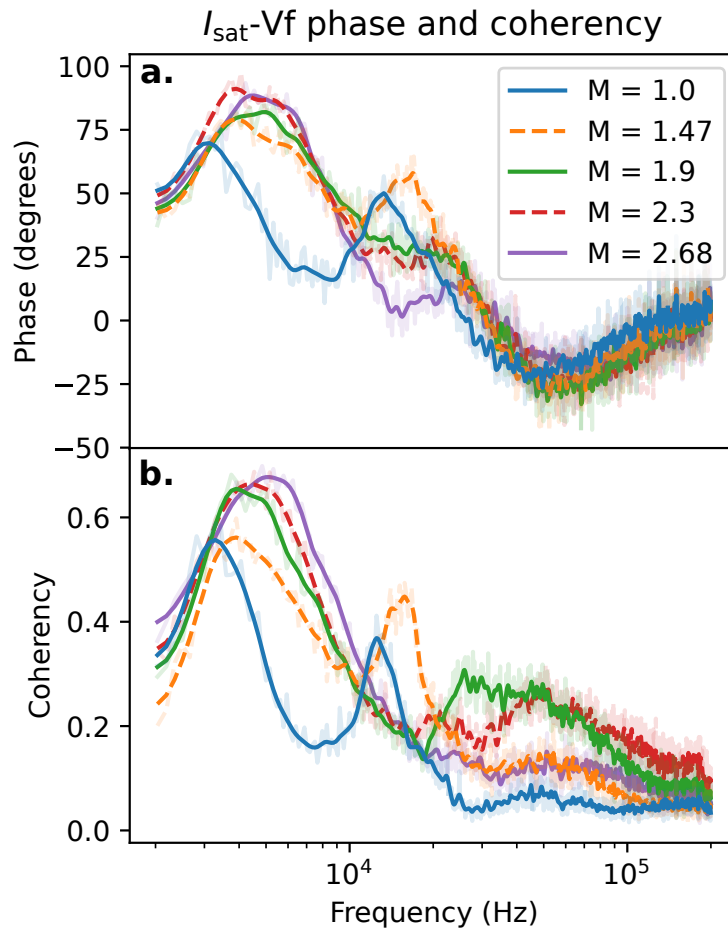


Figure 2.10: Phase (a) and coherency (b) of I_{sat} current and Vf near x_{PF} at the midplane, smoothed. Positive phase means I_{sat} leads Vf. Peaks in coherency occur between 3-5 kHz and at the drift-Alvén wave peaks between 12 and 25 kHz. These coherency peaks tend to have larger phase shifts than other nearby frequencies.

T_e profiles and fluctuations may affect particle fluxes but measurements of both were not taken in the same datarun; nevertheless, a quantification of the effect of T_e on particle flux is attempted. T_e fluctuations affect I_{sat} -based density measurements through the $T_e^{-1/2}$ term, and triple probe and Langmuir sweep T_e measurements suggest that temperature gradients have a negligible impact. A naive incorporation of temperature fluctuation data from DR2 into particle fluxes from DR1 suggest that cross-field particle flux may be underestimated by up to 50% via the I_{sat} temperature term, but the trend and relative fluxes across mirror ratios remain unchanged. Such a naive incorporation should be treated with suspicion because of the sensitive nature of the flux with respect to the gradient and the differences in profiles between DR1 and DR2. These difference in profiles made be caused by cathode condition, deposits on the anode, or a different gas mix and are difficult to account for.

2.3.3 Compensating for the Te profile

Electron temperature (Te) compensation for the I_{sat} measurement can be done in several ways. One way is to account for the average temperature (i.e., steady state) when calculating the density from I_{sat} . Te can be gathered from triple probe or swept measurements. Triple probe measurements are generally less reliable than swept probe measurements. The difference between swept and triple probe Te measurements can be seen in fig. 2.11. The two techniques have roughly good agreement, though the triple probe appears to slightly underestimate the temperature. The spikes in the edge are likely from sheath expansion of the probe in the swept measurements (see fig. 2.6).

Te fluctuations can affect I_{sat} fluctuation measurements through the $\sqrt{\text{Te}}$ term. In this case, Te measurements are difficult to compensate for in DR1 because of the changes in profiles between DR1 and DR2, so the Te fluctuations were included by finding the ratio in DR2 of I_{sat} fluctuations before and after including these Te fluctuations. This ratio was then applied to DR1. The issue of mismatched profiles still persists but this method allows for changes in fluctuation power between the two datarun sets. In general, $\tilde{\text{Te}}/\text{Te}$ fluctuations are at most than 30% (near the edge), and much lower in the core seen in fig. 2.12.

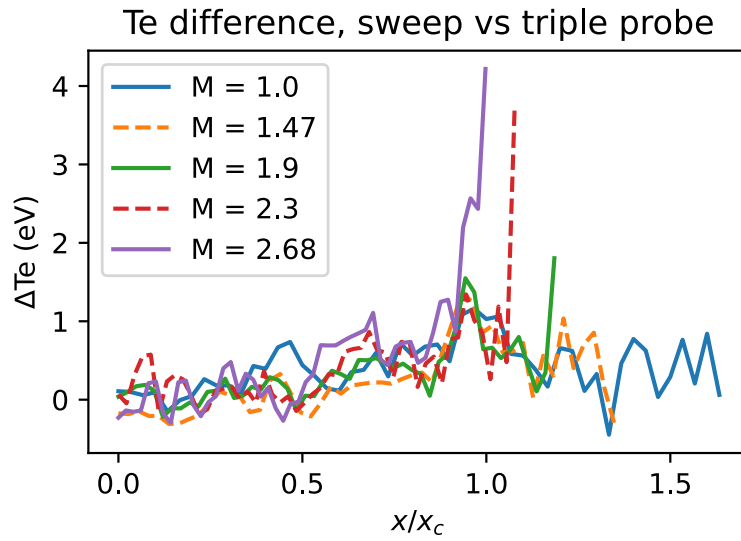


Figure 2.11: Difference between swept and triple probe temperature measurements. The triple probe appears to slightly underestimate the temperature and temperature gradient.

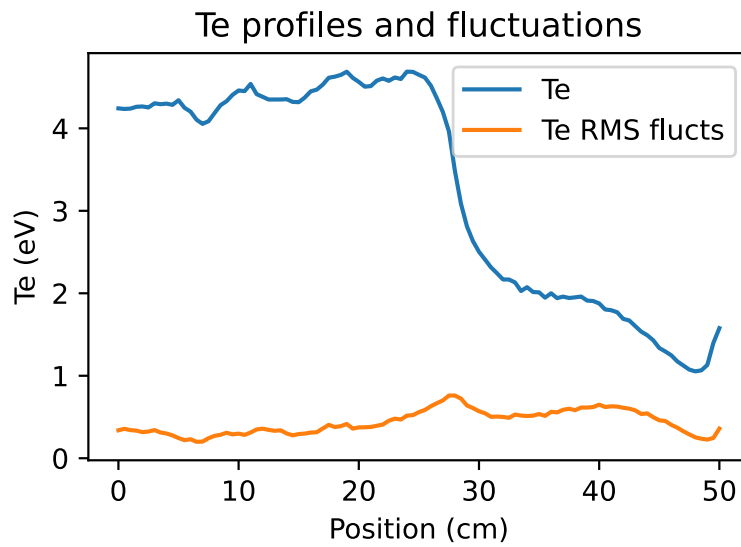


Figure 2.12: Te and Te fluctuation profiles from the triple probe. RMS electron temperature fluctuations are not particularly large.

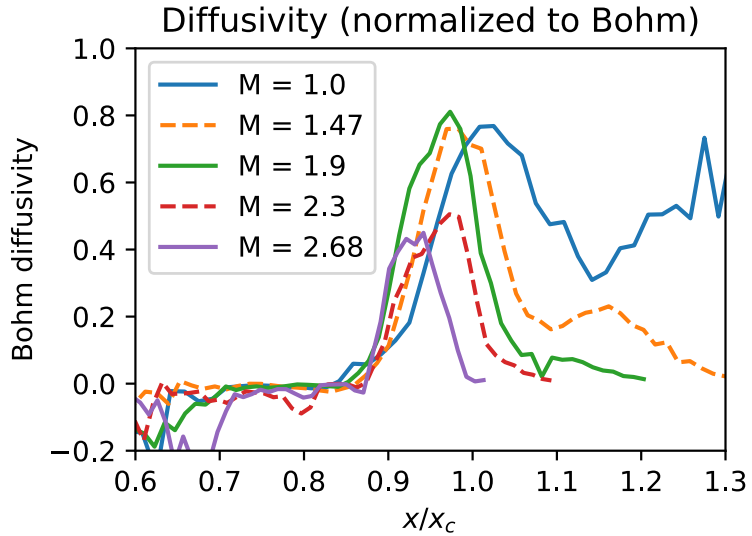


Figure 2.13: Diffusivity relative to D_B using a tanh fit for the density profile and the particle flux measurement assuming a constant T_e of 4.5 eV across the profile.

This T_e compensation becomes particularly important when calculating the I_{sat} profile gradients which is needed when calculating the diffusivity. A calculation of the diffusivity scaled to the Bohm diffusivity $D_B = \frac{1}{16} \frac{T}{eB}$ can be seen in fig. 2.13. This calculation uses the particle flux calculated earlier (in the paper) and tanh fit on the density profile for a density smooth gradient. In general, mirror ratios higher than two have a lower diffusivity. When the particle flux is compensated for T_e fluctuations, the temperature profile used in for the Bohm diffusion coefficient, and the density profile is smoothed convoluting a $\sigma = 2$ cm gaussian, the diffusion coefficient relative to D_B are roughly 2.5 times greater, seen in fig. 2.14. The trend, however, remains relatively the same: higher mirror ratios tend to have a lower diffusivity. The impact of different profile smoothing methods on the density gradient can be seen in fig. 2.15.

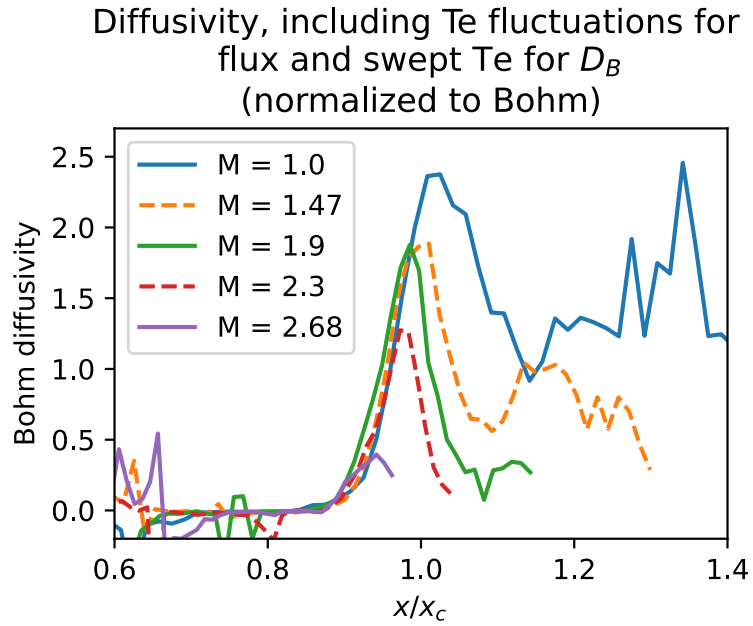


Figure 2.14: Diffusivity with Te compensation relative to D_B . The particle flux is compensated for Te fluctuations, and the swept-probe temperature profile is used for Te. The diffusivity is around 2.5 times higher than without compensation, but the trend remains similar.

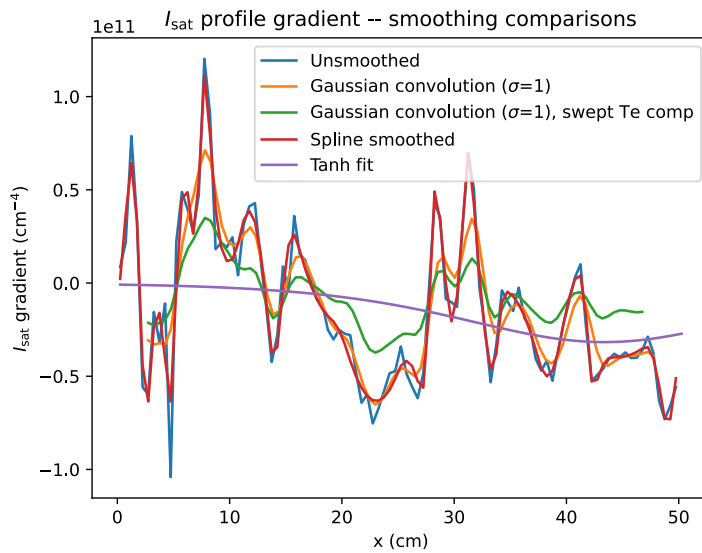


Figure 2.15: I_{sat} gradients under varying profile smoothing methods

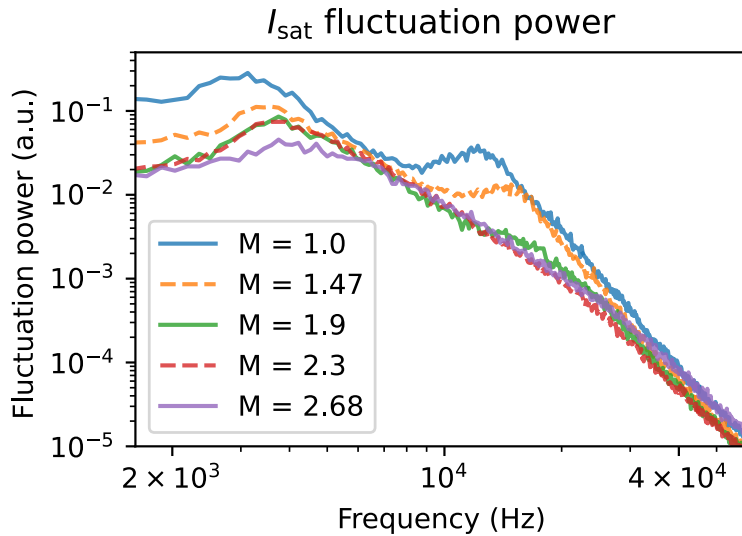


Figure 2.16: I_{sat} (density) fluctuation power averaged over a 1 cm region around x_{PF} at the mid-plane. The fluctuation power is largely featureless below 2 kHz and beyond 40 kHz aside from electronics noise.

2.3.4 Drift waves

The I_{sat} fluctuation power spectra in the region of peak power $x \sim x_{\text{PF}}$, also where the density gradient is strongest, can be seen in fig. 2.16. Notably, the fluctuation peaks shift to higher frequencies and decrease in total fluctuation power. The shift in frequency may be the Doppler shift caused by the change $\mathbf{E} \times \mathbf{B}$ plasma rotation seen in fig. 2.7 at the location $x/x_c \approx x_{\text{PF}}$. The shift in frequency is somewhat smaller than what would be expected from the field line-averaged increase in Alfvén speed at the longest possible wavelength. The phase angle of I_{sat} and Vf provides insight into the nature of the driving instability. Including a nonzero resistivity η in the drift wave leads to a small phase shift δ between density and potential. This phase shift δ in a collisional plasmas is on the order of $\delta \approx \omega v_e / k_{\parallel}^2 \bar{v}_e^2$ [Hor99]. Estimating this quantity using measured and typical values ($k_{\parallel} = 0.18$ rad/m, $\bar{v}_e = 1300$ km/s, $v_e = 3.7$ MHz, $\omega = 12$ kHz) yields a substantial phase shift of $\delta \approx 46^\circ$, which roughly agrees with the phase shifts in fig. 2.10, though the implied

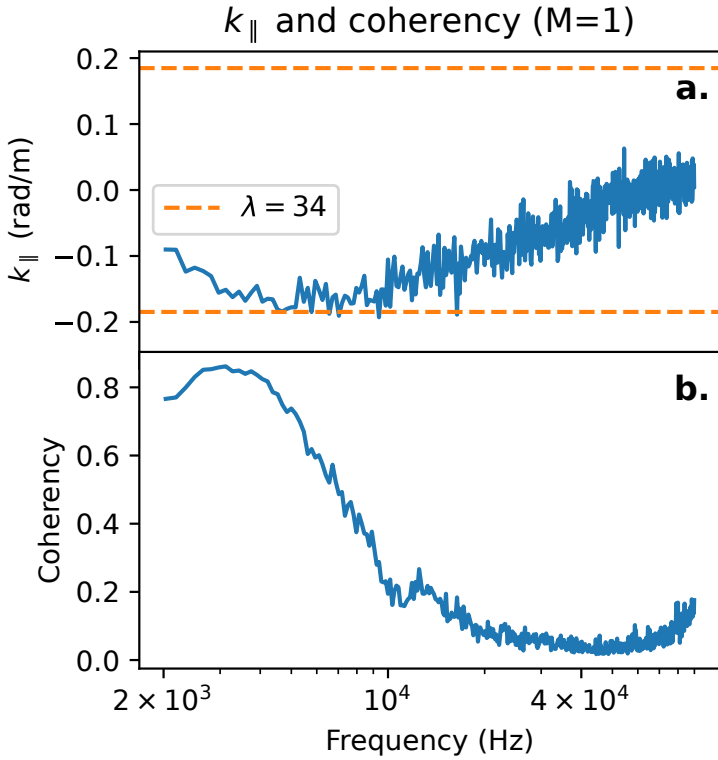


Figure 2.17: k_{\parallel} (a) and coherency γ (b) as a function of frequency. Only results from the $M = 1$ case are available, but it is clear that there are long ($\gtrsim 34$ m) wavelength modes at 3 and 12 kHz. The probes used for calculating k_{\parallel} were located at the midplane ($z=8.31$) and $z=12.14$ m, 3.83 m apart.

increased phase shift at higher frequencies does not agree with measurements. As seen in fig. 2.10, the phase shift between I_{sat} and V_f fluctuations are larger below 10 kHz, implying the presence of additional modes beyond or significant modification of resistive drift wave fluctuations. The phase difference between two V_f probes, 3.83 m apart, was used to calculate the parallel wavelength $\frac{2\pi}{\lambda} = k_{\parallel} = \phi_{Vf1, Vf2}/\Delta z$ assuming the wavelengths are greater than 7.66 m. The two probes mapped to the same field line only in the $M = 1$ configuration, so parallel wavenumbers are available only for the flat case. Parallel wavenumbers are theoretically calculable from 2d correlation planes but the coherency dropped dramatically when a mirror geometry was introduced. A 34 m wavelength mode likely contributes to the measured k_{\parallel} from 3 to $\gtrsim 10$ kHz (fig 2.17). Drift waves are long-

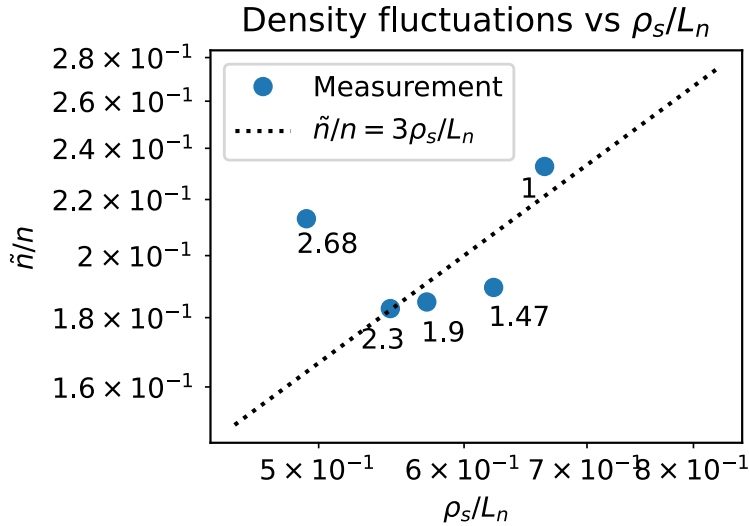


Figure 2.18: Normalized density fluctuations vs ρ_s/L_n . The measured values fall close to the $\tilde{n}/n = 3\rho_s/L_n$ line which is consistent with theory.

wavelength modes so coherent density and potential fluctuations along the flux tube are expected. The coherency is a measure of similarity of the spectral content of two signals, in this case Vf probes 1 and 2. The coherency is defined as $\gamma = \frac{|\langle P_{1,2} \rangle|}{\langle |P_{1,1}|^2 \rangle \langle |P_{2,2}|^2 \rangle}$ where $P_{x,y}$ is the cross-spectrum between signals x and y and the angle brackets $\langle \rangle$ denote the mean over shots. The coherency between the two Vf probes drops off with increasing frequency, with a slight bump at around 12 kHz. There are several candidates for the driving mechanism of the 3-5 kHz mode, but the 12 kHz mode is most likely a drift-Alfvén wave.

Drift wave theory[Lie85] suggests that the normalized density fluctuation level \tilde{n}/n should fall near $3-10 \rho_s/L_n$. A plot of this relation using experimental data can be seen in fig. 2.18. However, comparison of \tilde{n}/n with $1/(k_y L_n)$ show that the normalized density fluctuations are about an order of magnitude too small for the $1/(k_y L_n)$ observed which is unexpected and this conflict has not been able to be resolved in this study.

Another issue with this drift-wave interpretation of results is that the electron thermal diffusion along the field line is too high. The plasma must be collisional enough that thermal equilibrium is

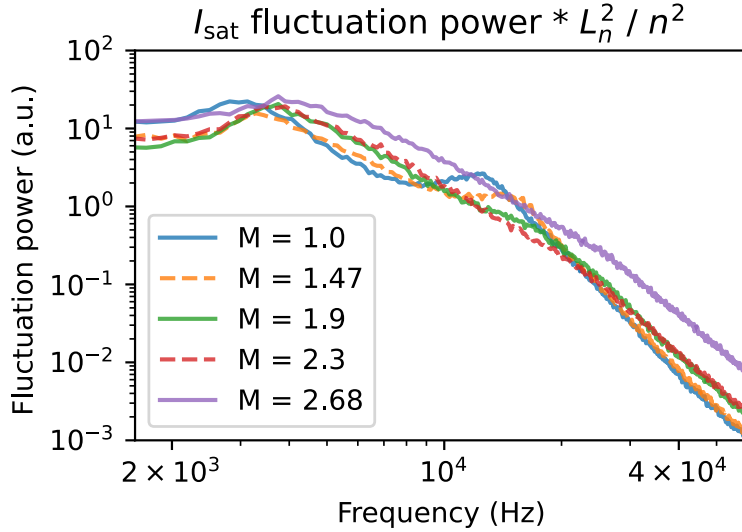


Figure 2.19: I_{sat} fluctuation power when scaled by the square of the gradient scale length and the squared density. We expect this value to be constant (assuming the same k_{\perp}).

guaranteed (i.e., the temperature is Maxwellian) , but if the collision rate is too high then thermal gradients can develop along the field line[Gol95]. This condition on thermal diffusivity condition for the drift wave ω and k_z is $\omega \ll k_z^2 v_{e,th}^2 / v_{ei}$. Plugging in values from the experiments yields frequencies at least 5 times greater than mandated by the diffusivity condition and the condition is violated. This condition violation may be responsible for the odd phase shifts seen between the density and potential fluctuations.

In saturated drift wave turbulence, the normalized density fluctuation amplitude is expected to scale with the gradient scale length L_n , so the fluctuation power then scales with L_n^2 . A plot of this can be seen in fig. 2.19. This assumes the same k_y , but as mentioned earlier, that scaling and the relationship in general is not consistent with theoretical predictions for saturated drift wave turbulence.

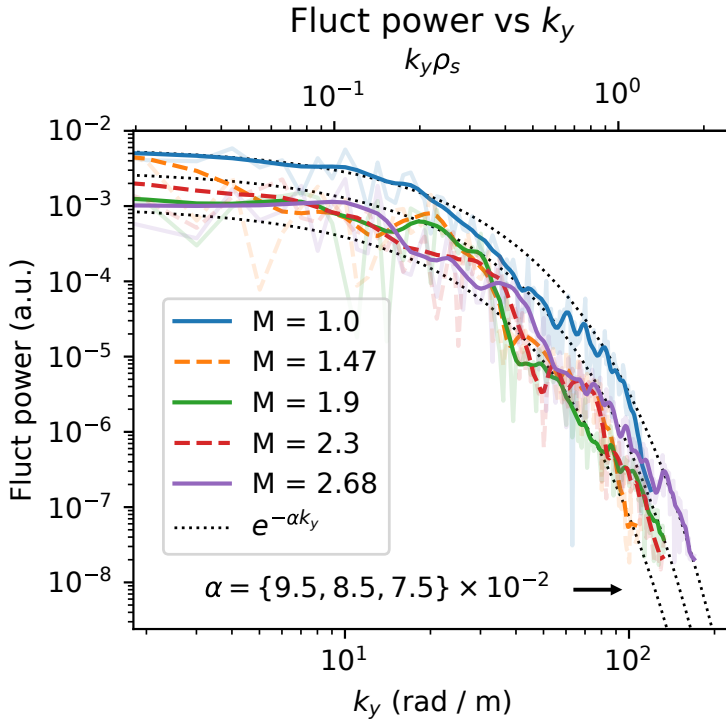


Figure 2.20: Fluctuation power summed for each k_y for frequencies up to 100 kHz, smoothed. The contribution to fluctuation power is negligible past 100 kHz. The fluctuation power decreases substantially when a mirror configuration is introduced, but no trend is seen otherwise and the k_y spectra remain exponential. Note the logarithmic scale.

2.3.5 Turbulence modification

The wavenumber-power relation in fig. 2.20 shows decreased fluctuation power when a mirror configuration is introduced. However, there is no discernible trend when the mirror ratio is increased further. The exponential nature of the curve also remains unchanged. The greatest decrease in fluctuation power occurred in low and high k_y 's, around 10 and 70 rad/m. The shape of the power- k_y curves follow an exponential distribution, and is inconsistent with a 2d drift-wave turbulent cascade (Wakatani Hasegawa k^{-3}) [WH84]. The steep dropoff in fluctuation power with k_y suggests that higher-wavenumber fluctuations do not have a significant effect on transport.

Previous simulations in a flat field [Fri13] predicted frequency and wavenumber spectra that can be fit with many power laws or exponentials, but the data presented here (figs. 2.16, 2.21, 2.20) appear to follow an exponential relationship within measurement variation.

Turbulence measurements can be directly compared to theoretical predictions and other devices, summarized by Liewer [Lie85]. For saturated drift wave turbulence, one expects the normalized fluctuation level $\tilde{n}/n \sim 1/\langle k_{\perp} \rangle L_n$, where k_{\perp} is some typical wavenumber. The power-weighted k_y (calculated from fig. 2.20) was approximately 15 rad/m, which is an order of magnitude too small to satisfy this relationship. \tilde{n}/n scaling with ρ_s/L_n , however, is roughly consistent with drift wave turbulence level saturation: the latter is ≈ 3 times larger. These comparisons suggest that the large, low frequency fluctuations (~ 3 kHz, which had even smaller k_y) may have a drift wave turbulence component but are dominantly driven by other instabilities. No trend is seen in ρ_s/L_n and $1/k_y L_n$ when mirror ratio was varied.

Core fluctuations appear to decrease dramatically as seen in the I_{sat} fluctuation power (fig. 2.8). The I_{sat} decorrelation time increases from ~ 0.7 ms for $M = 1$ to ~ 2.5 ms for $M = 2.68$. At $x = x_{PF}$, decorrelation times for all mirror ratios remained at 0.2 ms.

2.3.6 Magnetic fluctuations

The perpendicular magnetic fluctuation (B_{\perp}) component of the drift-Alfvén wave can be seen in fig. 2.21. These B_{\perp} fluctuations are spatially and spectrally coincident with the electrostatic fluctuations (fig. 2.16). Drift-Alfvén waves have been studied in the LAPD in the past [MM97, VG06]; strong coupling is observed for $\beta_e > m_e/m_i$ which is satisfied in this study. The Alfvén speed $\omega/k_{\parallel} = v_A = B/\sqrt{4\pi n M}$ (given $\omega \ll \Omega_{ci}$) when averaged over the entire column ranges from ~ 450 to ~ 1600 km/s. A k_{\parallel} corresponding to a wavelength $\lambda = 34$ m roughly falls within the bound established by the kinetic and inertial Alfvén wave dispersion relations at the frequency peaks observed at $x \sim x_{PF}$ seen in fig. 2.21. The lengthening of field lines caused by curvature accounts for at most 10% of the change in frequency.

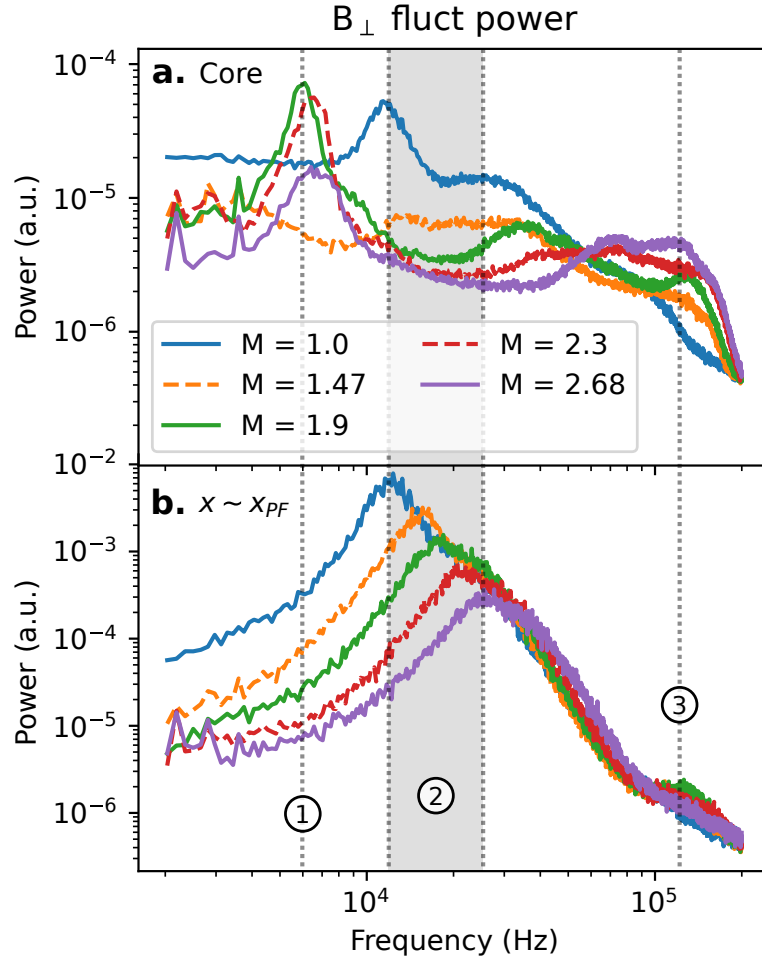


Figure 2.21: B_{\perp} fluctuation power averaged at the core from 0 to 3 cm (a) and around the peak fluctuation point ($x \sim x_{PF}$) (b). Fluctuation power decreases across the board with mirror ratio except for core frequencies close to Ω_{ci} . Peaks around 10 – 30 kHz at x_{PF} are consistent (region 2) with drift-Alfvén waves and the near-cyclotron frequency features in the core may be resonating Alfvén waves created by the magnetic mirror. Frequencies below 2 kHz and dominated by instrumentation noise and thus excluded.

The spatial extent of the B_{\perp} features identified in fig. 2.21 are plotted in fig. 2.22. Feature 1 at ≈ 6 kHz shows increased fluctuation amplitudes at $x = 0$ for mirror ratios 1.9 and above, but for $M = 1$ and $M = 1.47$ there is no increase in fluctuation power. A similar feature, but at a much smaller level, is observed in I_{sat} fluctuation power in the core as well. This core feature may be caused by the hole in the core seen in the I_{sat} profile (fig. 2.4) driving low-amplitude waves or instabilities. Feature 2 in fig. 2.22 is the magnetic component of the drift-Alfvén wave. The fluctuation power peaks at the gradient region and corresponds with the peak in density fluctuations (fig. 2.8).

Feature 3 is particularly interesting because this the only fluctuating quantity to *increase* with mirror ratio, seen in fig. 2.23. This feature may be broad evanescent Alfvénic fluctuations from the plasma source. These fluctuations have been observed in the LAPD in the source region alongside an Alfvén wave maser [MMC05]. Note that the Alfvén maser cannot enter the mirror cell at mirror ratios greater than 1.75 because the Alfvén maser resonates at $0.57 f_{ci}$ but the midplane is always at or near 500G.

The sub-2 kHz modes in B_{\perp} and its harmonics are nearly constant in power across the entire plasma; these features are likely perturbations from the magnet power supplies and thus ignored. The lack of radial, azimuthal, and axial structure in these magnetic signals below 2 kHz and narrow bandwidth indicate a non-plasma origin. Significant radial and azimuthal structure in B_{\perp} fluctuation power starts to appear in frequencies larger than 4 kHz.

The drift-Alfvénic nature of the 12 kHz Bdot feature is confirmed by changing the flat field from 500G to 400G: the feature shifts down in frequency from 12 to 10 kHz seen in fig. 2.24. From the drift wave and Alfvén wave dispersion relations the frequency is expected to be $400G / 500G = 0.8$ of the original, which is approximately what is observed. The k_y of the drift-Alfvén wave also has an effect and may be responsible for a $10 \text{ kHz} / 12 \text{ kHz} = 0.83$ factor instead.

There may be some sort of resonator made by the mirror cell and its interaction with Alfvén waves. In fig. 2.25, the behavior of the B_{\perp} spectrum in the core changes dramatically between 1 and 10 kHz in the short mirror when compared with the medium and longer mirrors. It's unlikely

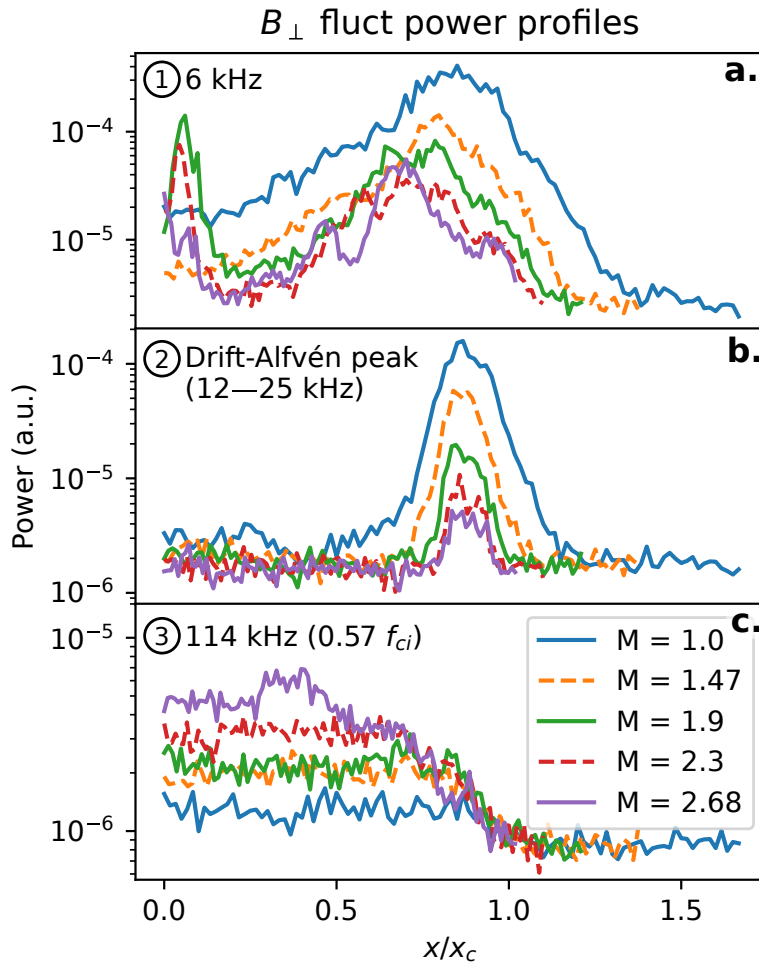


Figure 2.22: B_{\perp} fluctuation power profiles for the three regions shown in fig. 2.21: region 1 (6 kHz) (a), region 2 where frequencies are taken from the peaks of the drift-Alfvén waves for each mirror ratio (b), and region 3 (114 kHz) (c).

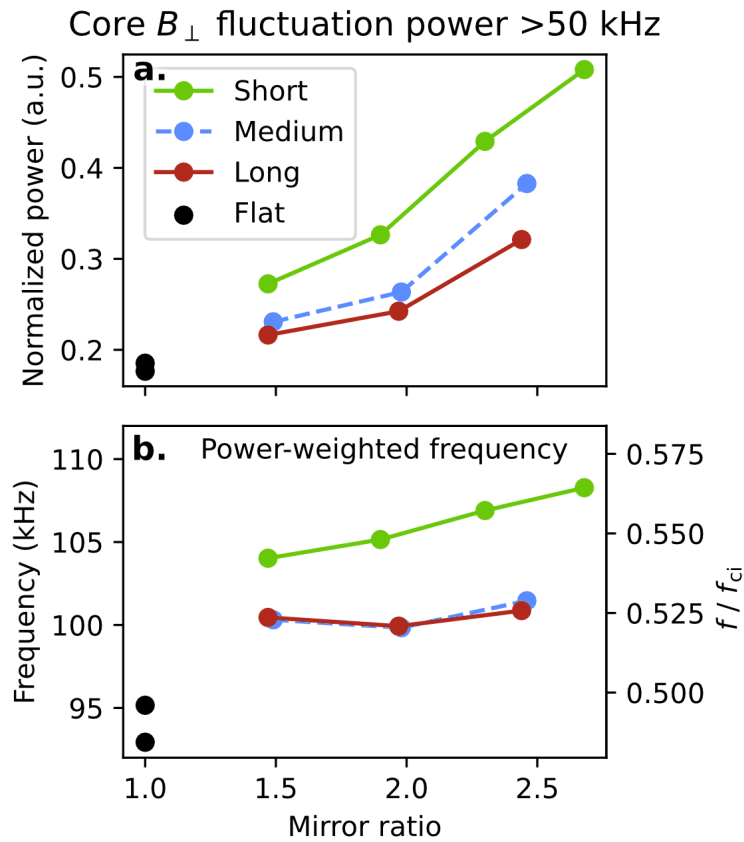


Figure 2.23: Summed fluctuation power of B_{\perp} in the core ($x/x_c \leq 0.3$) as a function of mirror length and ratio. Top (a): the fluctuation power is normalized by the sum of the full-spectrum summed power. Bottom(b): the frequency of the power distribution > 50 kHz weighted by the fluctuation power.

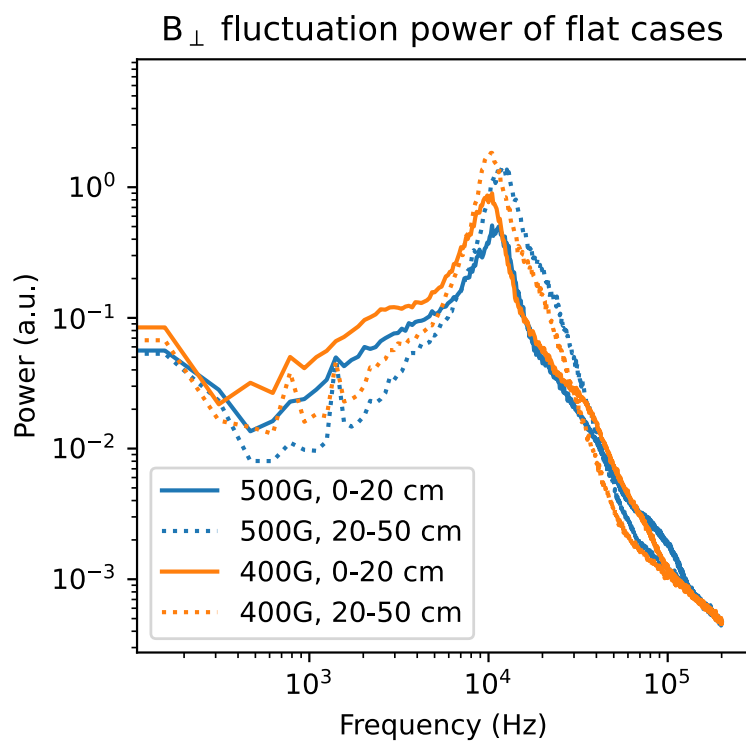


Figure 2.24: B_{\perp} flat field for 500G and 400G flat fields. The frequency of the identified drift-Alfvén wave at 12 kHz drops when the field is lowered, as expected.

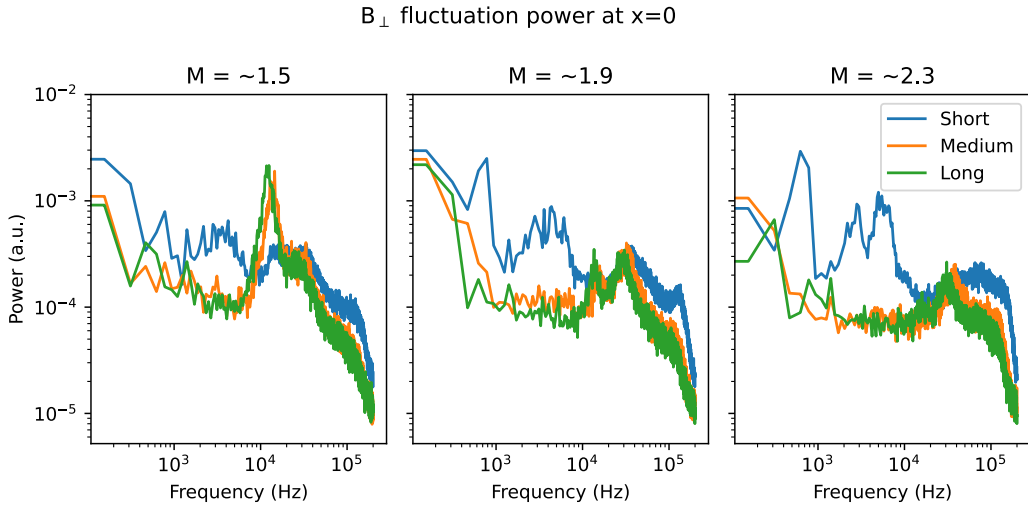


Figure 2.25: B_{\perp} at $x=0$ for different mirror lengths. The origin of fluctuations between 1 and 10 kHz is unknown.

that this is an Alfvénic fluctuation because the wavelength is an order of magnitude too large to fit in the machine.

For completeness, B_z fluctuation measurements are seen in fig. 2.26. The peaks in the 10 kHz region are likely crosstalk or slight coil misalignment of the probe and are picking up B_{\perp} fluctuations. The profile low frequency B_z fluctuations can be seen

The low frequency fluctuations in the Bdot spectra may seem important but plotting the spectra as a function of position (fig. 2.27) clearly shows the harmonics of the signal and the narrow bandwidth of them. This spectral feature is present regardless of mirror ratio, but changes in magnitude in approximate proportion with the field, i.e., the magnet power supply current. This power supply-induced field fluctuation can easily be seen in the ≈ 625 Hz mode in B_z , seen in fig. 2.28. The fluctuation power is largely constant across the entire plasma column, with the fluctuation power increasing with increased mirror fields. The taper of the fluctuation power at the edge could be caused by the background field vector no longer pointing in the z direction as the probe approaches the magnet coil. In general, the probe valves are not centered between the magnet coils, leading to rotation of the field vector as the probe is pulled out.

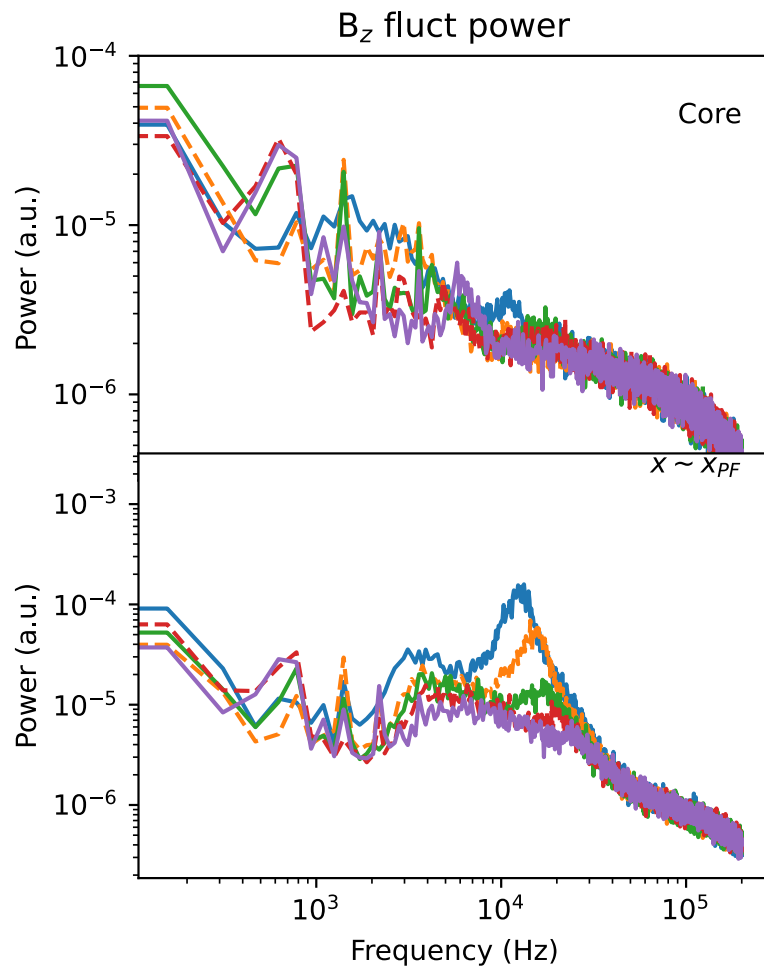


Figure 2.26: B_z fluctuations in the core and x_{PF} . Aside from picking up some B_\perp signal, the spectra are largely featureless.

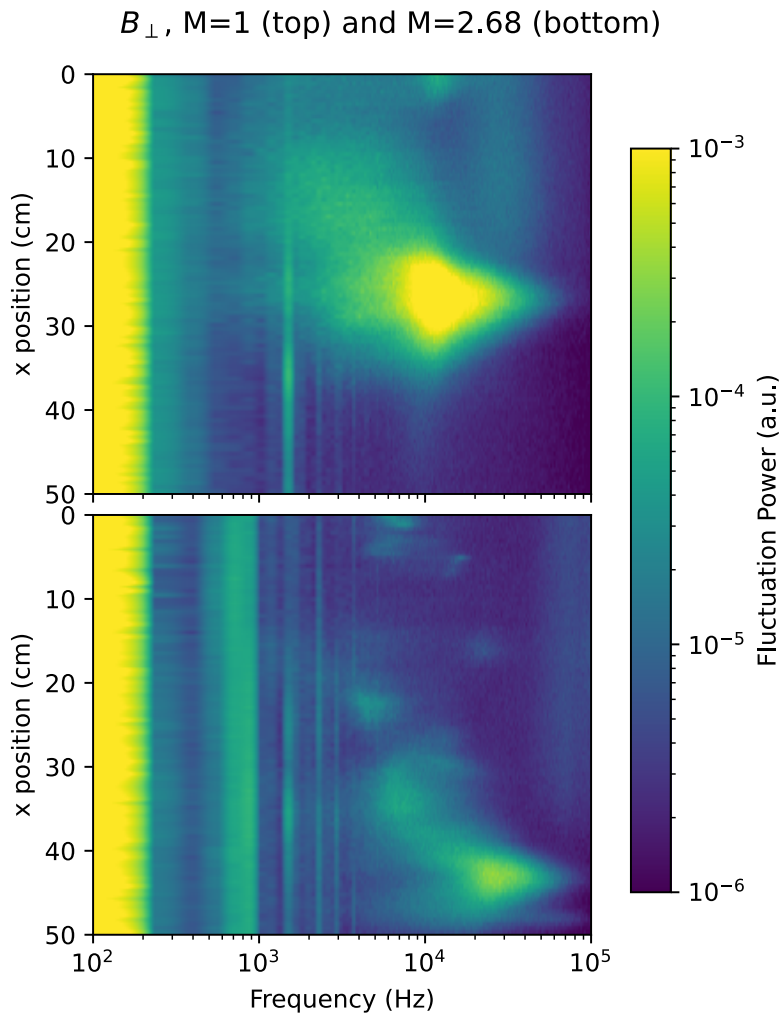


Figure 2.27: B_{\perp} fluctuation power for mirror ratios of 1 and 2.68. Lower frequencies are shown and the colorbar clipped to show detail in what appears to be power supply fluctuations

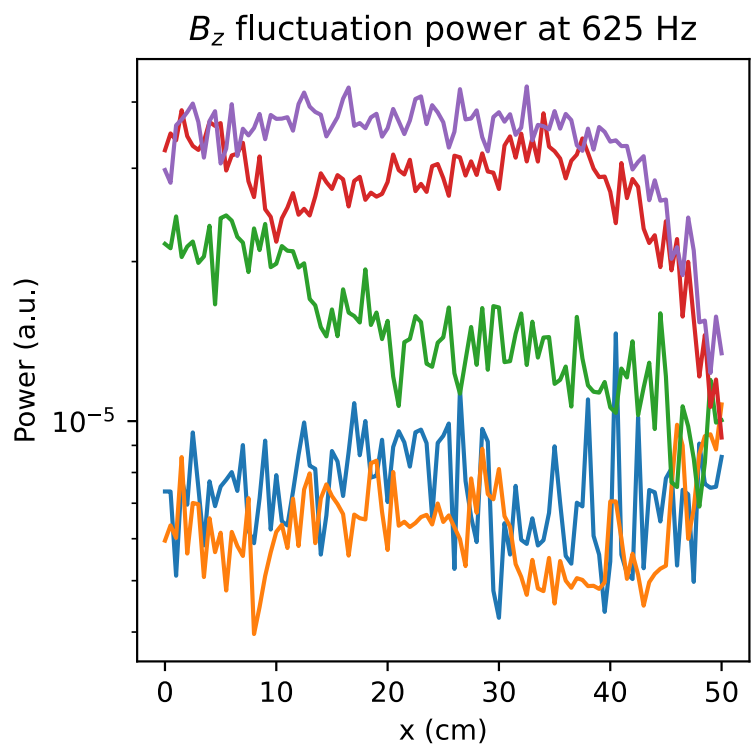


Figure 2.28: B_z fluctuation power profiles for all mirror ratios at 625 Hz.

2.4 2d Structure

The perpendicular magnetic field structure is measured by collecting x-y planar bdot ($dB_{\{x,y,z\}}/dt$) data alongside a stationary, axially separated I_{sat} reference probe (DR2). This probe provides a phase reference for the magnetic field fluctuations, allowing a 2d map of relative phase to be constructed over many shots. Only the region around x_{PF} was measured because of constraints on probe movement. The amplitude and phases for each magnetic field component are then used to reconstruct the local magnetic fluctuation vector \mathbf{B} . The axial current density structure, j_z , can be derived from this vector field. \mathbf{B} and the corresponding j_z for the flat-field ($M = 1$) case can be seen in fig. 2.29. Two main current channels can be seen with the magnetic fields circulating around them. This structure quickly decoheres in time as expected in a turbulent plasma. At higher mirror ratios, the field magnitude and corresponding current density decrease (which was also seen in DR1: fig. 2.21). Similar structure is seen in the mirror configurations; the $M = 1.9$ and $M = 2.68$ cases can be seen in fig. 2.30.

Using two, axially-separated, correlated I_{sat} measurements (DR2), with one collecting x-y planar data, the azimuthal mode number m (radially integrated) was calculated. Higher-frequency and higher- m features are seen with increasing mirror ratio (fig. 2.31). The increased frequencies may be caused by a change in Doppler shift by the $\mathbf{E} \times \mathbf{B}$ flow. This higher- m trend suggests that azimuthal structures do not scale with increased plasma radius but instead remain roughly the same size. The limited planar probe movement caused an increase in the lower bound on m in higher mirror ratios. At mirror ratios 1.47 and higher, the lower frequency component (< 10 kHz) appears to decrease significantly in amplitude. Calculating k_{\perp} from m evaluated at $x \sim x_c$ yields similar k_y values as the two-tip technique (fig. 2.32). The average k_y for a given frequency can be calculated using two Vf tips on the same probe by calculating the phase difference and dividing by the spatial separation of 5 mm: $k_y = \phi_{vf1, vf2}/\Delta y$ [BKP82]. The maximum $|k_y|$ measurable before aliasing is $\pi/\Delta y \approx 628$ rad/m. As seen in fig. 2.32, the k_y spectrum remains similar across mirror ratios, but the wavenumber extends further into higher frequencies with increasing mirror ratio. These

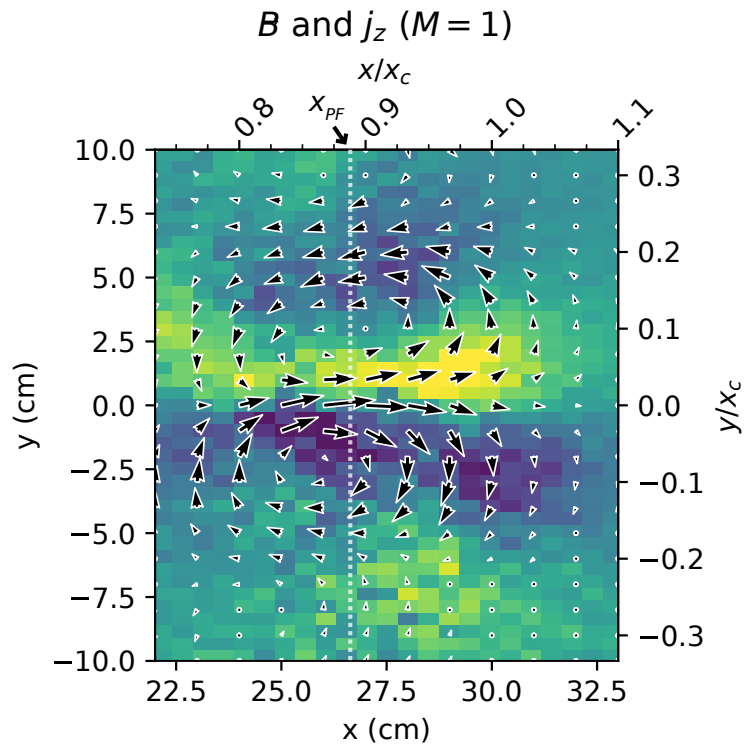


Figure 2.29: Perpendicular magnetic field and the derived current density for the flat-field ($M = 1$) case using a Bdot probe with an axially-separated I_{sat} reference (DR2). The x-y plane was centered near x_{PF} .

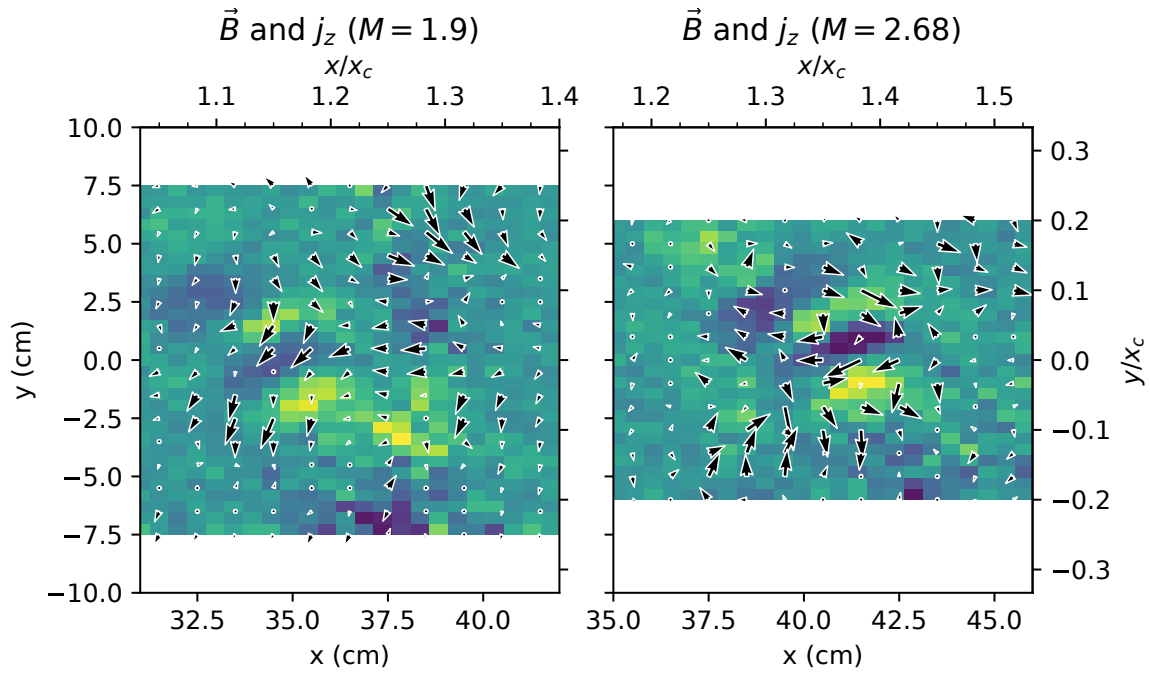


Figure 2.30: Perpendicular magnetic field and the derived current density for the $M = 1.9$ and $M = 2.68$ cases computed in the same manner as fig. 2.29. The x-y planes were centered near x_{PF} , and the view size was kept constant across the plots. The structure is much less obvious in the mirror cases, but all exhibit the expected Alfvèn wave pattern

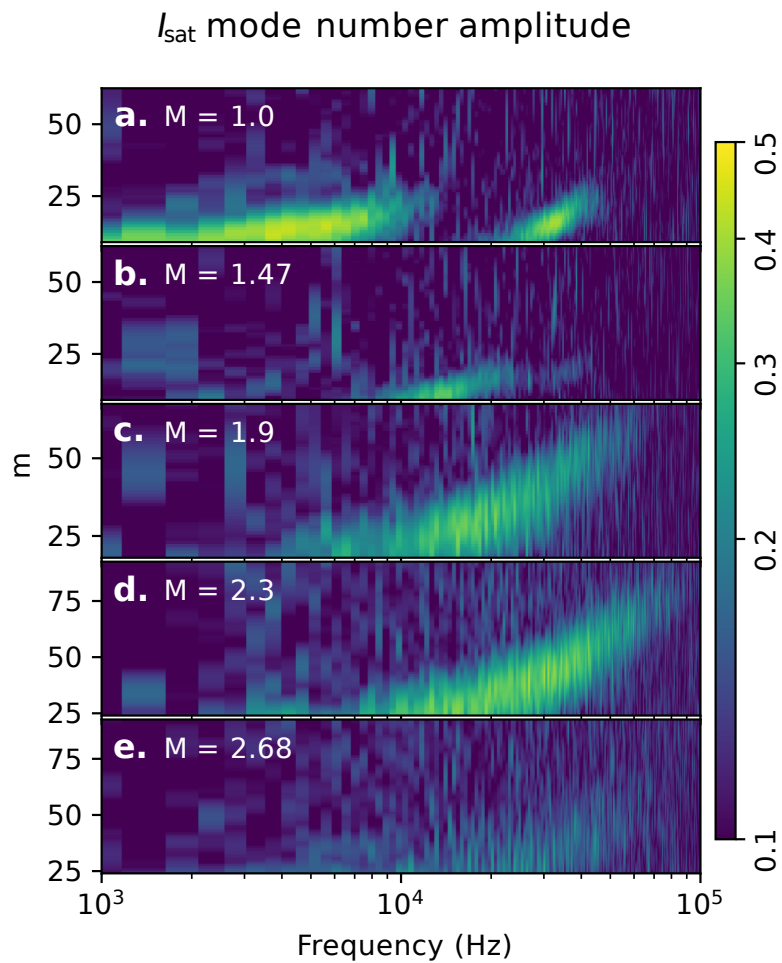


Figure 2.31: Azimuthal mode number m amplitudes calculated from two axially-separated, correlated, I_{sat} probes. Increasing mirror ratio (a to e) leads to increased m at higher frequencies.
(DR2)

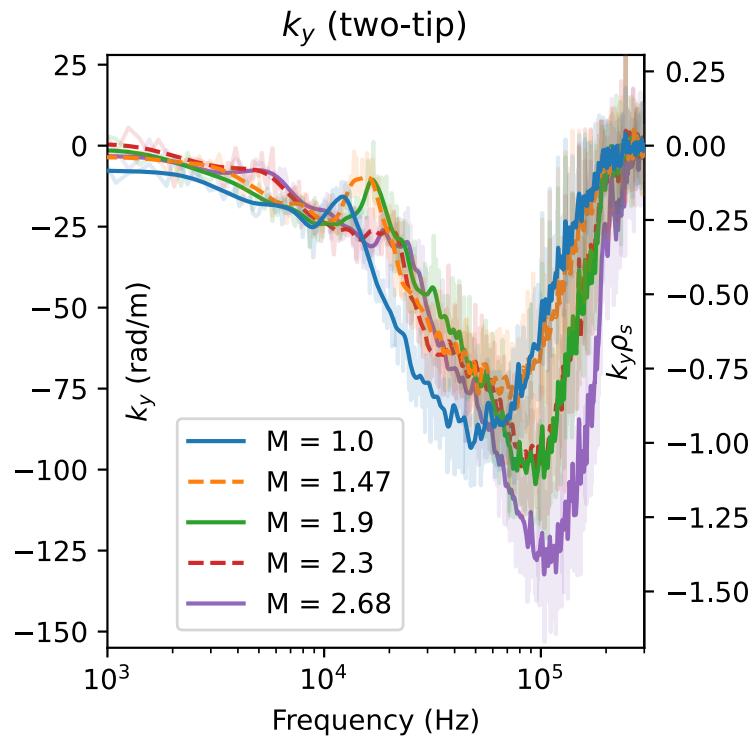


Figure 2.32: k_y averaged about x_{PF} and smoothed for each mirror ratio calculated using two vertically-separated Vf tips on the same probe. Little change is seen in k_y at lower frequencies but higher frequencies tend towards larger k_y at higher mirror ratios.

azimuthal mode numbers and gradient scale lengths are consistent with linear simulations using the 3d fluid code BOUT [PUC10] in the flat, unbiased case.

2.5 Discussion

2.5.1 Lack of mirror-driven instabilities

No evidence is seen for mirror-driven instabilities curvature, loss-cone, or otherwise. Given the LAPD parameters in this study (tables 2.1 and 2.2), the collision frequencies are sufficiently high such that the mirror is in the gas-dynamic regime: losses out of the mirror throat are governed by gas-dynamic equations rather than free streaming through the loss cone. To be in the gas-dynamic regime, the mirror length must exceed the mean free path of the ions [IP13]:

$$L > \lambda_{ii} \ln M / M \quad (2.2)$$

where L is the mirror length, λ_{ii} is the ion mean free path, and M is the mirror ratio. These collisions populate the loss cone and maintain a (cold) Maxwellian distribution, eliminating the possibility of loss-cone-, ion-driven instabilities like the AIC [CS82] or DCLC [Sim76, Kan79] instabilities that have been observed in other (historic) devices.

The paraxial, approximate interchange growth rate is [Pos87, RBC11]

$$\Gamma_0 = \frac{c_s}{\sqrt{L_M L_P}} \quad (2.3)$$

which yields $\Gamma_0 \approx 1.2$ kHz using $L_M \approx 7$ m and $L_P = 17$ m. c_s is used instead of \bar{v}_i because $T_i \ll T_e$ and mirror length L is split to distinguish between the contributions of the plasma length and mirror length to inertia and to curvature drive, respectively. Interchange is not visible in-part because the aspect ratio of these mirrors is quite large, limiting the growth rate of interchange. The length of the mirror (3.5 m), radius of curvature (6-7 m), and plasma column (17 m) are much larger than the radius of the plasma (0.5 m maximum), so the plasma inertia is large relative to the instability drivers. Line-tying to the cathode may further lower the growth rate. The hot cathode

used for plasma formation could function as a thermionic endplate that can supply current to short out the flute-like interchange perturbations. Line-tying has been seen in flux rope experiments on the LAPD using a hotter, denser source [VGP11], also in other devices [FKR79], and is why interchange was not seen in the earliest mirror machines [Pos87]. Note that the plasma terminates on the cathode or end plates before the magnetic field flares out, so there is no contribution to stability from an expander tank as seen in other GDTs [RBC11, IP13]. Finite Larmor radius (FLR) effects may provide a stabilizing effect for larger azimuthal mode numbers. At the highest mirror ratio, assuming a plasma radius of $a_0 = \sqrt{2.68} * x_{PF} = 43$ cm, the FLR stability criterion $\frac{m}{2} \frac{\rho_0 L}{a_0^2} > 1$ [RBC11] suggests a stabilizing effect may be present for azimuthal mode numbers $m > 4$.

If the curvature-induced interchange instability were observable, then introducing a mirror configuration would lead to new features in I_{sat} and B_{dot} fluctuations. In particular, low-frequency mode(s) – likely less than 10 kHz given the low m-number and plasma rotation rates – would be observed growing from the pressure gradient region. For onset of the interchange instability, the mirror curvature or plasma pressure would need to be increased but the precise conditions required for this onset are not yet known for the LAPD.

Interchange could also be at least partially stabilized by the continuous production of electrons in the core that are electrostatically trapped by the ambipolar potential [GH71]. The intuition behind this stabilization mechanism is as follows: electrons are continuously produced via ionization of neutrals, and any change in the local potential will cause more or fewer electrons to be lost out the ends of the device along that field line, counteracting the potential change. This stabilization mechanism has been experimentally demonstrated to completely suppress interchange when the ambipolar potential $\Phi \gtrsim 6T_e$ [KHS87].

The $\mathbf{E} \times \mathbf{B}$ shear flow present (fig. 2.7) may also make a contribution to the stabilization of interchange [RBC11, BLZ03, BBS07, BBC10]. The estimated shearing rate is between 3 and 10 kHz, which is greater than the estimated ≈ 1.2 kHz growth rate of the interchange mode.

2.5.2 Instabilities driving turbulence

Rotational interchange can be significant driver of the broadband turbulence spectrum in the LAPD, particularly when a biased limiter is installed. This observation has been confirmed by both linear simulations [PUC10] and biasing experiments [Sch13].

This rotational interchange mode has the following attributes, as summarized by [Jas72]: flute-like ($k_{\parallel} = 0$), $|e\tilde{\phi}/T_e|/|\tilde{n}/n| \gtrsim 1$, radial potential phase variation 45 to 90°, maximum possible $|e\tilde{\phi}/T_e| < 1$. All of these attributes are seen for the lower frequency (3 kHz) mode. The Vf radial phase variation when $M > 1$ is not clearly seen because the coherency is dramatically reduced along the field line. The rotational interchange mode could couple with the drift wave at $k_{\parallel} = \pi/L \sim 0.37$ rad/m ($n = 0.5$), which has been observed in the past [Sch13] and likely present here. Estimates of shearing rate from the $\mathbf{E} \times \mathbf{B}$ flow velocity profile (fig. 2.7), calculated fluctuation ratios, and radial phase shift variation suggest that Kelvin-Helmholtz-driven turbulence is not significant, if present at all. Historically, biasing a limiter has been required to clearly observe the Kelvin-Helmholtz instability [HPC05, SCR12, Sch13].

Low frequency density fluctuations may also be driven by a flute-like conducting-wall temperature-gradient instability which only requires an electron temperature gradient to grow (even with straight field lines) [BRT91]. Simulations of turbulence in the LAPD suggest the possible presence of these conducting wall modes (CWM) which have the highest growth rate for $m \leq 20$ [FCU13]. This lower- m mode could be responsible for the peak around 3 kHz in the $M = 1 I_{\text{sat}}$ fluctuation (fig. 2.16) and azimuthal mode numbers (fig. 2.31) and for the low-frequency low- k_{\parallel} or flute-like behavior (fig. 2.17). This CWM may also be responsible for flatter electron temperature profiles seen in previous studies [PMC22, Sch13] (fig. 2.6).

These linearly unstable modes may be outgrown by a rapidly-growing nonlinear instability that couples to drift-like modes as suggested by simulations [FCU13]. This nonlinear instability is driven by the density gradient at an axial modenumber of $n = 0$ and nonlinearly transfers energy to $n \neq 0$ fluctuations.

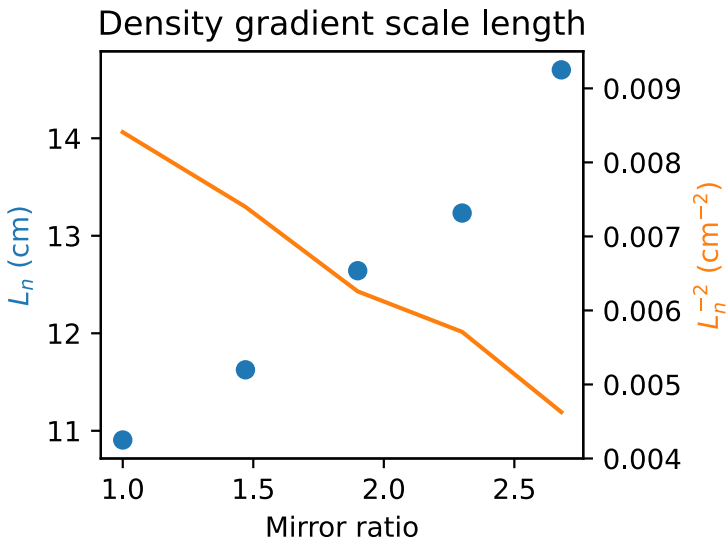


Figure 2.33: Gradient scale length L_n and the associated term in the drift wave growth rate L_n^{-2} . This scale length was calculated over a 3 cm region around x_{PF} (peak fluctuation region) at the mid-plane. Increasing the mirror ratio increases the gradient scale length, which suggests weakening of the underlying instability driver.

The conducting wall mode and nonlinear instability may be present in these mirror experiments but the spectra are adequately explained by linearly unstable modes. Precise identification of these modes requires further study; neither of these instabilities have been directly observed in the LAPD.

2.5.3 Causes of particle flux reduction

The reduction in particle flux explained by a reduction in density fluctuations likely caused by a increased gradient scale length $L_n = \frac{n}{\nabla n}$ (fig. 2.33), decreasing the linear drift wave growth rate and saturation level seen in sec. 2.3.5. This gradient length reduction may also reduce the growth rate of the rotational interchange instability, which may be the dominate driver for the low-frequency large-amplitude density fluctuations.

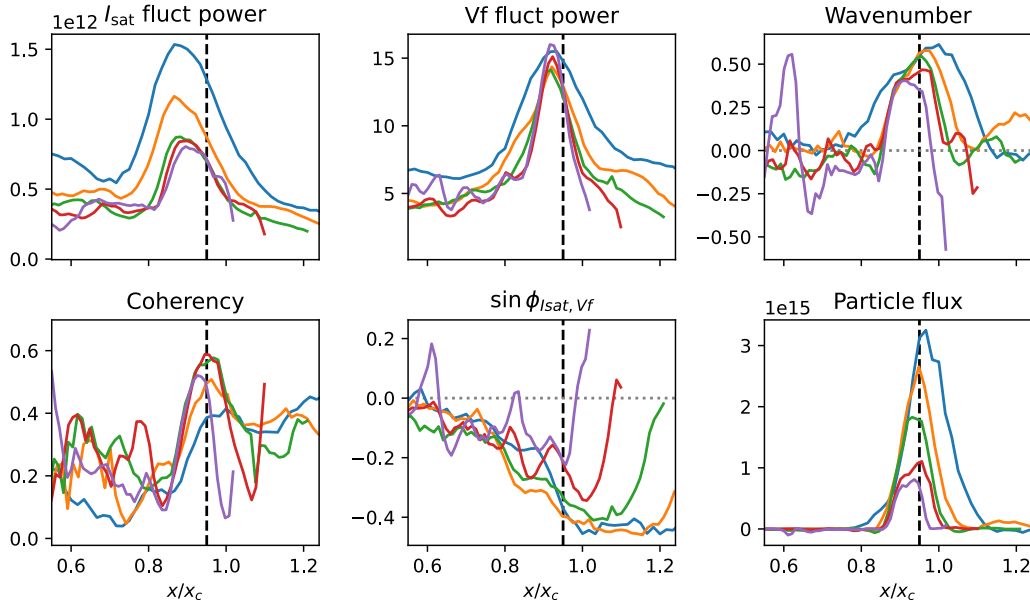


Figure 2.34: The particle flux broken down into the components used to calculate it. The dashed black line is simply a visual reference near the peak particle flux at $x/x_c = 0.95$. The I_{sat} fluctuation power appears to be the largest driver in changes in particle flux. The colored lines correspond to mirror ratio as seen in earlier plots.

A plot showing the breakdown in particle flux can be seen in fig. 2.34. The changes in I_{sat} fluctuation power is the most obvious driver, but the $I_{\text{sat}} - Vf$ phase difference, coherency and wavenumber also seem to have an effect. The Vf fluctuation power remains largely consistent across the different mirror ratios. Note that this particle flux appears somewhat different because this is using the uncalibrated I_{sat} values and the flux is not scaled by solid angle. This flux also does not use temperature-compensated I_{sat} measurements.

The decorrelation time of I_{sat} time series data is around 0.15 ms at x_{PF} . An estimate of the $\mathbf{E} \times \mathbf{B}$ flow shear from fig. 2.7 (DR2) yields a shearing time between 0.1 and 0.3 ms at x_{PF} . These times suggest that spontaneous flow shear may be important for suppressing turbulence, as seen in other studies [SCR13, CYK05], at all mirror ratios. However, no clear trend in shearing strength is seen with mirror ratio.

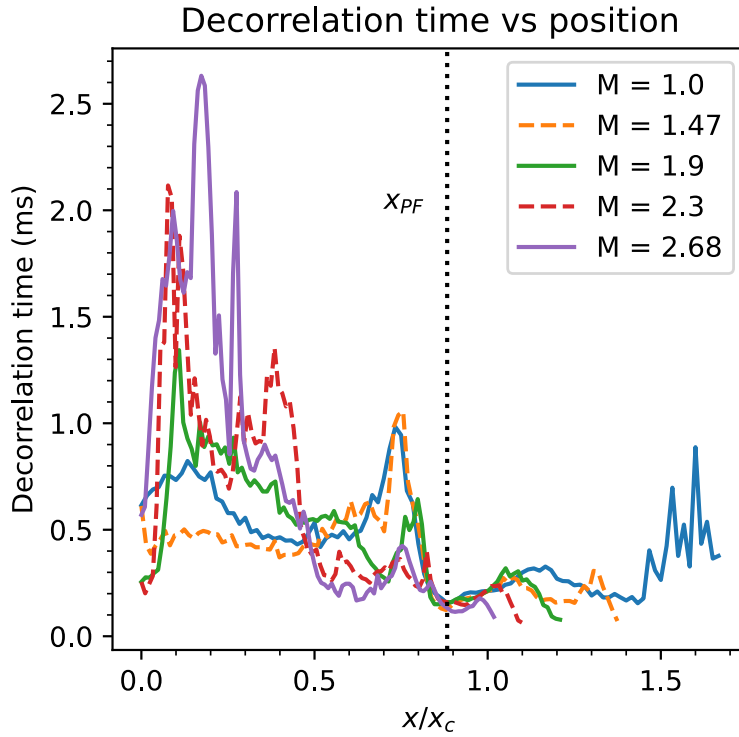


Figure 2.35: Decorrelation time from I_{sat} time series data for different mirror ratios. All of the mirror ratios have a minimum decorrelation time at x_{PF} and much longer times (slower rate) in the core.

The decorrelation time of a signal is calculated by taking the autocorrelation of a signal – I_{sat} in this case – and finding the full-width half-max of the envelope using a Hilbert transform. This decorrelation time can be seen in fig. 2.35. The decorrelation is minimized at x_{PF} and maximized in the core, further confirming the turbulent nature of the fluctuations at x_{PF} .

The estimated shearing rate from DR2 can be seen in fig. 2.36. The rate is plotted instead of time because of the singularity when the flow reverses. At around x_{PF} ($x/x_c \approx 0.87$), the shearing rate is around 2 to 8 kHz meaning the shearing time is around 0.5 to 0.125 ms. This is fairly close to the decorrelation time from the I_{sat} time series measurements (fig. 2.35). These similar times/rates suggests that ExB shearing may set the limit on cross-field transport.

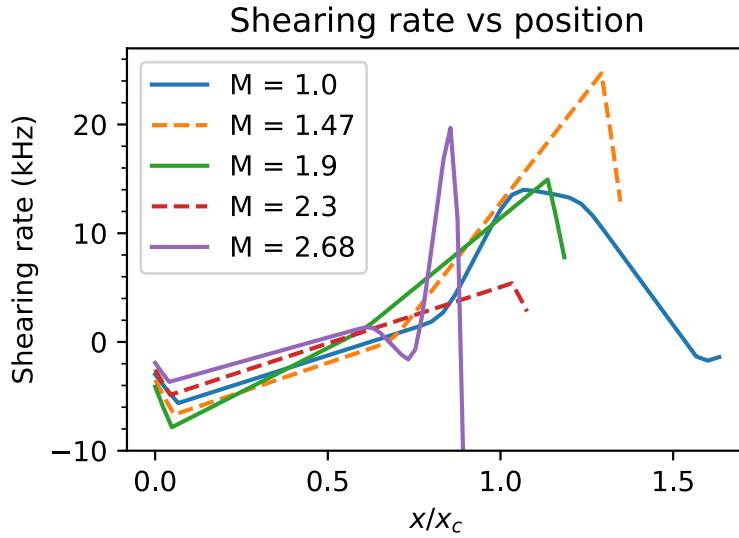


Figure 2.36: ExB shearing rate.

It is important to note that the electron thermal diffusion time along the field line is very long compared to the frequency of the drift wave ($\omega \gtrsim k_{\parallel} \bar{v}_e^2 / v_{ei}$) [Gol95] so the electron temperature along the field line may not be constant on the drift wave timescale. This factor is not taken into account in this analysis but may have substantial impact on interpretations of the measured phase shift.

2.5.4 Differences between DR1 and DR2

Directly applying signals between runs is fraught with danger because the profiles/plasmas changed appreciably between the two.

The discharge power for DR2 was roughly 10% smaller than what was seen in DR2 seen in fig. 2.37. Since the discharge voltages were similar (DR1: 62.5 vs DR2: 60.5) we expect to see less dense plasmas in DR2.

Changes in the I_{sat} profiles between the two dataruns (and between two separate measurements in DR1) can be seen in fig. 2.38. Interestingly, there is some difference in the profiles *within the*

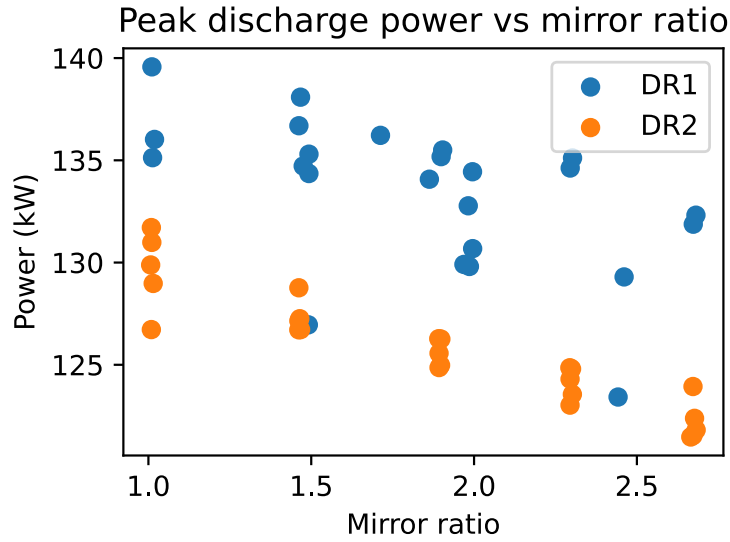


Figure 2.37

same datarun which could be caused by probe shadowing. Probe shadowing effects should be less important in mirrors because the probe closest to the cathode magnetically maps to a region further outside than the probes in the mirror cell. This difference in density can also be seen in the line-integrated density from the 56 GHz interferometer (port 23): fig. 2.39. These differences in density could also be caused by different hydrogen and helium pressures in the runs. Helium pressure was roughly the same for both dataruns ($6\text{e-}6$ to $3\text{e-}6$ for DR1, $6\text{e-}6$ to $2\text{e-}5$ for DR2), but the hydrogen pressure was an order of magnitude higher for the DR2, on the order $7\text{e-}6$ instead of $1\text{e-}7$ for DR1. These differences in pressures could have had an effect on plasma formation and transport, thus affecting profiles. Hydrogen fraction is known to have an effect on breakdown characteristics in the new LaB₆ cathode (cite Shreekrishna?).

Differences could also occur within dataruns. Calibrating the effective area of the I_{sat} probes can be done using the 56 GHz interferometer, but this calibration factor drifted over time and seen in fig. 2.40. This could be deposits being removed or added to the probe, affecting the effective area. This calls into question the reliability of absolute I_{sat} measurements, but we proceed regardless because there's no easy way to fix this issue.

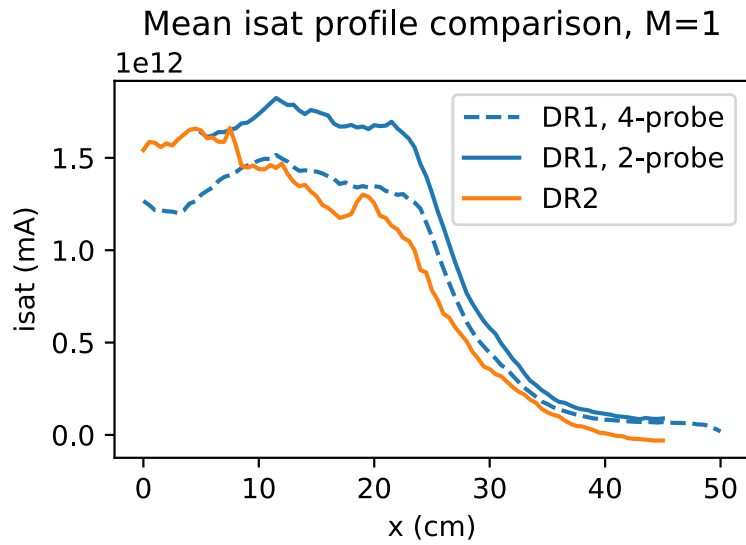


Figure 2.38: I_{sat} profiles ($M=1$), DR1 vs DR2 in the mirror cell.

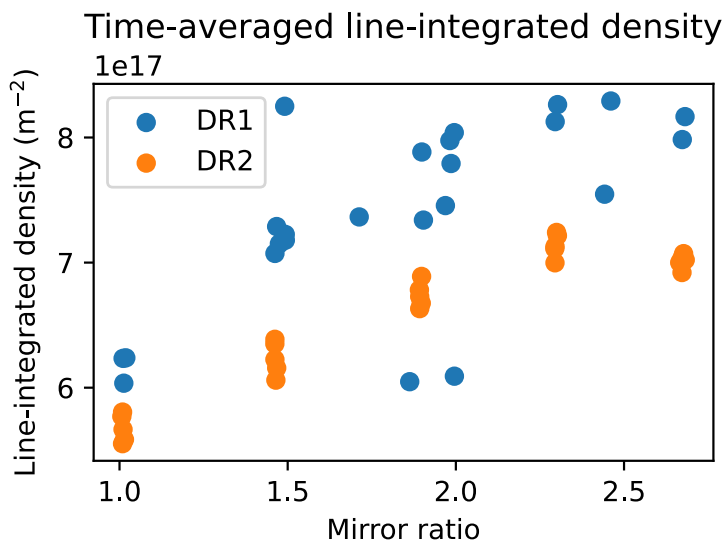


Figure 2.39: Line integrated density from the 56 GHz, DR1 vs DR2. On average, DR2 has a lower density than what's seen in DR1. The interferometer is located near the region of good curvature closest to the cathode.

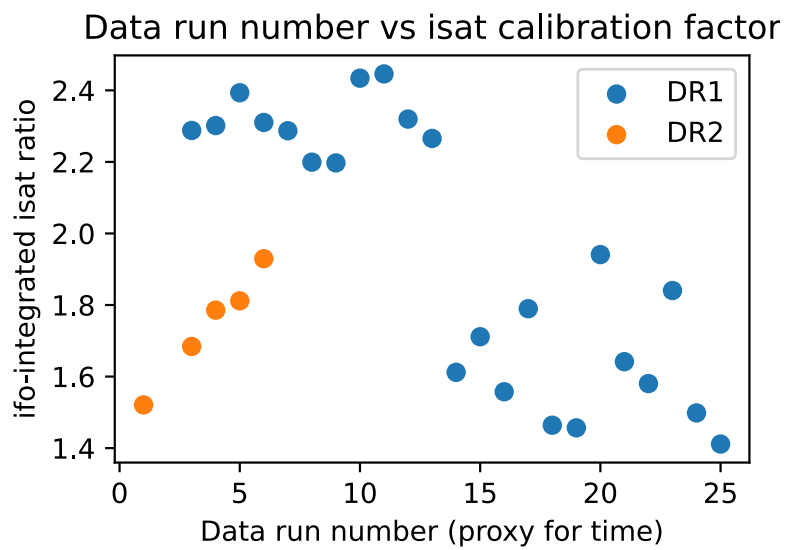


Figure 2.40: I_{sat} calibration factor over different dataruns from the same run sets. Datarun number is monotonically increasing, so in this case it's used as a proxy for time. A rather large variance is seen in this calibration factor, which suggests the I_{sat} probes having time-varying characteristics affecting the measurement.

2.6 Conclusions and future work

Turbulence and transport was studied in mirrors with varying lengths and ratios using the flexible magnetic geometry of the LAPD. Particle flux and fluctuation amplitudes decreased up to a factor of two when mirror ratio was increased. The primary drivers of turbulence were identified as the rotational interchange mode, caused by spontaneous rotation, and unstable drift-Alfvén waves driven by the density gradient. The decrease in density fluctuation amplitudes can be attributed to an increase in the gradient scale length caused by the dimensionally wider plasma at the mirror midplane. Despite imposing a mirror configuration, no signs of mirror-driven instabilities were observed. The highly-collisional, GDT-like plasma produced suppressed any velocity space instabilities. The interchange growth rate was likely suppressed to an undetectable level by line-tying, in-cell electron production, and shear flow.

Future experiments in hotter regimes with the new LaB6 cathode [QGP23] will need to be performed to evaluate the robustness of these results, particularly concerning the stabilization of curvature-induced interchange. Additionally, the source field should be matched to the mirror mid-plane field so that the plasma remains the same radius to isolate geometric effects. Simultaneous measurements using flux and/or vorticity probes and I_{sat} are needed to concretely determine if azimuthal flow shear is modified by the mirror field, and to quantify the effect of flows on rotational interchange and drift wave instability drive in general. Multiple simultaneous axial measurements of potential would enable better understanding of the axial wavenumber and identification of possible modes.

CHAPTER 3

Optimizing mirror configurations in the LAPD using machine learning

Shorten; less detail Modern machine learning (ML) techniques based on neural networks (NNs) provide an opportunity to learn trends directly from data, which is the first step towards automating fusion science. The goal of this work is to demonstrate that ML-based insight extraction is possible and useful. The Large Plasma Device (LAPD) is a remarkably flexible basic plasma science device with a high shot rep rate (0.25-1 Hz) and relatively reproducible plasmas. The LAPD also capable of high-spatial-resolution measurements, such as the ion saturation current (I_{sat} proportional to density and the square root of electron temperature). These traits of the LAPD make it the ideal machine for producing datasets for experimenting with ML techniques. Time-averaged ion saturation current data were recorded from randomly sampled machine configurations in the LAPD in order to create a minimally biased, relatively diverse dataset. Over 100,000 shots in over 45 different machine configurations were collected. Magnetic field strengths, fueling parameters, and the discharge voltage were varied in these experiments. A five-model, 200k parameter NN ensemble was trained on this dataset using a negative log-likelihood (NLL) loss function. This ensemble and loss formulation enable the breakdown of uncertainty into aleatoric and epistemic components. During inference, these NNs can be evaluated quickly (4 million predictions per second on an RTX 3090). This fast inference enables creation of a comprehensive set of I_{sat} values (over 127 million) in any LAPD machine configuration at any position bounded by the training set. Trends inferred using this method, such as effects on I_{sat} of introducing mirrors or changing the discharge current, are consistent with intuition. In addition, these predictions can be used to

optimize LAPD behavior. The required machine conditions for minimizing or maximizing axial variation (quantified by the standard deviation of on-axis I_{sat} values) can be found via comprehensive search over the predicted I_{sat} values. The corresponding machine conditions were then executed on the LAPD. The optimized, experimental axial I_{sat} profiles yielded similar behavior to model predictions, but with appreciable absolute error. This error could be caused by the lack of absolute calibration of the Langmuir probes. The predicted uncertainty provides a relative metric for gauging model confidence. Ultimately, ML techniques provide a new way of extracting insight from experiments. LAPD plasmas can be optimized by using simple and straightforward neural networks, which is a first in the magnetized plasma (or fusion) community. All code and data used in this study will be made freely available.

3.1 Introduction

Machine learning (ML) techniques, particularly the use of neural networks (NNs), have become increasingly used in magnetized confinement fusion research to control and stabilize fusion plasmas. Plasma devices are complicated systems with many possible settings, actuators, and actuator states. From an ML point of view, these parameters are a high-dimensional input into a system whose output (plasma behavior) we wish to understand. Because this space is high-dimensional, understanding how these devices work is often time-consuming and requires careful planning. We seek to accelerate understanding of fusion devices with the goal of putting fusion on the grid as fast as possible.

Many studies have used ML for profile prediction on a variety of tokamaks, particularly for real-time prediction and control. A model was built to predict several quantities, such as electron density and temperature, in DIII-D using NNs[?]. A reservoir computing approach was also performed[?] featuring the ability to quickly adapt to new situations or other tokamaks. Entire shots have also been auto-regressively predicted using Recurrent NNs (RNNs)[?]. RNNs have also been used for autoregressive predictions on the EAST[?] and KSTAR tokamaks[?, ?], the

latter of which were used to train a reinforcement learning-based controller. Electron temperature profiles have also been predicted using dense NNs on the J-TEXT tokamak [?].

Much focus in the fusion community has been on instability mitigation in tokamaks, particularly the catastrophic loss of plasma confinement known as a disruption. The tearing instability is a common cause of disruptions in tokamaks, and the mitigation of these instabilities has been performed in DIII-D using reinforcement learning[?]. In general, there has been much work on predicting disruptions, the most important of them being an RNN approach by Kates-Harbeck et al.[?] and the random forest approach taken by Rea et al.[?]. A good overview of pre-2022 disruption prediction activity can be found in Vega et al.[?].

The process of inferring trends using data-driven methods has been relatively uncommon. Finding scaling laws are one such task that is at the extreme high-bias end of these data-driven methods. Nonetheless, ML techniques have been used as a tool to discover scaling laws. Classical ML techniques were used to find the boundary between safe and disruptive operational space on the JET tokamak[?]. Genetic programming was then used to find a symbolic, power-law expression for this boundary to provide interpretability. Similarly, the development of the new Maris density limit[?] used ML techniques – neural networks, random forests, linear SVMs, and linear regressions – to find a stability boundary by treating the fit as a classification problem. The power law derived from the linear SVM far outperforms that traditional Greenwald scalings when validated across many tokamaks. This new scaling also predicts, in advance, the density limit violation within a discharge much better than the Greenwald or other scalings.

The laser plasma research field (ICF, wakefield, and others) has used machine learning extensively for different applications, enumerated in the review by Dopp et al. [?]. We have not been able to find the extra step of using ML methods to infer trends in plasma research in general. Data-driven plasma science in general has been reviewed by Anirudh et al. [?].

This study takes these data-driven methods a step further: instead of learning a model for particular task (e.g., disruption prediction or profile prediction), we scan along inputs of this model to infer trends. Trend inference applied in this way is new to magnetized plasma research.

The goal of this study is to develop a data-driven model that can provide insight into how machine settings impact the plasmas produced in the Large Plasma Device (LAPD) in lieu of a theoretical model. We demonstrate the capability to infer trends in a particular diagnostic signal, the time-averaged ion saturation current (I_{sat}) for any mirror (or anti-mirror) field geometry in a variety of machine configurations. Trends of the effect of varying a particular machine setting can be predicted in a data-efficient manner by training on many randomly-selected machine settings. This partially randomized data acquisition is a first for magnetized plasma research. Additionally, to the authors' best knowledge, this is the first time NNs have been used to directly infer trends in magnetized plasmas. Using this model, LAPD plasmas can also be optimized given any cost function, which we demonstrated by minimizing axial I_{sat} variation. This global optimization is only possible using ML techniques. This work demonstrates the usefulness of a pure ML approach to modeling device operation and shows how this model can be exploited. We encourage existing ML projects and experiments to consider this approach if possible, but it may require assuming some risk to acquire diverse datasets.

This paper is organized as follows: section 3.2 discusses the LAPD and the data acquisition process. Development of the model and uncertainty quantification are discussed in sections 3.3 and 3.4, respectively. Validation of the predictions made by the model are shown in section 3.5. Inferring trends in discharge voltage and gas puff duration are presented in section 3.6. Optimizing the axial I_{sat} profile is performed and validating the optimization on the LAPD can be seen in section 3.7. The discussion, outlook, future work, and conclusions are discussed in sections 3.8 and 3.9.

3.2 Data collection and processing

3.2.1 The Large Plasma Device (LAPD)

The Large Plasma Device (LAPD)[?, ?] is a basic plasma experiment located at the University of California, Los Angeles. The LAPD produces an up to 18m long, 1m diameter plasma column

Large Plasma Device

Top view

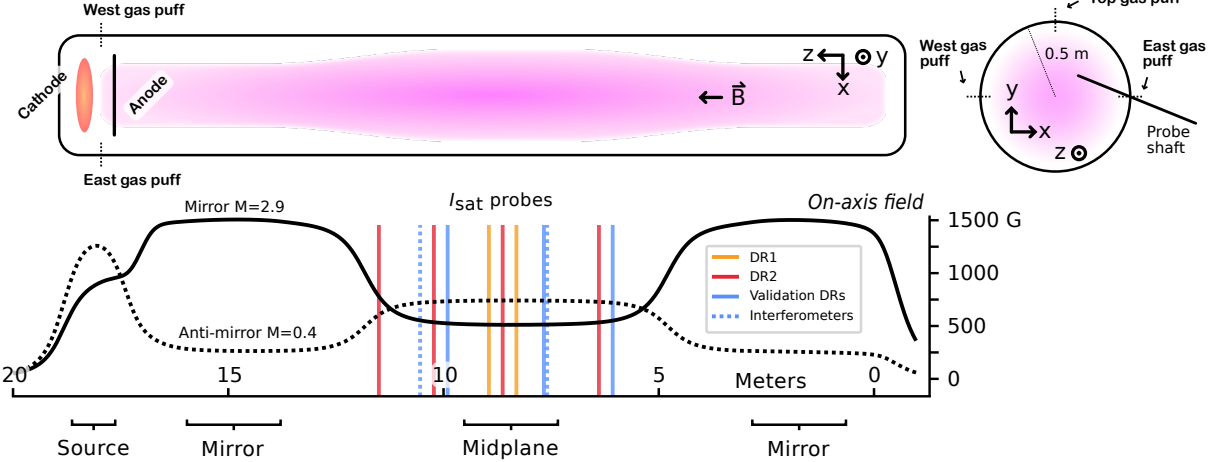


Figure 3.1: A cartoon of the Large Plasma Device, the coordinate system used, examples of a mirror and anti-mirror magnetic field configuration, and probe locations used in this study. The source, mirror, and midplane regions are labeled; the three fields were programmed independently.

with densities up to $3 \times 10^{13} \text{ cm}^{-3}$ and temperatures up to 20 eV, though typical operation yields temperatures around 5 eV. Every 32 cm, the LAPD has unique ball valves between the solenoid coils that permit 3d movement of inserted probes. These probes enable the collection of time series data with high spatial resolution at virtually any point in the plasma column. The LAPD also has a discharge repetition rate, configurable between 0.25 and 1 Hz. Additionally, the LAPD has 13 independently controllable magnet power supplies to shape the geometry of the magnetic field along the length of the device. The discharge is formed by 38 cm diameter lanthanum hexaboride (LaB₆) cathode[?] and 72 cm molybdenum anode 0.5m (-z direction) at the southern end (+z) of the device. A cartoon of the LAPD and relevant coordinate system can be seen in fig. 3.1.

The LAPD has many actuators available for various physics studies. Components such as biasing rings, antennas, and an additional cathode, can be inserted into the LAPD. However, in this work we focus on the settings fundamental to the operation of the main cathode. In particular, the region half way between the cathode and anode contains three gas puff valves: East, West,

and top. The opening size, duration, and triggering of these valves has a large impact on plasma formation. There is also a static gas fill system but it is not used in this study. The cathode-anode voltage (and more broadly, discharge power) also has a significant effect on the plasma density and temperature downstream of the source. The magnetic field configuration also greatly affects the plasmas produced. One main actuator not considered in this study is the cathode temperature because it takes many hours to adjust and equilibrate, limiting the diversity of any dataset collected.

This diagnostic coverage, high repetition rate, and high degree of configurability makes the LAPD a natural fit machine learning studies.

3.2.2 Data collection and processing of I_{sat} signals

Ion saturation current, referred to as I_{sat} , is measurement using a sufficiently negatively biased Langmuir probe such that only ions are collect. The measurement is proportional to $S n_e \sqrt{T_e}$, where S is the effective area of the probe. Since the area varies depending on the particular probe used for the measurement, the I_{sat} displayed will be normalized to area. An I_{sat} value of 1 mA/mm² corresponds to $n_e \approx 1\text{-}2 \times 10^{12} \text{ cm}^{-3}$ for a T_e from 4 to 1 eV.

Data were taken over two separate weeks, 14 months apart. The first run set will be referred to as DR1 and the second as DR2. These run sets are further broken down into *dataruns* which are a collection of shots with the same machine conditions. 67 dataruns were collected in total.

I_{sat} signals were averaged from 10 to 20 ms. This range was chosen to avoid effects of ramp up and to average-out plasma fluctuations. Plasma profile evolution is not covered to limit the scope and compute required for this study. Note that the I_{sat} time traces can vary significantly between axial (z) position and dataruns (read: machine settings). For the I_{sat} signal on the same probe as a Langmuir sweep (DR2 port 26, z=863 cm), the I_{sat} signal was averaged only where the sweep was off (plus an additional 40 μs buffer) and not affecting the measurement. Some I_{sat} signals in DR1 saturated either the isolation amplifier or the digitizer and were removed from the dataset.

The machine parameters varied were the source field, mirror field, midplane field, gas puff

valve voltage, gas puff duration, and discharge voltage. The source, mirror, and midplane regions are labeled in fig. 3.1. The magnetic field in each of these regions effectively control the width of the plasma in those regions relative to the cathode. The gas puff voltage controls the rate of gas flow into the chamber while the valve is open. The relationship between gas puff voltage and this rate is not yet quantified. The gas puff duration is how long this voltage is applied to the gas puff piezo valve. The discharge voltage is the voltage the capacitor bank is charged to, which is then applied across the anode and cathode 10 ms after the gas puff voltage is applied. The discharge voltage is related to the discharge current (and thus total discharge power), but the current cannot be set ahead of time: it is determined by other machine settings.

These machine parameters – with the exception of gas puff duration – were randomly sampled via Latin-hypercube sampling (LHS) for 44 of the dataruns. Data were then collected with these settings. Gas puff duration was reduced for the last seven runs to 20, 10, or 5 ms. The breakdown of each setting in the dataset can be seen appendix 3.11, table 3.4. The top gas puff valve was used for only the first nine dataruns of DR2 because of equipment issues.

Data were collected on the probes at equally spaced locations on a $y=0$ line (51 dataruns total) or an $x-y$ grid (16 dataruns total). The spacing varied between 1.5 to 2 cm depending on the particular datarun and grid configuration. The axial positions of the probes were left fixed at six different locations in total. 895 cm and 831 for DR1 and 1150, 1022, 863, and 639 cm for DR2 (also shown in fig. 3.1).

Six shots were recorded per position with the exception of the first four dataruns in DR1 with five shots. Note that each position may have some variation in the I_{sat} value recorded, but the model will only learn the expected value. Generative models – future work – can instead directly learn the distribution.

3.2.3 Dataset distribution and bias

Planar data were typically recorded overnight, leading to many more shots for that particular machine state. In general, $\approx 64\%$ of the shots recorded were planes.

Only seven dataruns with gas puff durations less than 38 ms were recorded. These dataruns were taken as an attempt to see mirror-related interchange instabilities in higher-temperature, less collisional regimes. Because of the small amount of dataruns in non-random machine configurations the training data is heavily biased towards the 38 ms gas puff duration. Good model performance on regimes similar to these short gas-puff runs is not expected.

The top gas puff valve was also used for the first nine runs of DR2.

The I_{sat} distribution is dissimilar between DR1 and DR2. DR1 appears to have a more uniform distribution than DR2 does. Combining the two datasets results in many I_{sat} examples near 0 mA/mm² and a sharp decrease in number of examples above 10 mA/mm². We expect or model to be biased towards fitting lower I_{sat} values better, and to perform badly in cases with very high I_{sat} values. Data bias is further discussed in appendix 3.11.

The final input size for the neural networks is 12: source field, mirror field, midplane field, gas puff voltage, discharge voltage, gas puff duration, three positions (x, y, z), probe rotation, run set flag, and the top gas puff flag. The last two were added as the project continued. The data are scaled to the peak-to-peak for each input; there are no outliers in the dataset so all scaled values are sane.

3.3 Model development, training

3.3.1 Initial training details

The loss used to train the model was simply the mean-squared error (MSE):

$$\mathcal{L}_{\text{MSE}} = \frac{1}{m} \sum_{i=1}^m (f(x_i) - y_i)^2 \quad (3.1)$$

where x_i is the inputs for the i th example, y_i is the ground truth, m is the number of examples in a given batch, and f is the neural network. During training, overfitting was tracked using a traditional 80-20 train-validation random split. Unless stated otherwise, a dense neural network, 4 layers deep and 512 units wide, was trained with AdamW using a learning rate of 3×10^{-4} . Leaky ReLU activations were used instead of tanh to avoid vanishing gradients and adaptive gradient clipping [?] (cutting gradients norms above the 90th percentile of recent norms) was used to mitigate exploding gradients.

3.3.2 Baselines for mean-squared error

A summary of the performance of all models can be seen in table 3.1.

A model was first trained with zeroed-out inputs as a baseline and to validate the data pipeline. This model effectively has only a single, learnable bias parameter at the input. This process yields a validation loss (simply MSE in this case) of 0.036.

A simple dense model (4 layers, 512 wide with one output; 794113 parameters, tanh activations) was trained on a zeroed-out input as a baseline for determining that the model is learning anything at all. This process yields a validation loss of 0.036. A linear model obviously cannot fit the dataset because profiles, amongst other features are never linear. However, a simple linear model can provide a performance baseline to help spot bugs when training more complex models. This baseline linear reaches a training and validation loss (MSE) of around 0.014.

3.3.3 Effects of reducing the training set

Several models were trained with dataruns cut out, decreasing the diversity of the training set. The test set was kept fixed. Loss on the test set monotonically increases with decreasing diversity.

An equal amount of dataruns from each run set were randomly and iteratively removed from the training set. Results when changing training set diversity are roughly what was anticipated: model performance on the test set decreased with the decrease in diversity.

Table 3.1: Summary of test set losses for different training data and ensembles

Model	MSE $\times 10^{-3}$
Zeroed-input	36
Linear model	14
Linear with tanh	11
9 dataruns	7.0
19 dataruns	6.9
29 dataruns	4.2
39 dataruns	4.1
49 dataruns	3.4
DR1 only	6.4
DR2 only	5.4
Full set, large model	2.8
Full set average	3.6 ± 0.56
Full set ensemble	2.9 ± 1.1
“Run set” flag ensemble	1.9 ± 0.64
“Top gas puff” flag	1.8

Multiple models with different seeds were trained for the full-training-set model to measure the performance variance over model parameters. The DR1-only dataset was evaluated on the DR1-only test set, and likewise with DR2. The cross-run test set losses were incredibly high, near or above the zero-input baseline of 3.6×10^{-2} . The “best” model was a large 12-deep 2048-wide dense network trained on the full training dataset, evaluated at 30 epochs. Longer training or larger models may yield better test set results, but will likely not come close to the training and validation losses which are on the order of 10^{-5} .

One unexpected result is that models trained on a single run set appear to perform worse when evaluated on the test set (from that particular run set) compared to the mixed training set of the same size (green arrows vs blue x). This fact indicates that mixing dataruns, despite different probe calibrations and cathode state, provides beneficial information on the structure of the I_{sat} measurement. This model is able to leverage information in both dataruns despite potential differences in the effect of the machine settings and the cathode condition.

3.3.4 Improving performance with machine state flags

Run sets DR1 and DR2 were taken roughly 14 months apart so the machine state was different from the two runs. In DR1, only one turbo pump was operating leading to much higher neutral pressures than in the DR2 run set. A new flag (mean-centered and scaled) was added to the inputs indicating which run set each shot belongs to. All the predictions in this work use the DR2 run set flag (a value of 1.0) because turning off the turbopumps is not a commonly desired mode of operating the LAPD. The inclusion of this flag also provides the model the ability to distinguish between the probe calibration differences between DR1 and DR2. An ensemble prediction with this run set flag brings the test set MSE down to 1.9×10^{-3} .

A flag indicating when the top gas puff valve was enabled in DR2 was also added to all training data, allowing the model to further distinguish between different fueling cases. The addition of this flag incrementally improved test set MSE to 1.8×10^{-3} and so remains as the input.

3.4 Uncertainty quantification

3.4.1 β -NLL loss and learning rate scheduling

One can interpolate between an MSE loss and Gaussian NLL loss by introducing an adaptive scaling factor $\text{StopGrad}(\sigma_i^{2\beta})$ into the NLL loss function (eq. 3.2):

$$\mathcal{L}_{\beta-\text{NLL}} = \frac{1}{2} \left(\log \sigma_i^2(\mathbf{x}_n) + \frac{(\mu_i(\mathbf{x}_n) - y_n)^2}{\sigma_i^2(\mathbf{x}_n)} \right) \text{StopGrad}(\sigma_i^{2\beta}) \quad (3.2)$$

for example n and model i , with an implicit expectation over training examples. $\beta = 0$ yields the original Gaussian NLL loss function and $\beta = 1$ yields the MSE loss function, so introducing a β factor can be interpreted as interpolating between these two loss functions. Thus, this factor improves MSE performance by scaling via an effective learning rate for each example (which is why StopGrad is used) [?], and may also improve both aleatoric and epistemic uncertainty quantification [?]. $\beta = 0.5$ was used by default in this study. This β -NLL loss function also improved training stability.

This typical negative-log likelihood loss assumes the prediction – the likelihood of y given input \mathbf{x} : $p(y|\mathbf{x})$ – follows a Gaussian distribution. Treating each prediction as an independent random variable (considering each model in the ensemble is sampled from some weight distribution $\theta \sim p(\theta|\mathbf{x}, y)$) and finding the mean of the random variables yields a normal distribution with mean $\mu_*(\mathbf{x}) = \langle \mu_i(\mathbf{x}) \rangle$ and variance $\sigma_*^2 = \langle \sigma_i^2(\mathbf{x}) + \mu_i^2(\mathbf{x}) \rangle - \mu_*^2(\mathbf{x})$ where $\langle \rangle$ indicates an average over the ensemble.

The ensemble predictive uncertainty can be broken down into the aleatoric and epistemic components [?]: the aleatoric uncertainty is $\langle \sigma_i^2(\mathbf{x}) \rangle$ and the epistemic uncertainty is $\langle \mu_i^2(\mathbf{x}) \rangle - \mu_*^2(\mathbf{x}) = \text{Var}[\mu_i(\mathbf{x})]$. The intuition behind these uncertainties is that the random fluctuations in the recorded data are captured in the variance of a single network, σ_i^2 , so the average of these variances represents that sort of randomness present. If the choice of model were to make a significant difference, we'd expect the predicted mean for a single model, μ_i , to fluctuate quite a bit, which is captured

by $\text{Var}[\mu_i(\mathbf{x})]$.

Modifying the learning rate over time (also known as scheduling) is known to improve model learning. A few schedules were tried: constant learning rate ($\gamma = 3 \times 10^{-4}$), $\gamma \propto \text{epoch}^{-1}$, $\gamma \propto \exp(\text{epoch})$, and $\gamma \propto \text{epoch}^{-1/2}$. The epoch is the training step divided by the number of batches in one epoch, so “epoch” in this case takes on a floating-point value. $\gamma \propto \text{epoch}^{-1}$ appears to give the best test set loss by a test MSE of 1×10^{-4} , and any schedule beats a constant learning rate by $2 - 4 \times 10^{-4}$.

3.4.2 Cross-validation MSE

Multiple train-test set pairs were created. Test set 0 is the hand-picked dataset, chosen to contain a diverse set of machine settings and probe movements. The other six were randomly compiled without replacement while keeping the number of dataruns from DR1 and DR2 equal. Seven model ensembles (35 NNs total) were trained to evaluate the effect of test set choice on perceived model performance. The median ensemble test set MSE for these seven sets was 2.13×10^{-3} with a mean of 3.6×10^{-3} . The handpicked dataset had an ensemble test set MSE of 1.85×10^{-3} , indicating that the choice of dataruns was adequately representative because the MSE is close to the median cross-validated value. This median MSE will be used to estimate model prediction error in addition to uncertainty quantification. This cross-validation also provides an error estimate if the models were to be trained on *all* dataruns. It was also seen that ensembles always out-perform the average single-model prediction.

3.4.3 Model calibration via weight decay

An attempt is made to calibrate the model uncertainty. The predicted uncertainty may not provide a suitable predicted I_{sat} range when compared to the measured value. Calibrating the model means changing the predicted uncertainty range so that the real, measured values fall within that range according to some distribution, such as a Gaussian in this case. One of the ways assessing this

calibration is by the z-score of predictions, where $z_n = x_n - \mu_n / \sigma_n(x_n)$ for example x_n , predicted mean μ_n , and standard deviation σ_n . Perfect model calibration would mean an identical z-score distribution $\mathcal{N}(\mu = 0, \sigma = 1)$ for the training and test sets. When evaluated on the training set, the training set z-score distribution is consistent with this Gaussian distribution. The standard deviation of this z-score distribution should be 1.

Increased weight decay can lead to better model calibration [?]. Many ensembles were trained to determine the best weight decay coefficient between 0 and 50, determined by the distribution of z-scores of the training and test examples, seen in fig. 3.2. Increasing the weight decay increases the test MSE and decreases its z-score standard deviation. This large standard deviation is caused by outliers. Excluding z-scores magnitudes above 10, or 4.4% of the test set, yields a standard deviation of 2.53. Nonetheless, the trend remains that increasing weight decay leads to smaller test set z-score standard deviations. However, the test set MSE increases after a weight decay of 1. This increase in test MSE means that the model is making less accurate predictions, but the model is better calibrated. Highly biased models are better calibrated, but come at great expense of mean prediction error. At the weight decay value of 50, the model has worse error than a linear model. Despite the attempts using weight decay, the model never becomes well-calibrated: the predicted uncertainty is always too low by a factor of 2 to 5.

Despite the better calibration, the uncertainty predicted by the model is decidedly worse: the uncertainty is similar across an entire profile, and when projected beyond the training data, the total uncertainty remains largely constant. See fig. 3.3. On the other hand, the zero weight decay model exhibits relatively increasing uncertainty beyond the bounds of the training data. Although not well-calibrated, this uncertainty can provide a hint of where the model lacks confidence relative to other predictions, even though the uncertainty is much less than it should be.

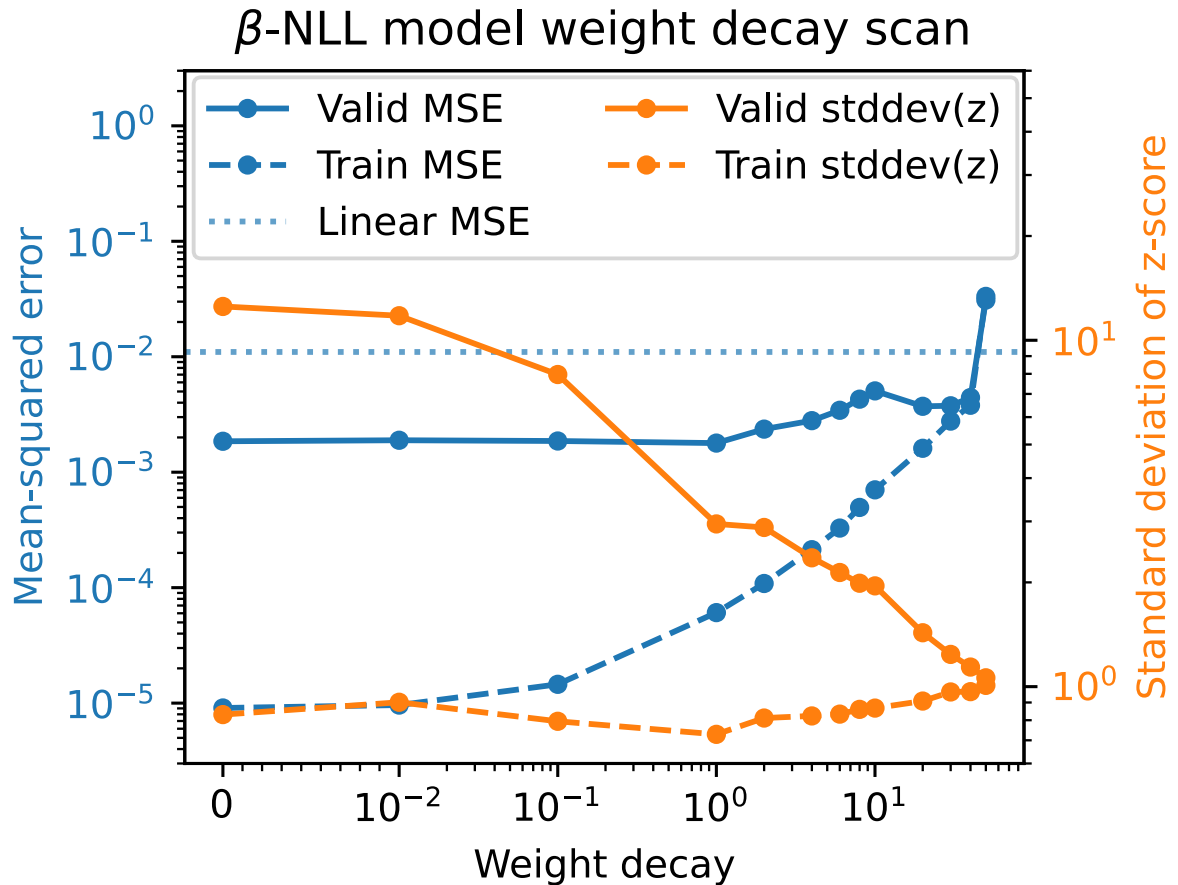


Figure 3.2: Model performance and calibration for different weight decays. Highly biased models are better calibrated, but come at great expense of mean prediction error. At the weight decay value of 50, the model has worse error than a linear model. Note the linear scale below 10^{-2} .

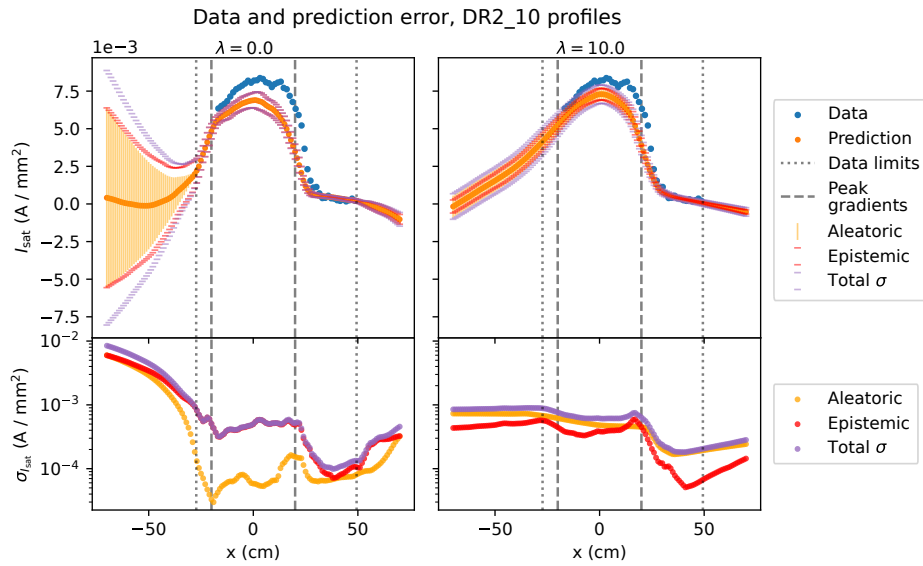


Figure 3.3: Model extrapolation performance (top plots) with uncertainty (bottom plots) for a model ensemble trained on a β -NLL loss function. DR2 run 10 was chosen as an illustrative example. The *relative* uncertainty appears to be more useful when zero weight decay ($\lambda = 0$, left) is used: the uncertainty increases when the model is predicting outside its training data along the x-axis.

3.5 Evaluating model performance

Model performance is evaluated in three ways by comparing against intuition from geometry, an absolute measurement, and extrapolated machine conditions.

3.5.1 Checking geometrical intuition

From geometric arguments (and experience), we know that modifying the mirror geometry can control the effective width of the plasma. One way to check that the machine model is learning appropriate trends is to check with this intuition. Namely, when the magnetic field at the source is not equal to the field at the probe, the probe will see the plasma expanded (or contracted) by roughly a factor of $\sqrt{B_{\text{probe}}/B_{\text{source}}}$. The cathode is about 35 cm in diameter, so a magnetic field ratio of 3 would give produce a plasma approximately 60 cm in diameter. All the probes used in this study are in or very close to the zero-curvature region of a mirror.

TODO: the end of this section doesn't match the plot. To check this intuition, the model is given the following inputs: $B_{\text{source}}=500$ G, $B_{\text{mirror}}=1500$ G, $B_{\text{midplane}}=500$ G, discharge voltage=110 V, gas puff voltage=70 V, gas puff duration=38 ms, run set flag=DR2 and top gas puff=off. The discharge voltage and gas puffing parameters were arbitrarily chosen. The x coordinate is scanned from 0 to 30 cm, and the z coordinate from 640 to 1140 cm. This discharge is then modified by separately changing B_{source} to 1500 G and B_{midplane} to 750 G ($M=1.5$). The x profiles at the midplane ($z=790$ cm) of the reference $M=3$ prediction, source field change, and midplane field change, all scaled to cathode radius, can be seen in fig. 3.4. Changing the source field to 1500 G increases the I_{sat} towards the edge of the plasma, as expected. When the midplane field is increased, the I_{sat} values decrease at the edge and increase at the core ($x=0$ cm), which implies a thinner plasma column and is consistent with previously measured behavior. When only the mirror field is modified, the strongest effect on I_{sat} is on or near $x=0$ cm, and the plasma column width does not appear to appreciably change. Strong axial I_{sat} gradients are present in these predicted discharges.

Predicted x profiles in mirrors at the midplane

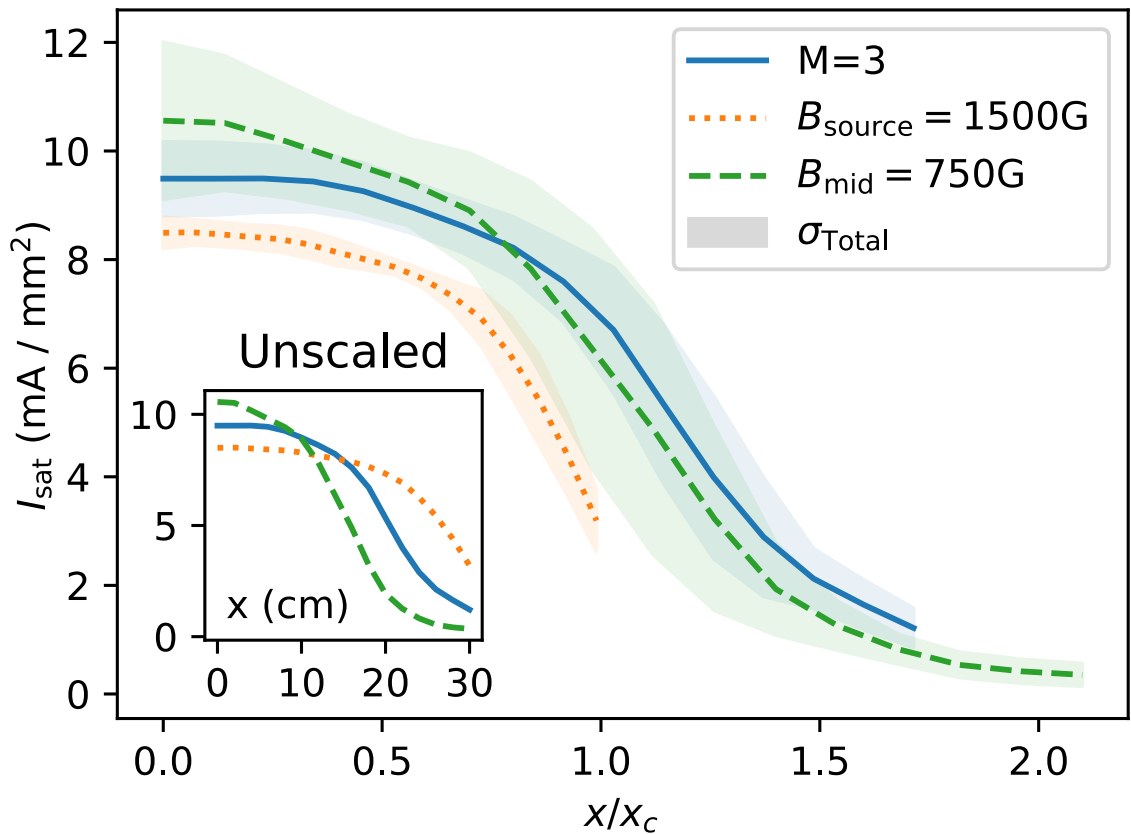


Figure 3.4: Plot of various mirror configurations scaled to the cathode radius $x_c = 17.5$ cm at the midplane ($z=790$ cm). When scaled according to the expected magnetic expansion, the profiles generally agree. The smaller the plasma diameter (and thus smaller volume), the higher the peak in I_{sat} at the core, as expected.

3.5.2 Directly comparing prediction to measurement

I_{sat} measurements were taken with the following LAPD machine settings: $B_{\text{source}}=1250 \text{ G}$, $B_{\text{mirror}}=500 \text{ G}$, $B_{\text{midplane}}=1500 \text{ G}$, discharge voltage=90 V, gas puff voltage=90 V, gas puff duration=38 ms, run set flag=DR2 and top gas puff=off. These settings were from a previous discharge optimization attempt. The probes utilized were the permanently-mounted 45° probe drives. These probes were known to have identical effective areas relative to each other from the previous experiment and from analyzing the discharge rampup.

Because of data acquisition issues, only a single useful shot was collected at a nominal -45° angle 10 cm past the center ($x=0 \text{ cm}$, $y=0 \text{ cm}$) of the plasma on three probes at z-positions of 990, 767, and 607 cm (ports 22, 29, and 34, respectively). The probe drives were slightly uncentered, leading to the real coordinates of the probes to be around $x = 9.75 \text{ cm}$ and $y = -8.4 \text{ cm}$. Note that the model can predict anywhere in LAPD bounded by the training data, so off-axis measurements are not an issue. The resulting predictions using these coordinates and machine conditions can be seen in fig. 3.5. The model reproduces the axial trend well, but slightly underestimates I_{sat} on an absolute comparison. However, given the lack of absolute I_{sat} calibration for both this validation datarun and the training data, the agreement of the absolute I_{sat} values may be coincidental. Additionally, the cathode appeared to be in a low-emissivity state that is, at the moment, not well understood. Nevertheless, the axial trends match.

An additional validation datarun was performed. For this run, the discharge voltage was increased to 160 V, and the source field changed to 822 G. The training data contains discharge voltages up to 150 V, so this case tests the extrapolation capabilities of the model. The comparison of model predictions and the measured data can be seen in fig. 3.6. As stated earlier, the absolute uncertainty provided of the model is not calibrated. However, note that the level of uncertainty provided by the model, as well as the large spread in model predictions, are much greater than seen in the interpolation regime (fig. 3.5) and eclipses the cross-validated test set RMSE. We conclude that this model has good interpolation capabilities, but extrapolation – as with any model –

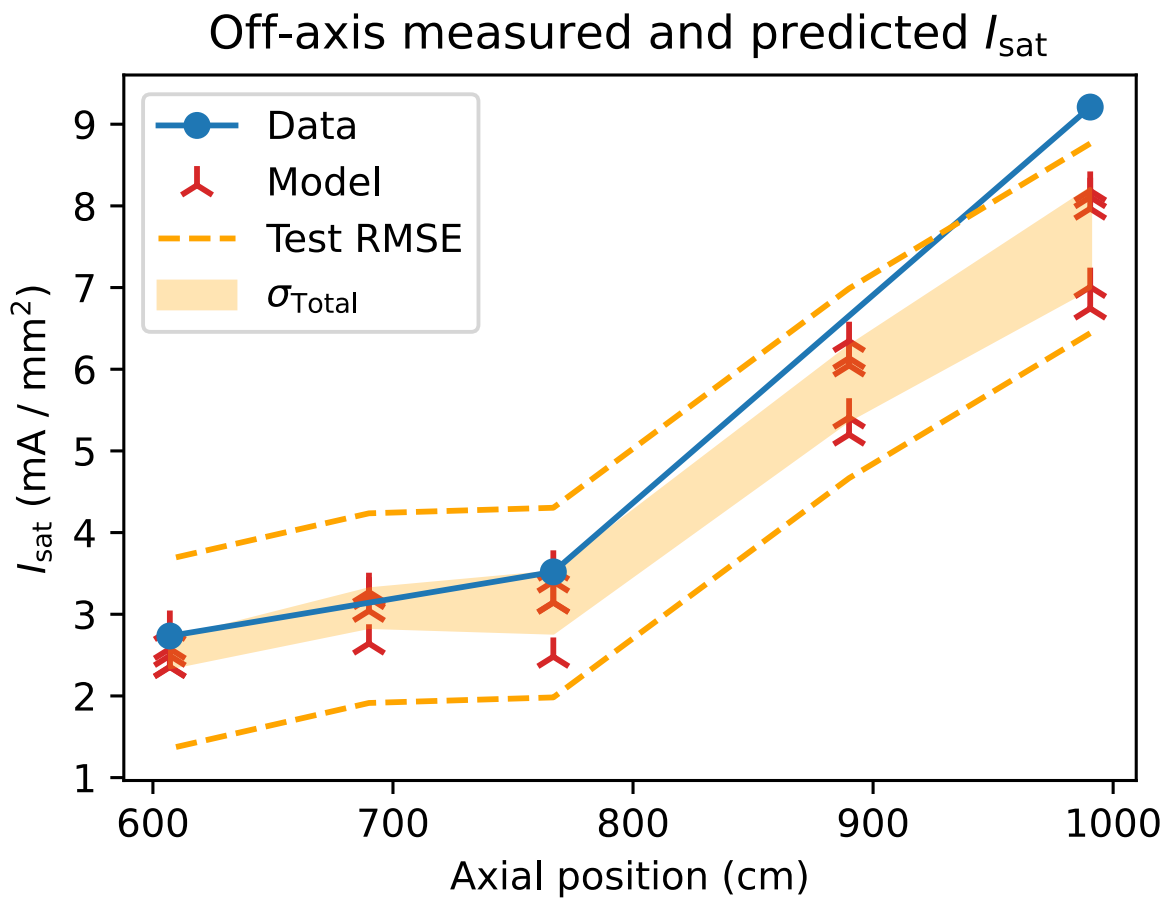


Figure 3.5: Data collected at off-axis positions around $x = 9.75$ cm and $y = -8.4$ cm are compared with predictions from the machine learning model at the same points in addition to two interpolating predictions. The model predicts the trend well, but underestimates I_{sat} in general. The shaded orange region is the total model uncertainty ($\sigma = \sqrt{\text{Var}}$).

remains difficult.

3.6 Inferring trends

A systematic study of the impact of discharge voltages on I_{sat} profiles has not been performed. Collecting both z- and x-axis profiles over a wide range of discharge voltages would take a considerable amount of time, mostly from the requirement to dismount and reattach the probes and probe drives along the length of the LAPD. We perform this study in silico using the learned model. Model input parameters were chosen to be common, reasonable values: 1 kG flat field, 80 V gas puff, 38 ms gas puff duration, run set=DR2, and top gas puff off. The 38 ms puff is used in these predictions because it is the most common gas puff duration in the training set, so the model is biased in favor of this gas puff setting. The results of changing the discharge voltage only can be seen in fig 3.7. Notably, the I_{sat} increases across both axes. Steeper axial gradients are seen with lower discharge voltages, but peaked x-profiles are seen at higher discharge voltages. The area closer to the source region (+z direction) appears to have a steep drop but flatter profiles down the length of the machine.

Unfortunately the discharge current was not included as an output in the training set. Otherwise the effect of changes in discharge power, rather than simply voltage, could be computed. The discharge current – and thus discharge power – is set by cathode condition, cathode heater settings, and the downstream machine configuration, and thus cannot be set to a desired value easily before the discharge. Discharge voltage, however, can remain fixed.

TODO: get plot from Shreekrishna?

Of particular interest for some LAPD users is achieving the flattest possible axial profile. We explore this problem in the context of mirrors. The gas puff duration is known to be a large actuator for controlling density and temperature and so is explored as a way of shaping the axial profile. We predict discharges with a flat 1 kG field with the probe in the center. The discharge voltage was set at 110 (a reasonable, middle value) with the run set flag=DR2 and top gas puffing=off. The

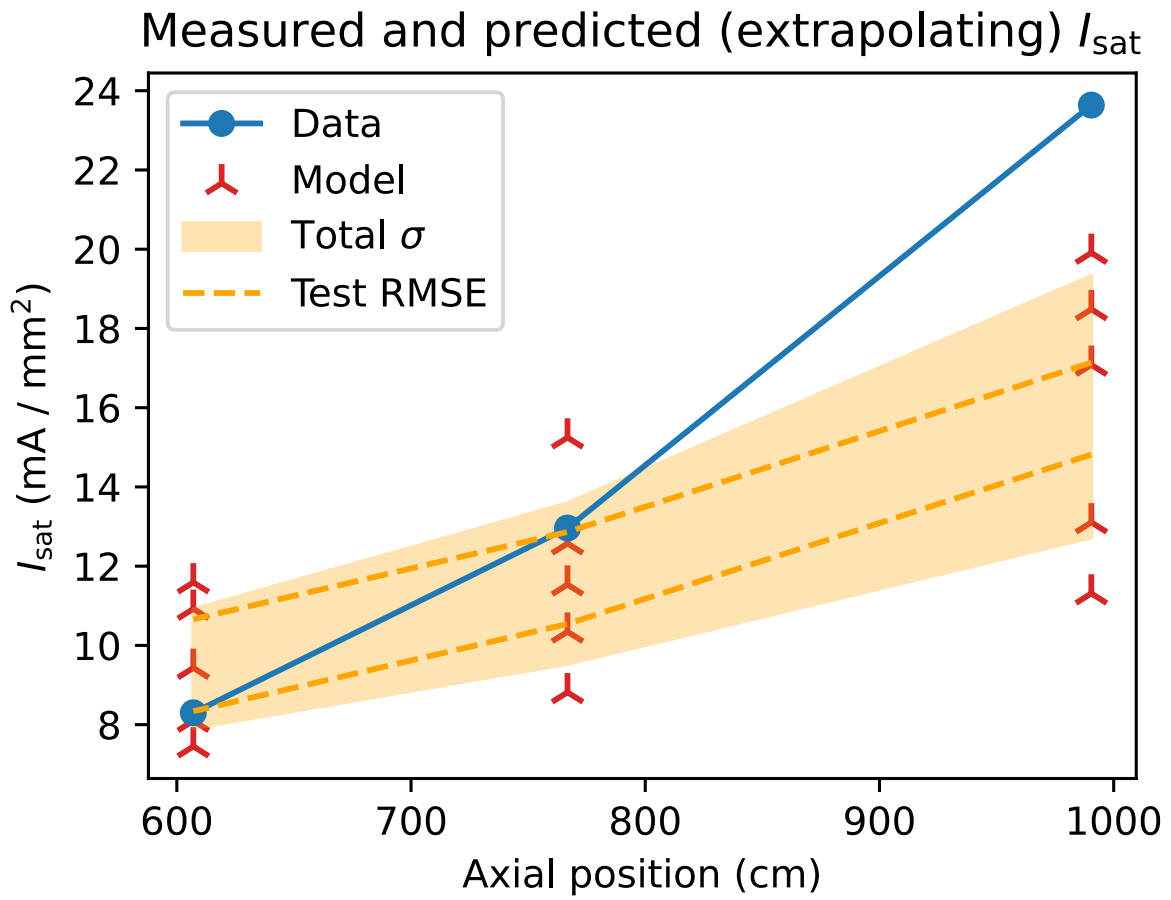


Figure 3.6: Measured vs predicted I_{sat} values for an odd machine configuration with $B_{\text{source}}=822$ G and discharge voltage=160 V. The training data only covers discharge voltages up to 150 V. The machine was also in an odd discharge state, so it's no surprise that the predicted uncertainty bounds are very large (even greater than the test set RMSE value) and that accuracy suffers.

Discharge voltage: effect on x and z profiles

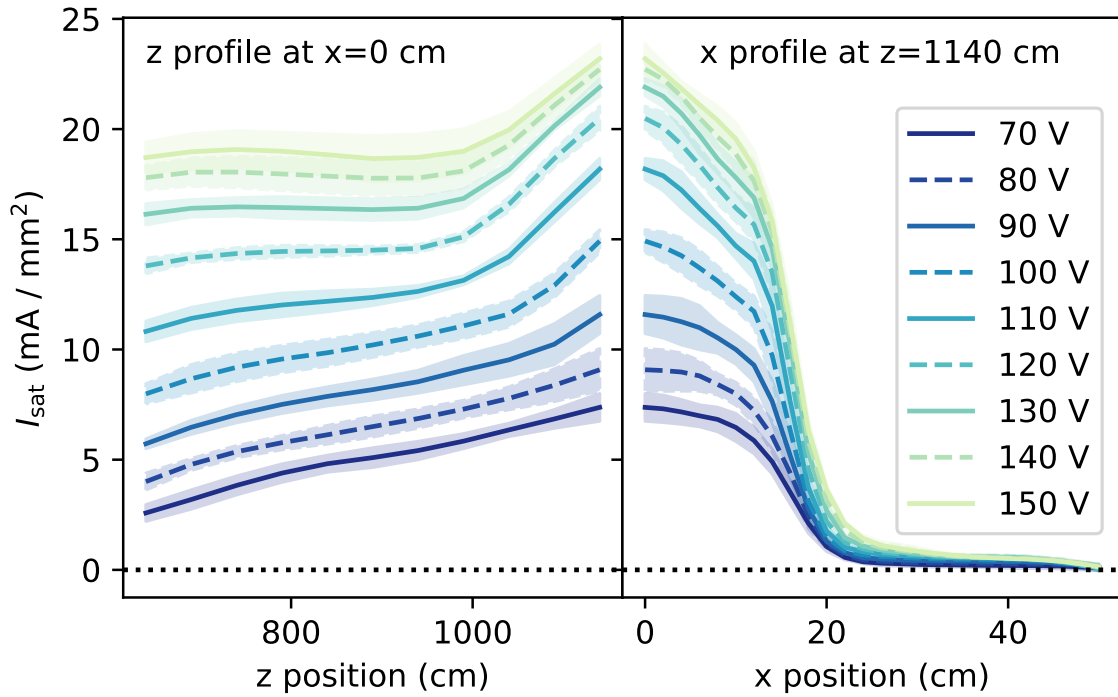


Figure 3.7: The z profile at $x=0 \text{ cm}$ and x profile at $z=1140 \text{ cm}$ for different discharge voltages. The I_{sat} decreases with increasing voltage, and the error (filled regions) stays roughly the same, but in general increase slightly towards the cathode and at higher discharge voltages.

inferred effect of gas puff duration on the axial gradient and axial gradient scale length can be seen in fig. 3.8. Care was taken to handle the aleatoric (independent) uncertainty separately from the axially-dependent epistemic uncertainty. As seen in the figure, the mean axial gradient decreases when the gas puff duration is shortened. The gradient scale length also increases, so the mean gradient is not decreasing simply because the bulk I_{sat} is decreasing. This result suggests that the gas puff duration may be a useful actuator to consider when planning future experiments.

These applicability of these results are somewhat muted because the gas puff duration was not chosen randomly in the training discharges. Only 6 runs in the training set had gas puff durations less than 38 ms. Three were 5 ms, three were 10 ms, with each having mirror ratios 1, 3, and 6 and otherwise identical configurations. The 20 ms gas puff duration datarun was in the test set. Given this lack of data diversity, the accuracy and applicability of this study must be interpreted cautiously. When a model is trained on *all* data available (using the cross-validated test set MSE as a guide for error), which includes the 20 ms gas puff case, the predicted gradient scale length decreases uniformly across the duration scan by 1 meter. The fact that the trend remains intact when an additional, randomized intermediate gas puff case is added gives confidence in the predictions of the model despite the lack of data diversity.

3.7 Optimizing profiles

One particular issue seen in LAPD plasmas is sharp axial density and temperature gradients. Some experiments require flat gradients, such as Alfvén wave propagation studies. We explore optimizing the axial I_{sat} variation as an approximation to this problem. In addition, in this case the optimization problem is used as a tool to evaluate the quality of the learned model. This is a very demanding task because the trends inferred by the model along all inputs must simultaneously be accurate. Constraints on this optimization further increase the difficulty of the problem. Success in optimization provides strong evidence that the model has inferred relevant trends in predicting I_{sat} . We quantify the flatness of the axial profile by taking the standard deviation of I_{sat} of 11 points

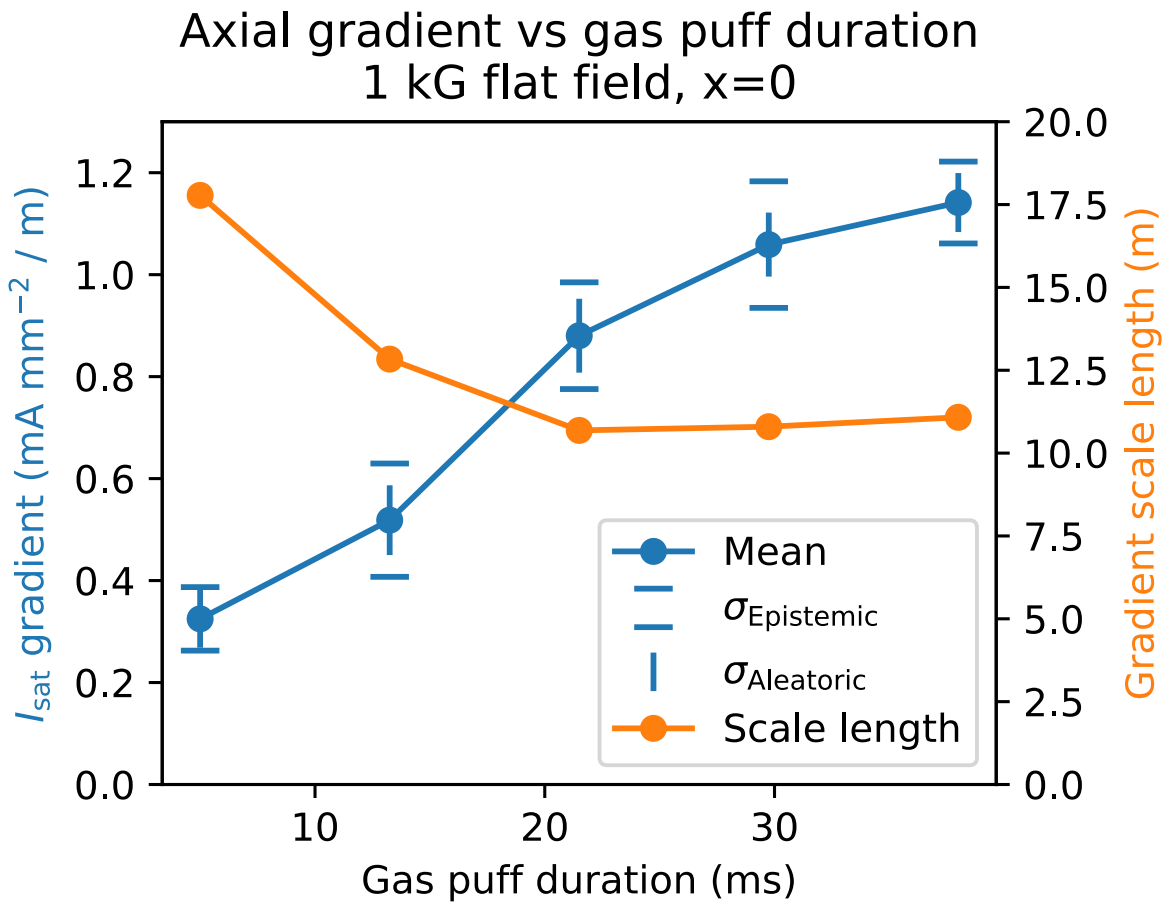


Figure 3.8: ML prediction: mean axial gradients decrease with decreased gas puff duration. Five durations are plotted between 5 and 38 ms (which are the bounds of the training data), evenly spaced. The gradient scale length also increases, indicating that the gradient change was not just from a decrease in the bulk I_{sat} .

Table 3.2: Machine inputs and actuators for model inference

Input or actuator	Range	Step	Count
Source field	500 G to 2000 G	250 G	7
Mirror field	250 G to 1500 G	250 G	6
Midplane field	250 G to 1500 G	250 G	6
Gas puff voltage	70 V to 90 V	5 V	5
Discharge voltage	70 V to 150 V	10 V	9
Gas puff duration	5 ms to 38 ms	8.25 ms	5
Probe x positions	-50 cm to 50 cm	2 cm	51
Probe y positions	0 cm	—	—
Probe z positions	640 cm to 1140 cm	50 cm	11
Probe angle	0 rad	—	—
Run set flag	off and on	1	2
Top gas puff flag	off and on	1	2

along the z-axis ($x, y = 0$). The required LAPD state for attaining the flattest possible axial profile can be found by finding the minimum of this standard deviation with respect to the LAPD actuators (model inputs):

$$\text{Inputs} = \arg \min_{\substack{\text{Inputs} \neq z}} \text{sd}(I_{\text{sat}}|_{x=0}) \quad (3.3)$$

The largest axial variation can likewise be found by finding the maximum. The model inputs used for this optimization can be found in table 3.2.

For this optimization we use an ensemble of five β -NLL-loss models with weight decay $\lambda = 0$. The $\lambda = 0$ model is used because it appears to give the most useful uncertainty estimate (seen fig. 3.3). The optimal machine actuator states are found by feeding a grid of inputs into the neural network. This variance estimate is not well-calibrated: the error of the predictions on the test set falls far outside the predicted uncertainty. However, this uncertainty can be used in a relative way: when the model is predicting far outside its training range, the predicted variance is much

larger. The ranges of inputs into this model are seen in table 3.2. These inputs yield 127,234,800 different machine states (times five models) which takes 151 seconds to process on an RTX 3090 (\approx 4.2 million forward passes per second) when implemented in a naive way. Note that gradient-based methods can be used for search because the network is differentiable everywhere but this network and parameter space is sufficiently small that a comprehensive search is tractable.

Like any optimization method, the results may be pathologically optimal. In this scenario, the unconstrained minimal axial variation is found when the I_{sat} is only around 1 mA/mm², which is quite small and corresponds to $1\text{-}2 \times 10^{12}$ cm⁻³ depending on Te. The inputs corresponding to this optimum are in the second column of table 3.3. This density range is below what is required or useful for many studies in the LAPD.

Since many physics studies require higher densities, we constrain the mean axial I_{sat} value to be greater than 7.5 mA/mm² (roughly $0.5\text{-}2 \times 10^{13}$ cm⁻³). The “run set flag” is set to “on” for cases to be validated (bolded in table 3.3) because we wish to keep the turbopumps on to represent typical LAPD operating conditions. In addition the “top gas puff flag” was set to ‘off’ to minimize the complexity of operating the fueling system on followup dataruns and experiments. Turning the top gas puff valve on is predicted to decrease the average I_{sat} by -2 mA/mm² for strongly varying profiles, but otherwise the shapes are very similar. The inputs corresponding to the maximum and minimum axial variation under these constraints can be seen in columns 3 and 4 of table 3.3. Out of curiosity we also consider what machine settings would lead to the greatest axial variation. The results of both of these optimizations can be seen in fig. 3.9. The optimizations yield profiles that have the largest I_{sat} values closest to the cathode, which is expected.

The predictions for the strongest, weakest, and intermediate axial variation cases is seen in fig. 3.9. The intermediate case was chosen as somewhere around half way between the strongest and weakest case with a round index number (15000, in this case). The parameters for intermediate case are also enumerated in table 3.3.

The predicted configurations with the run set flag on and top gas puff flag off (bolded in table 3.3 were then applied on the LAPD. The data collected, compared with the predictions can be seen

Table 3.3: Machine inputs and actuators for optimized axial profiles

Input or actuator	Weakest	Weakest	Strongest	Intermediate
I_{sat} constraint (mA/mm^2)	$I_{\text{sat}} = \text{any}$	$I_{\text{sat}} > 7.5$	$I_{\text{sat}} > 7.5$	$I_{\text{sat}} > 7.5$
Source field	750 G	1000 G	500 G	2000 G
Mirror field	1000 G	750 G	500 G	1250 G
Midplane field	250 G	250 G	1500 G	750 G
Gas puff voltage	70 V	75 V	90 V	90 V
Discharge voltage	130 V	150 V	150 V	120 V
Gas puff duration	5 ms	5 ms	38 ms	38 ms
Run set flag	on	on	on	on
Top gas puff flag	on	off	off	off

in fig. 3.9.

For the optimized axial profiles, the absolute value of the I_{sat} predictions compared to measurement do not agree. All of the predicted profiles have overlapping predictions (within the predicted error) at the region furthest from the cathode, but the measured values do not show that behavior. Although the mean I_{sat} value was constrained to be greater than 7.5 mA/mm^2 , the measured mean was 2 mA/mm^2 for the weakest case. Despite these lack of absolute

The important thing here, however, is that the optimized LAPD settings, when implemented on the machine, do yield profiles with strong, intermediate, and weak axial variation. Although the minimum- I_{sat} constraint was violated for the case of weakest axial variation case, this optimization would nonetheless be very useful for creating axial profiles of the desired shape.

There are three contributing factors to the mismatch of the ML-predicted values and the real measured values. First, the condition of the cathode, such as its emissivity or temperature, in the plasma source region is unquantified and cannot be compensated for in data preprocessing or in the model itself. Second, the calibration of the Langmuir probes could differ substantially between runs. The probes in the training data run sets (DR1 and DR2) were well-calibrated to each

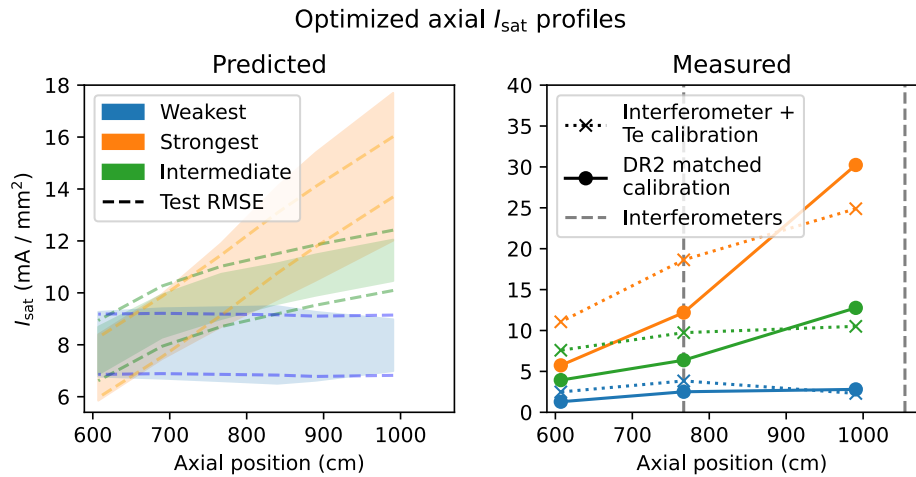


Figure 3.9: Axial profiles, predicted and measured, for the optimized weakest (blue), intermediate (green), and strongest (orange) cases. a. The shaded region covers the mean prediction \pm one standard deviation, and the dashed lines are \pm the median cross-validation RMSE values. b. The measured I_{sat} values are calibrated to DR2 run 10 (solid lines), or using triple probe Te measurements on the probe and linearly extrapolating the interferometer measurements (dotted lines). The absolute values disagree between the predicted and measured values, but axial trends are consistent with the optimization.

other within the run set, but were not absolutely calibrated. The probes used for verifying the optimization were not calibrated. A rough calibration was performed by linearly extrapolating interferometer measurements and using triple probes (dotted lines on the right panel in fig. 3.9). A configuration identical to DR2 run 10 was also measured to simultaneously correct cathode condition and probe calibration (solid lines on the right panel in fig. 3.9). Langmuir probe calibration is discussed further in 3.13 Third, the original dataset may not have sufficient diversity to make accurate predictions on such a constrained optimization problem.

If this optimization were performed using the dataset instead of the model, the constrained search would encompass just 10084 shots out of the 131550 shots total in the training dataset, or around 7.7%!. Including the on-axis constraint reduces the number of shots down to 303 (270 in the training set), or 0.23% of all shots in the dataset. We conclude that this optimization of an arbitrary objective function, as done here, would be intractable using traditional, non-machine learning techniques because orders of magnitude more dataruns would need to be collected.

Optimization requires correctly learning the trends of all inputs and how they interact. In addition, as seen from the shot statistics, the model was trained on very few shots in the constrained input and output space. These two factors – the need for the model to learn all trends and the constrained search space – combine to make an incredibly difficult task that functions as a benchmark for the model. These factors considered, it is not surprising that the model incorrectly predicts the absolute value. The uncertainty predicted by the model, though not well-calibrated, was nonetheless very large compared to the median test set RMSE, which indicates that the model was very uncertain. The model did get the trends correct, however; the optimized, measured profiles were strong, intermediate, or weak.

We did not check to see if the predicted optima were actually optima: an approximation of the local derivative using a finite-differenced technique would require much more run time on the LAPD than was available.

3.8 Discussion

3.8.1 Key achievements

TODO: Expand discussion on uncertainty and why it's important

To the authors' knowledge, this is the first time machine learning has been used to infer specific trends in magnetized plasmas and introduces the first open magnetized plasma dataset. Three examples of trend inference were shown in this paper: influence of magnetic geometry on plasma width, changes in the axial and radial profiles with changing discharge voltage, and the relationship of gas puff duration with axial gradient scale length. In addition, the axial profile was optimized by minimizing (or maximizing) the axial standard deviation. There is no other way of simultaneously uncovering many trends or finding optima without using an ML model over a diverse dataset. Traditionally, such studies would require extensive scans over grids to map the parameter space, but here it was accomplished with minimal data.

The trends inferred in this work, such as changing discharge voltages, gas puff durations, or mirror fields, would traditionally require a grid scan (varying one parameter at a time) in LAPD settings space. Here instead we are able to extract any trend covered by the training set with only a minimal amount of machine configurations sampled. Both data collection runs lacked absolute I_{sat} calibration and had potential differences in cathode condition. Despite these issues the model learned trends that were exploited via optimization.

Fundamentally, this model can predict I_{sat} with uncertainty at any point in space covered by the training data. No other model exists that can perform this prediction. Traditionally this sort of capability would be possible only with a detailed and validated theoretical study.

3.8.2 Current limitations

This study would be dramatically improved by collect more, diverse data. Only 44 of the 67 dataruns in this dataset were randomly sampled which is very small compared to the over 60,000

possible combinations in LAPD settings. In addition, there are many other LAPD settings that were not changed in this study, such as gas puff timings, gas puff valve asymmetries, wall/limiter biasing, cathode heater settings, operation of the north cathode, and so on. The bounds of the inputs were also conservative; all settings in this study could be pushed higher or lower with a small amount of risk to LAPD operations. In addition, the placement of the probes can be further varied and place outside the mirror cell, which would provide a more complete picture of LAPD plasmas and particularly axial effects.

Probe calibrations differed between the two training run sets (DR1 and DR2), and a flag was introduced for the model to distinguish between them, but despite this deficiency combining the two run sets was advantageous for model performance. The condition of the cathode (e.g., electron emissivity and uniformity) also has a large impact on the measured I_{sat} . The improved model performance with the flag suggests that inconsistencies between dataruns could be compensated for using latent variables if a generative modeling approach is to be taken. At the very least, this model provides a way to benchmark these differences in machine state.

On the model side, hyperparameter tuning can also be done. In this study we were not interested in squeezing out a few extra percent in MSE performance. Instead, we wanted to focus on the trends and insights that can be extracted from this model, rather than simple predictive accuracy. There may also be regimes in hyperparameter space where the uncertainty is better calibrated (perhaps using early stopping). Uncertainty estimation is important, even if the absolute uncertainty is not well-calibrated, because it can provide a useful relative estimate like what was shown in this paper.

3.8.3 Future directions

The neural network architecture used here can readily scale to additional inputs and outputs; including time-series signals is the obvious next step. Integration of multiple diagnostics – perhaps starting with individual models before combining them – could enable inference of plasma pa-

rameters throughout the device volume. For example, combining triple probe electron temperature measurements with existing I_{sat} data would allow density predictions anywhere in the plasma. This capability could enable in-situ diagnostic cross-calibration (e.g., the Thomson scattering density measurement) and prediction of higher-order distribution moments like particle flux. The model could be further enhanced by incorporating physics constraints such as boundary conditions (e.g., zero I_{sat} at the machine wall) or symmetries.

The problem presented here – learning time-averaged I_{sat} trends – is fairly simple and required a relatively simple model. As demonstrated in this work, ML provides a way to explore regions of parameter space quickly and efficiently. Most physics studies on plasma devices (and fusion devices) are dedicated to a single particular problem, use grid scans, and are not useful to other experiments or campaigns. This work shows a way of using data and trends uncovered from other experimental studies. This work also demonstrates that random exploration can be a useful tool: the increased diversity of the aggregated data will always benefit an ML model whether or not the experiment discovers something new.

3.9 Conclusion

We demonstrate the first randomized experiments in a magnetized plasma experiment to train a neural network model. This learned model was then used to infer trends when changing field configuration, discharge voltage, or gas puff duration. This model was also used to optimize axial variation as measured by the standard deviation, which was validated in later experiments despite poor absolute error.

We strongly advocate that all ML-based analyses in fusion should validate their models and gain insight by inferring trends, as demonstrated here. This validation step is crucial for ensuring that ML models capture physically meaningful relationships and the insights provided may provide direction for future research. We hope this is the first step towards automating fusion science.

Measured and predicted I_{sat} for DR2 run 10

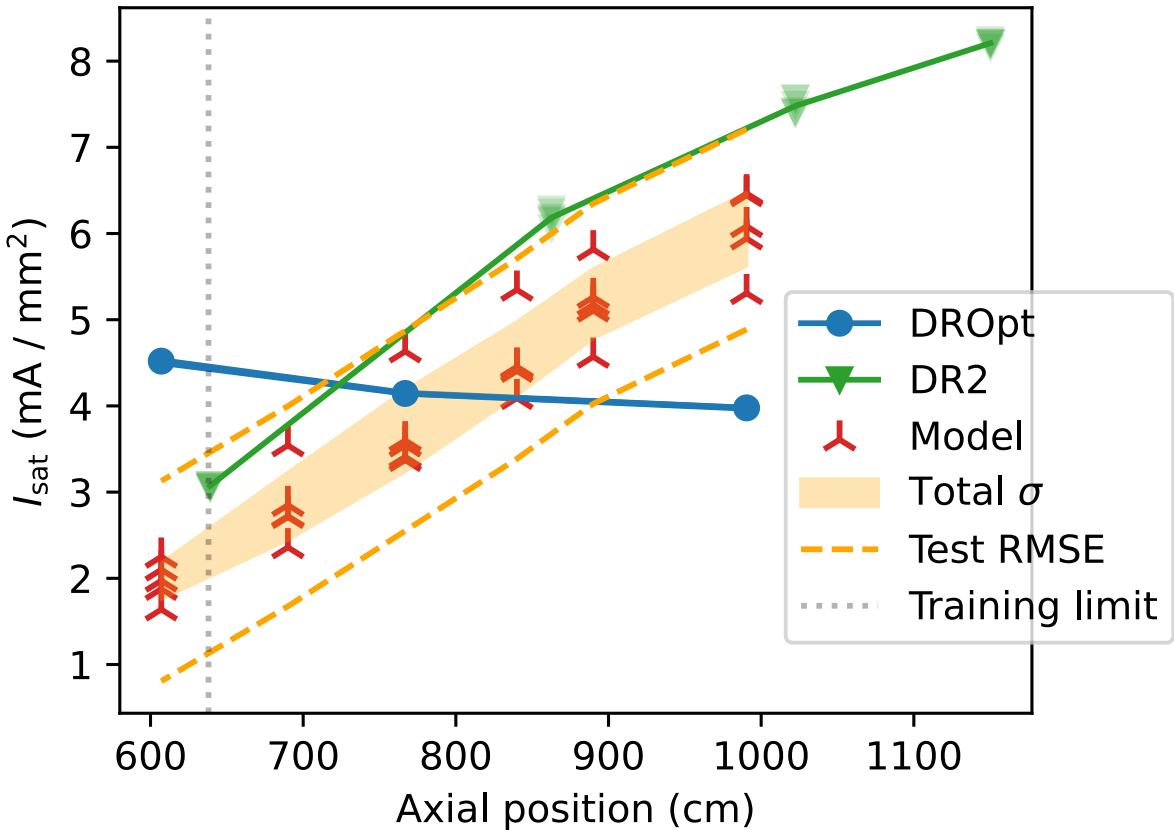


Figure 3.10: Comparison of original DR2 profiles with the profiles from the optimization dataset (DROpt) for the same machine configuration. The I_{sat} values in the DROpt dataset are not calibrated in this plot, indicating significant variation in probe calibration in this DROpt dataset.

Loss and MSE over epochs, model 1 of 5

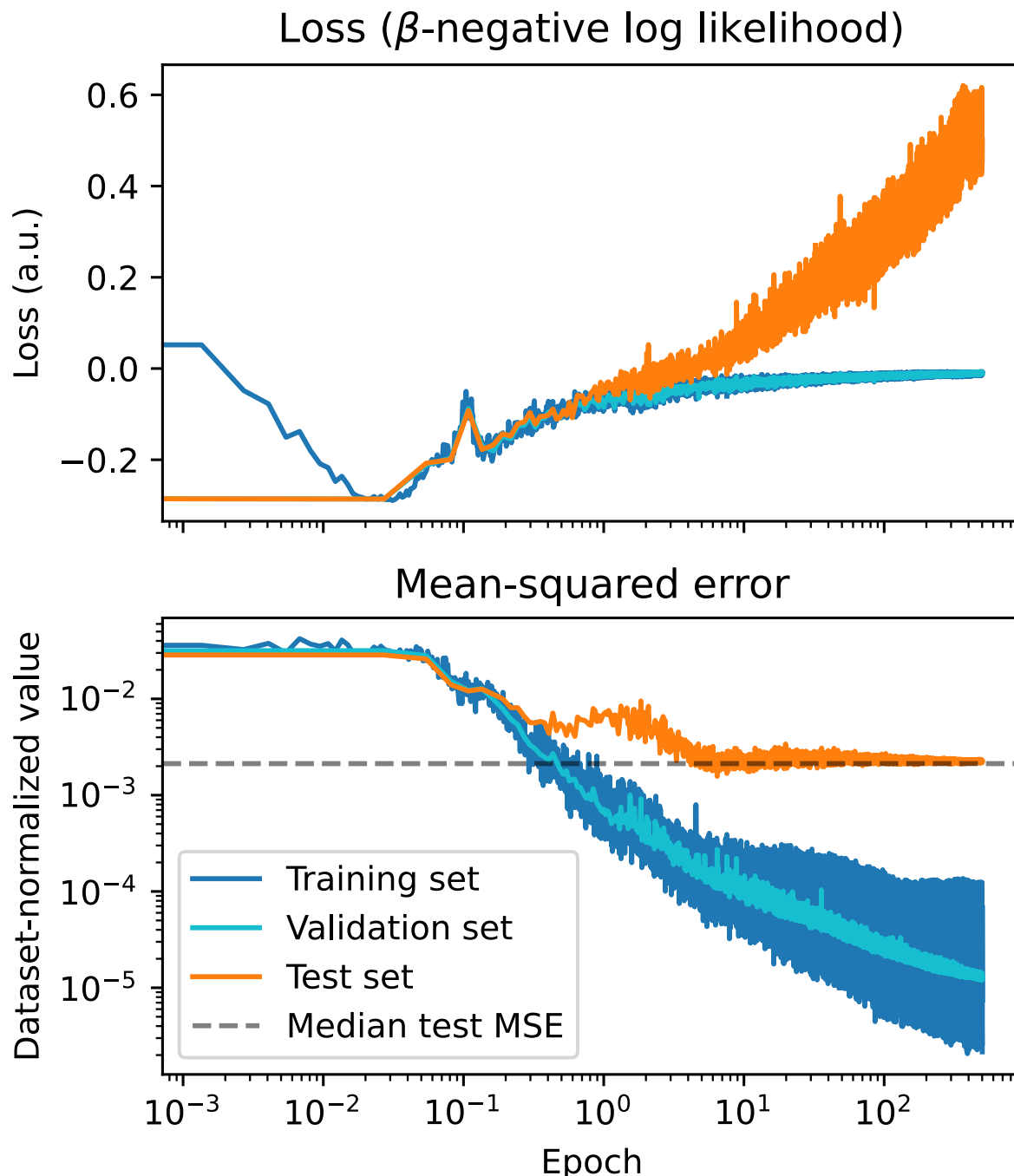


Figure 3.11: The loss and MSE for the training, validation, and test sets over the entire training duration of 500 epochs. The inclusion of the β term in the loss function – interpreted as a per-example learning rate – makes the loss function no longer interpretable in simple terms.⁹⁰ The mean-squared error benefits from longer training for all sets.

3.10 The open dataset and repository

All the code to perform the ML portion of this study is available at this github repository: <https://github.com/p>. The training datasets are also available in that repository in the datasets directory. Additional data are available upon request. This is the first open dataset from a magnetized plasma device.

The plots used in this paper were made in jupyter notebooks, which are also uploaded. The final training code can be found in `train_dense_beta_NLL.py`. Trained models are found in the `code/training_runs` directory.

The history of many training runs can be found on Weights and Biases: <https://wandb.ai/phill/profile-p> and the accompanying notes on these trained models are found in the associated pdf: TODO: upload pdf.

TODO: Improve github readme and upload new stuff

3.11 Data bias

Despite the best efforts to randomize the machine configuration, imbalance in the dataset will be present because of the relatively small amount of samples for the given actuator space. The distribution of I_{sat} signals can be seen in fig. 3.12. The I_{sat} distribution is clearly different for DR1 and DR2, with DR1 having a much flatter distribution. These distributions imply that if the model is constrained to sample from DR2 via the run set flag, then the model is expected to predict a lower I_{sat} value in general. When predicting from the model in general, performance will likely be worse for I_{sat} values $\gtrsim 11 \text{ mA/mm}^2$.

The distribution of the selected machine settings for all the dataruns is enumerated in table 3.4. Despite the randomization of the settings of 44 dataruns, the distribution is often uneven. This unevenness is exacerbated in the test set because that is a selection of 6 out of 67 dataruns. The remaining 23 non-random dataruns also contribute to the imbalance. For example, a source field of 1 kG and discharge voltage of 112 show up disproportionately in the dataset because data were

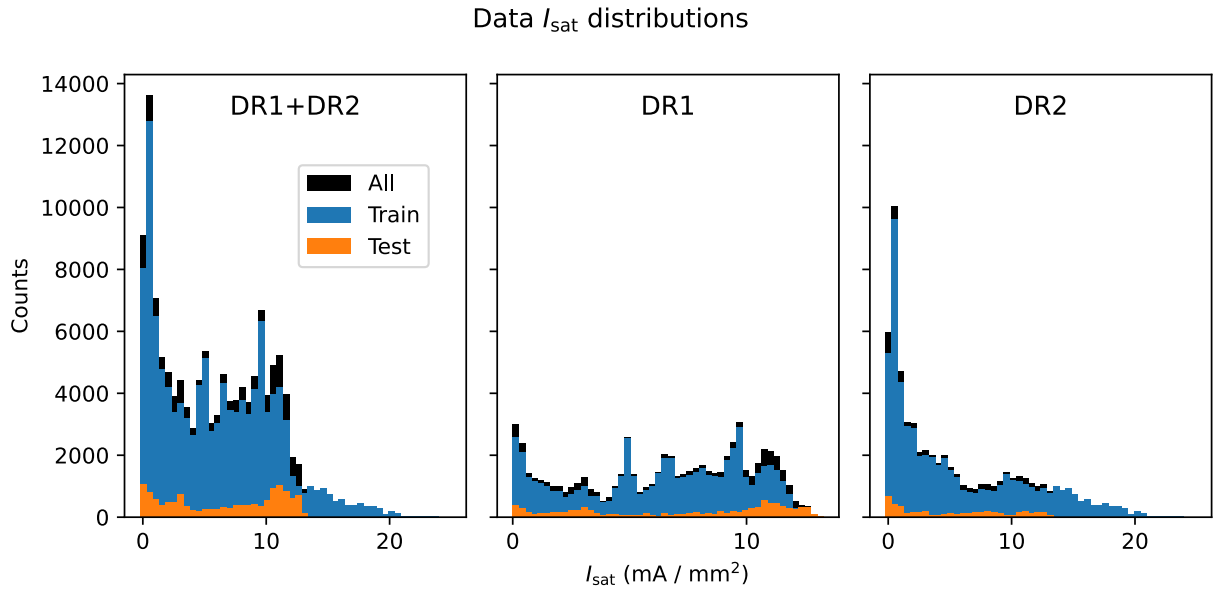


Figure 3.12: Distribution of I_{sat} signals. DR1 appears to have a more uniform distribution than DR2 does. Combining the two datasets results in many I_{sat} examples near 0 mA/mm² and a sharp decrease in number of examples above 10 mA/mm². From these histograms we expect or model to be biased towards fitting lower I_{sat} values better, and to perform badly in cases with very high I_{sat} values.

Table 3.4: Data breakdown by class and dataset (percent)

B source (G)				B mirror (G)				B midplane (G)			
	Train	Test	All		Train	Test	All		Train	Test	All
500	4.77	0	4.29	250	4.30	8.41	4.72	250	8.25	21.01	9.55
750	3.34	12.61	4.29	500	30.49	8.41	28.23	500	43.80	8.41	40.19
1000	43.13	78.99	46.78	750	6.68	16.81	7.72	750	6.62	52.19	11.27
1250	12.59	0	11.30	1000	28.85	57.97	31.82	1000	26.36	5.78	24.26
1500	19.23	0	17.27	1250	3.34	4.20	3.43	1250	9.24	0	8.30
1750	1.91	0	1.71	1500	26.34	4.20	24.08	1500	5.73	12.61	6.43
2000	15.03	8.41	14.35								

Gas puff voltage (V)				Discharge voltage (V)				Axial probe position (cm)				
	70	12.11	16.81	70	12.22	8.41	11.83	639	12.48	8.41	12.06	
	75	6.68	0	6.00	80	5.25	0	4.72	828	17.07	36.28	19.03
	80	11.46	8.41	11.15	90	2.86	8.41	3.43	859	12.48	8.41	12.06
	82	41.49	57.97	43.17	100	3.34	8.41	3.86	895	33.01	30.10	32.71
	85	14.13	0	12.69	110	8.77	0	7.87	1017	12.48	8.41	12.06
	90	14.13	16.81	14.40	112	20.62	0	18.52	1145	12.48	8.41	12.06
					120	3.82	8.41	4.29				
					130	0.95	0	0.86				
					140	2.86	8.41	3.43				
					150	39.30	57.97	41.20				

Gas puff duration (ms)				Vertical probe position (cm)			
	38	94.27	91.59	38	≈ 0	36.26	46.08
	< 38	5.73	8.41	6.00	≠ 0	63.74	53.92

collected at those settings while other equipment was being adjusted or calibrated.

Another source of imbalance is the vertical location of the probe: overnight dataruns are often planar so that machine time can be effectively used, so there are fewer planar dataruns but with many more shots, leading to more shots having a nonzero y-coordinate. This imbalance could have been avoided if the LAPD had programmable machine settings; this capability may be developed in the future.

3.12 Data and training pipeline validation

Multiple models were trained with varying depths and widths to verify that training loss decreases with increased model capacity. Doubling the layer width from 512 to 1024 moderately decreases the training loss; doubling the depth of the network from 4 to 8 layers has a larger impact. Increasing the width further to 2048 and depth to 12 layers has a dramatic impact on training loss, so this model and dataset are behaving nominally.

TODO: Discuss loss function, verifying no data leakage, and overfitting

3.13 Effect of I_{sat} calibration

The Langmuir probes did not seem to be behaving correctly when the optimization validation data were taken. The probes showed an *increasing* I_{sat} profile when moving further from the cathode in the lowest gas puff condition, which is in direct disagreement with previous measurements and intuition. An example of this discrepancy can be seen in fig. 3.10, where a run from the original testing set (specifically DR2 run 10) is duplicated. The probes for the validation run can be either corrected for by assuming the 5 ms gas puff run has a flat axial profile, or normalizing the probes to the DR2 run 10 axial profile. Calibrating the probes using the DR2 run 10 reference was the best way to go because it corrects for both probe discrepancies as well as changes in the condition (or emissivity) of the main cathode.

CHAPTER 4

Reconstructing missing diagnostics using energy-based models

The goal here is to show that diagnostics can be reconstructed from other diagnostics and machine state information (MSI) using energy-based models (EBMs). This is the first time that EBMs have been used and possibly the first time diagnostics reconstruction has been attempted using neural networks in a magnetized plasma context. The bulk of this work was performed in 2021 and 2022.

4.1 Brief introduction to energy-based models (EBMs)

4.2 Building a 15 million shot dataset

The LAPD has a set of permanent diagnostics and machine state information (MSI) that is produced but was not recorded for every shot. I built out a diagnostics pipeline that would record the following for every single shot, continuously:

1. Discharge current (time series)
2. Discharge voltage (time series)
3. 56 GHz interferometer (time series)
4. Five axially spaced photodiodes, one having a He-II filter (time series)
5. RGA and total gas pressures (single point for each mass)
6. Magnetic field profile

These data were recorded so that the shots could be synchronized with the data acquisition system used for probe measurements. A plot of a couple of shots can be seen in fig. ??.

These diagnostics and MSI have some particular characteristics. The discharge current may not be accurate based on how the value is measured. The interferometer skips when the plasma density gets too high and the signal cannot be recovered. However, the interferometer signal is still included because these fringe skips (and timing thereof) contain information about the plasma density evolution, though the numerical value may be difficult to acquire. The diodes are not absolutely calibrated, have a nonlinear response, and are not restricted to the visible spectrum. The RGA takes a minute or two to sweep, so partial pressures are not necessarily exact for the particular shot it is recorded. The magnetic field profile is calculated, not measured, so some field measurements may be incorrect if the state of a magnet power supply is recorded incorrectly, or if the source field currents were not manually updated. Despite all these issues, we proceed.

TODO: Plot of example data

This system recorded shots continuously, capturing a wide variety of LAPD machine conditions and experiments. Some particular challenges with this dataset was that other important information was not recorded in an orderly way. The north LaB6 source current and voltage time traces were not recorded even though the north source parameters could have a significant impact on the behavior of the plasma. The locations of large antennas or obstructions were also not recorded conveniently: retrieving this information would require manually opening and reading many experimental datarun files, but that only corresponds to probe data. In general this information was not recorded between dataruns.

In addition, the data may be highly biased towards a particular set of cases. The LAPD was often left as-is without changing parameters for considerable lengths of time, either between dataruns or campaigns, or in general for a particular experiment week. Thus, the data collected may not contain sufficient diversity to learn trends well, particularly with important machine state information not recorded.

The general cathode (and thus plasma condition) was also left unquantified. Variation emissivity across the cathode could lead to considerable changes across the plasma column, and the discharge characteristics could drift over time. This unquantified drift in plasma conditions further makes this dataset a difficult training target, given that the same machine configuration could lead to multiple types of plasma.

TODO: show plot of long-term trends of the discharge current and density changing.

4.3 Training the model

4.4 Unconditional sampling

4.5 Reconstructing missing diagnostics via conditional sampling

4.6 Inferring trends and outlook

CHAPTER 5

Conclusions

5.1 Future Directions

APPENDIX A

0D mirror optimization

1. **problem:** Main things that need to be done: find references and double check the equations
2. **problem:** Power to central cell isn't accounted for in plug temperature caluations fudge factor is used

1. **TODO:** Check that DT alpha orbit is contained
2. **TODO:** Add HHFW heating to increase Einj above Ebeam
3. **TODO:** Add neutron dpa
4. **TODO:** Implement assumption calculations for FLR effects and the paraxial approximation
5. **TODO:** Add FLR stabilization estimate (Eq 38 in "Magneto-hydrodynamically stable[...]", Ryutov 2011)
6. **TODO:** Add neutral beam shine through as a condition for plasma density
7. **TODO:** Compare to baseline in section 7 of Egedal et al 2022 [?]
8. **TODO:** Implement beta-enhanced mirror ratio limits from diamagnetic-bubble paper. Beta-enhanced mirror ratio flag?
9. **TODO:** Add "tail wagging" stabilization power cost
10. **TODO:** Calculate stability thresholds and growth rates

A.1 List of assumptions / conditions

There are many issues and assumptions with this analysis (in no particular order):

1. Powers and particles are not strictly balanced in tandem mirrors
2. Thermal barriers are ignored which may be very important for a practical reactor
3. A fudge factor is used for electron temperatures when plug electrons are heating the central cell
4. Macrostability is not considered
5. Microstability is not considered
6. Plug confinement time is not self-consistent with plug temperatures
7. Effects of field ripple are not calculated
8. T-T and T-He3 reaction rates are not considered
9. Radial transport is assumed to be only classical
10. Cat-DD assumes instant burnup of products which is unreasonable, particularly at the high ion energies needed in mirror reactors
11. Impurities are assumed to be zero
12. Heating and magnet costs are not justified
13. All fusion power exits the plasma immediately (charged particles are collected by the direct-energy converter, neutrons absorbed by the blanket)
14. When using the temperature model from Egedal 2022 [?], we assume that the auxiliary power is much less than the beam power ($P_{aux}/P_{NBI} \ll 1$) or else the model may be inaccurate. Auxiliary power (say, to compensate for classical diffusion losses or additional ECH) can be included in this model but it would require iterative solving.

15. Burnup fraction is sufficiently small that fusion reactions are not a significant loss of fuel (ironically).
16. The DECs collect all ion losses at a fixed efficiency

A.2 User specified parameters

A.2.1 Simple mirror endplug

1. Mirror field, plug (T): $B_{p,m}$
2. Plug (i.e., midplane) cell field (T): B_p
3. Magnet bore/throat radius (m): r_b
4. Plug length (m): L_p
5. Neutral beam energy (keV): E_{inj} or E_b
6. Beta limit (critical stability): β_{limit} (set to 0.8 [?])
7. Effective species mass (amu): μ
8. Effective atomic number (account for He and other impurities): Z_{eff}

The β_{limit} (discussed in Kotelnikov 2021 [?]) assumes a stationary plasma (no rotation, no flow out the ends), ignores finite-Larmor-radius (FLR) effects (which stabilize $m > a^2/L\rho_i$ modes), and uses the paraxial approximation ($L_m \gg a$). It also assumes $\beta \ll 1$ but this paper shows that these results match up with GDT experiments. The β_{limit} depends on the radial pressure profile falloff; the faster the falloff, the lower the β_{limit} . L is the length from midplane to throat, and L_m is the length of the mirror (highest field to lowest, I think). Profile calculations will not be included in a 0D optimization. The relevant assumptions for FLR effects and the paraxial approximation should be calculated and shown in the output to make sure they are not dramatically violated.

A.2.2 Tandem mirror

Central cell parameters defined below. Simple mirror endplugs are used on either end.

1. Central cell field (T): B_{cc}
2. Central cell to plug density ratio: n_{cc}/n_p
3. Central cell ion to plug electron temperature ratio: $T_{cc,i}/T_{p,e}$ (assumes Maxwellian)
4. Central cell to plug electron temperature ratio: $T_{cc,e}/T_{p,e}$
5. Central cell length (m): L_{cc}
6. Electron temperature fudge factor: $T_{ep, \text{fudge}}$ if electron are heating the central cell. Default value is 0.5

A.2.3 Engineering parameters

1. Vessel wall radius (with respect to plasma radius): $a_{\text{wall}} = a_{\text{wall, ratio}} \cdot a_{\text{plasma}}$
2. Blanket thickness: d_{blanket}
3. Vacuum vessel thickness: d_{vv}
4. Direct Converter Efficiency (used in the mirror exhaust): η_{DEC}
5. Thermal to electric conversion efficiency: η_{TE}
6. ECH heating efficiency: η_{ECH}
7. NBI heating efficiency: η_{NBI}
8. RF heating efficiency: η_{RF}

Optimizing the blanket and vacuum vessel thickness would probably require some neutronics calculations which would probably depend on the fuel mix, so we're just going to leave those constant in our optimization.

A.3 Fusion

DT fusion helium energy (keV): $E_\alpha = 3500$

A.3.1 Reactivity

DD and DT fusion cross-section parameterizations can be found in Bosch 1992. [?]. What we care most about is the fusion reaction rate per unit volume (eq. 10 in the paper):

$$\frac{dR}{dV} = \frac{n_i n_j}{1 + \delta_{ij}} \langle \sigma v \rangle \quad (\text{A.1})$$

This parameterization accepts ion temperature in keV and gives reactivity in cm^3/s :

$$\langle \sigma v \rangle = C1 \cdot \theta \sqrt{\xi / (m_r c^2 T^3)} e^{-3\xi} \quad (\text{A.2})$$

$$\theta = T / \left[1 - \frac{T(C2 + T(C4 + TC6))}{1 + T(C3 + T(C5 + TC7))} \right] \quad (\text{A.3})$$

$$\xi = (B_G^2 / 4\theta)^{1/3} \quad (\text{A.4})$$

$$B_G = \pi \alpha Z_1 Z_2 \sqrt{2 m_r c^2} \quad (\text{A.5})$$

where m_r is the reduced mass and α is the fine structure constant. The coefficients ($C1$, $C2$, and so on) are in the paper cited above. This parameterization is valid for T_i between 0.2 to 100 keV.

problem: We will definitely exceed this in our optimization – the extent of the deviation should be quantified. The cross section explodes for DD after roughly 500 keV Max error is 0.25% for DT and 0.35% and 0.3% for DD $\Rightarrow p$ T and DD $\Rightarrow n$ He3, respectively. phil: We will want to use the cross-section (the parameterization of which goes up to 550 keV for DT in [?]) and integrate over ion distribution. Integration over non-Maxwellian ion distributions should be doable if FBIS [?] can give the full distribution. phil: For now I'm just linearly interpolating (in log-log space)

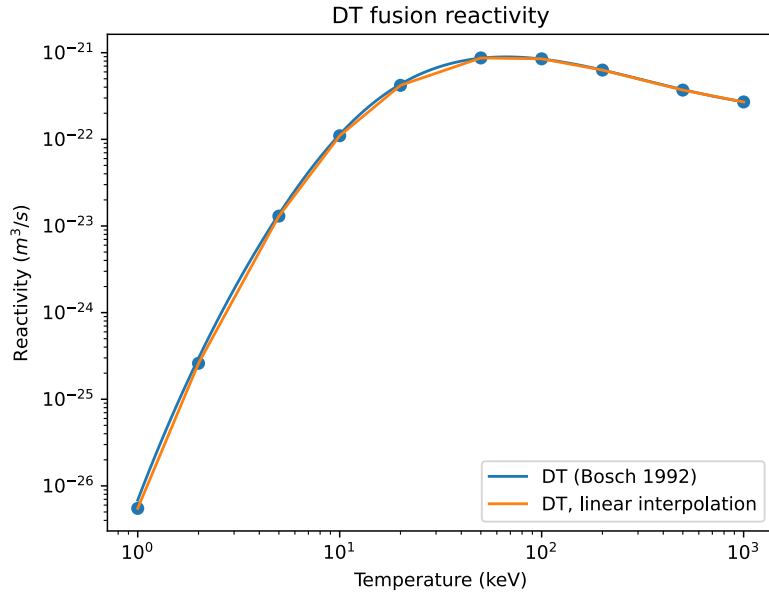


Figure A.1: DT reactivities

between the points provided in the NRL. Comparison plots of the different methods for DD and DT can be seen in figures A.1 and A.2.

A.3.2 Fusion power

DT fusion reaction rate (#/s):

$$R_{x,DT} = V n_D n_T \langle \sigma v \rangle_{DT} \quad (\text{A.6})$$

If $n_D = n_T = n/2$, then this becomes $V \frac{n^2}{4} \langle \sigma v \rangle_{DT}$

DD fusion reaction rate (#/s):

$$R_{x,DD} = V \frac{n_{\text{plug, D}}^2}{2} \langle \sigma v \rangle_{DD} \quad (\text{A.7})$$

The $\frac{1}{2}$ factor is to avoid double counting DD reactions.

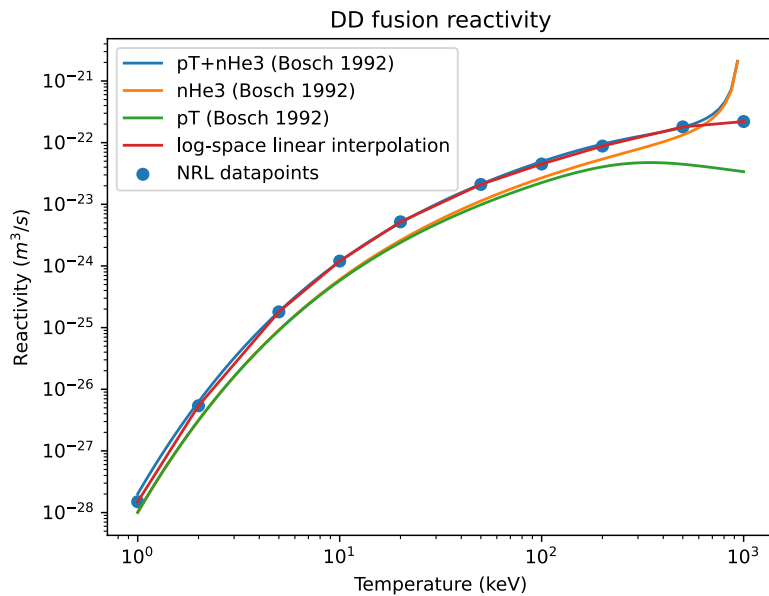


Figure A.2: DD reactivities

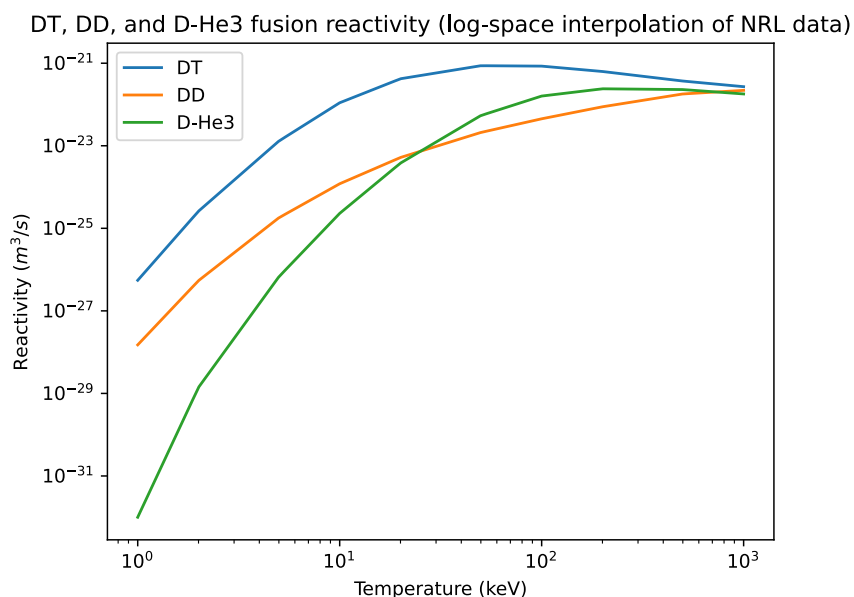


Figure A.3: DT, DD, and D-He3 reactivity comparison

Fusion power (MW):

$$P_{DT,n} = 14.1 |e| R_{x,DT} \quad (A.8)$$

$$P_{DT,+} = 3.5 |e| R_{x,DT} \quad (A.9)$$

$$P_{DD,n} = 2.45 |e| R_{x,DD} \cdot \frac{1}{2} \quad (A.10)$$

$$P_{DD,+} = (4.02 + 0.82) |e| R_{x,DD} \cdot \frac{1}{2} \quad (A.11)$$

$$(A.12)$$

It's useful to split the power into charged and neutrons because energy is extract from them in different ways. Neutrons provide thermal power, charged particles heat the plasma and/or are directly captured by the DECs. The $\frac{1}{2}$ coefficient on the DD reactions assumes a 50-50 split on the DD branching ratio which actually varies with energy and may be significant above around 100 keV. If we assume the tritium produced from a DD reaction is burned instantly, then the additional power produced ("catalyzed DD") is:

$$P_{cat\ DD,n} = 14.1 |e| R_{x,DD} \cdot \frac{1}{2} \quad (A.13)$$

$$P_{cat\ DD,+} = (3.5 + 18.3) |e| R_{x,DD} \cdot \frac{1}{2} \quad (A.14)$$

$$(A.15)$$

We assume the tritium is burned instantly because the DT reaction rate is much higher than DD and D-He3 fusion up to around 200 keV, after which it's only slightly higher up to around 1 MeV. A more accurate estimate of fusion power would require estimates of D-He3, TT, and T-He reaction rates and density evolution of each species. A plot of reactivities can be found in Fig. A.3. phil:
I do not know how to do this steady-state calculation in a simple 0d way – perhaps this sort of calculation is left for a more detailed reactor model.

A.4 General formulae

Electron cyclotron frequency (GHz):

$$f_{\text{ECH}} = \frac{eB}{2\pi m_e c} = 28B \quad (\text{A.16})$$

Ion cyclotron frequency (MHz):

$$f_{ci} = \frac{ZeB}{2\pi m_i c} \quad (\text{A.17})$$

$$f_{ci,D} = 7.63B \quad (\text{A.18})$$

$$f_{ci,T} = 5.09B \quad (\text{A.19})$$

Here, Z is the charge state of the ion.

Electron plasma frequency (Hz):

$$f_{pe} = \frac{1}{2\pi} \sqrt{\frac{4\pi n_e e^2}{m_e}} = 8.98 \cdot 10^3 \sqrt{n_{\text{plug}}} \quad (\text{A.20})$$

Ion plasma frequency (Hz):

$$f_{pi} = \frac{1}{2\pi} \sqrt{\frac{4\pi n_i Z^2 e^2}{\mu m_p}} \quad (\text{A.21})$$

$$f_{pi,D} = 2100 \sqrt{\frac{n_{\text{plug}}}{2}} \quad (\text{A.22})$$

$$f_{pi,T} = 2100 \sqrt{\frac{n_{\text{plug}}}{3}} \quad (\text{A.23})$$

Here, μ is the mass of the ion in proton mass units (e.g. $\mu_{\text{Deuterium}} = 2$ and $\mu_{\text{Tritium}} = 3$).

Lorentz factor (γ):

$$\gamma = \sqrt{1 + \frac{T_e}{m_e c^2}} = \sqrt{1 + \frac{T_e}{511 \text{keV}}} \quad (\text{A.24})$$

Ion thermal velocity:

$$v_{Ti} = 97900 \sqrt{\frac{10^3 E_{\text{ion}}}{\mu}} \quad (\text{A.25})$$

Ion gyroradius: problem: Cary's spreadsheet uses the temperature to calculate this but calls it " E_{ion} ". I think temperature should be used to accurately account for the energy in vperp

$$\rho_i = \frac{mv_\perp}{qB} = 3.22 \cdot 10^{-3} \frac{\sqrt{\mu E_{ion}}}{B_p} \quad (\text{A.26})$$

Whistler wavelength:

$$\lambda_{\text{whistler}} = \sqrt{\frac{2\pi\Omega_e c^2}{\Pi_e^2 f}} \quad (\text{A.27})$$

$$\lambda_{\text{whistler}} = \sqrt{\frac{90 f_{\text{ECH}}}{f_{pe}^2 f_{D,2\text{nd Harmonic}}}} \quad (\text{A.28})$$

The 2nd formula is what appears on the spreadsheet and is used to estimate the size of the RF wave used for HFW as compared to the size of the plasma. It takes into account the various constants and units used in the spreadsheet.

Collision rates (from NRL):

$$v_e = 2.91 \cdot 10^{-6} \frac{n_e \ln \Lambda}{T_e^{3/2}} \quad (\text{A.29})$$

$$v_i = 4.80 \cdot 10^{-8} \frac{Z_{\text{eff}}^4 n_i \ln \Lambda}{\mu^{1/2} T_i^{3/2}} \quad (\text{A.30})$$

These can be rearranged to give the following collision times (s): problem: this seems to assume $\log \Lambda = 20$ (should be doubled check but doesn't probably make much of a difference – comparing to eq 4.8 in [?]). problem: Depends on Zeff which isn't accounted for during optimization/power balance. phil: Technically we should use $T = \frac{2}{3}E_{ion}$ for the central cell since the distribution is likely approximately Maxwellian, but it only changes τ_{ii} by a factor of 1.8.

$$\tau_{ee} = 10^{-4} \frac{T_e^{3/2}}{n_{20} \lambda_{ee}} \quad (\text{A.31})$$

$$\tau_{ii} = 1.25 \cdot 10^{-4} \frac{\mu^{1/2} E_{ion}^{3/2}}{n_{20} Z_{\text{eff}}^4} \quad (\text{A.32})$$

Slowing down times [?] phil: I assume Z is Zeff? Need to double check. I put it as Zeff in the ipynb :

$$\tau_{i,\text{slow}} = 0.1 \frac{\mu T_e^{3/2}}{n_{20} Z^2 \lambda_{ei}} \quad (\text{A.33})$$

$$\tau_{i,\text{fast}} = \left(\left(\tau_{ii} 0.4 \log \frac{R_m}{\sqrt{1-\beta}} \right)^{-1} + \frac{1}{\tau_{\text{slow}}} \right)^{-1} \quad (\text{A.34})$$

Here, we can write $Z = 2$ for alpha particles. The 2nd equation comes from substituting the expression for T_e in a purely NBI heated case seen above.

Coulomb logarithms:

$$\lambda_{ee} = 23.5 - 0.5 \ln n_e + 1.25 \ln T_e - \left(10^{-5} + \frac{(\ln T_e - 2)^2}{16} \right)^{1/2} \quad (\text{A.35})$$

$$\lambda_{ei} = 24 - 0.5 \ln n_e + \ln T_e \quad (\text{A.36})$$

$$\lambda_{ii,\text{Cary}} = 31 - 0.5 \ln n_e + \ln T_e \quad (\text{A.37})$$

$$\lambda_{ii,\text{NRL}} = 23 - 0.5 \ln n_e + 1.5 \ln T_i \quad (\text{A.38})$$

The formula for λ_{ee} is from NRL. The formula for λ_{ei} is from NRL. However, the plasma does not fit into any of the 3 limiting cases described in the formulary. We have picked the formula based on the condition that is violated the least severely. There are 2 formulas for λ_{ii} . They do not have a large disagreement in the ranges of T_e and T_i of interest.

A.5 Radial particle transport

As of the time of writing, diffusive radial transport in mirror reactors appears to be an open question. The goal here is to provide reasonable estimates of radial particle loss and how each scale, not necessarily going for high-accuracy predictions (though being close would be nice!)

A.5.1 Classical diffusion

Assuming Fick's law and a linear density gradient from $3n$ to 0 (from Chen 5.8):

$$\tau_{\text{classical}} = \frac{nV}{A \cdot \Gamma} = \frac{na}{-2D_{\perp} \nabla n} \quad (\text{A.39})$$

where D_{\perp} is defined as

$$D_{\perp} = \eta_{\perp} n \sum T / B^2 \quad (\text{A.40})$$

and the parallel and perpendicular conductivities are

$$\eta_{||} = 5.2 \cdot 10^{-5} \frac{Z \ln \Lambda}{T^{3/2}} \quad (\text{A.41})$$

$$\eta_{\perp} = 2 \cdot \eta_{||} \quad (\text{A.42})$$

Combining all of this together gives

$$\tau_{\text{classical}} = \frac{a^2 B^2 T_e^{3/2}}{3.12 \cdot 10^{-4} \cdot n Z \sqrt{\mu} \ln \Lambda \sum T} \quad (\text{A.43})$$

A.5.2 Bohm diffusion

phil: I don't like how pessimistic the estimates are for this are. Reasonable values gets you 500 μs confinement times for Bohm diffusion. Bohm diffusivity:

$$D_{\text{Bohm}} = \frac{1}{16} \cdot \frac{T_{i,cc} \cdot 10^3}{B_{cc}} \quad (\text{A.44})$$

Normalized gyroradius (assuming deuterium):

$$r_{\text{Larmor}} = \frac{\sqrt{2mE_{\perp}}}{2eB_{cc}} = \frac{0.00791 \sqrt{T_{i,cc}}}{B_{cc}} \text{ cm} \quad (\text{A.45})$$

$$\rho^* = \frac{r_{\text{Larmor}}}{a_{cc}} \quad (\text{A.46})$$

Again, using Fick's law and assuming a linear density gradient from $3n$ to 0 (so that total particle number remains $n \cdot V$), cross-field particle flux is:

$$\Gamma = -D_{\text{Bohm}} \cdot \nabla n_e \quad (\text{A.47})$$

$$= \frac{1}{16} \cdot \frac{T_{i,cc} \cdot 10^3}{B_{cc}} \cdot 3n_i \quad (\text{A.48})$$

which implies a characteristic confinement time of

$$\tau_{\text{Bohm}} = N_{\text{tot}} \left/ \frac{dN}{dt} \right. = n_i \cdot V / (\Gamma * A) \quad (\text{A.49})$$

$$= n_i \cdot \pi a^2 L \left/ \left(\frac{1}{16} \cdot \frac{T_{i,cc} \cdot 10^3}{B_{cc}} \cdot 3n_i \cdot 2\pi a_{cc} L \right) \right. \quad (\text{A.50})$$

$$= \frac{8aB_{cc}}{3T_{i,cc}10^3} \quad (\text{A.51})$$

A.5.3 Gyro-Bohm diffusion

The gyro-Bohm scaling assumes cross-field transport is dominated by small ion-gyroscale turbulence. Though commonly used for tokamak scaling laws, we should be able to get some rough estimates for mirrors. Right now it can be estimated by just diving the Bohm confinement time by the normalized gyroradius ρ^* . The gyro-Bohm estimate is then:

$$\tau_{\text{gyro-Bohm}} = \frac{8aB_{cc}}{3T_{i,cc}10^3} \cdot \frac{1}{\rho^*} \quad (\text{A.52})$$

The $\frac{1}{\rho^*}$ factor can boost the confinement time estimate by a factor of 50-100. phil: But the confinement times still seems a little low.

A.5.4 ETG-driven transport

Cary's spreadsheet says phil: (I'm having trouble finding a derivation or hand-wavy justification)

:

$$\chi_{\text{ETG}} = 0.1 \frac{T_{e,cc}^{3/2}}{B_{cc}} \quad (\text{A.53})$$

$$\tau_{\text{ETG}} = \frac{a_{cc}^2}{\chi_{\text{ETG}}} \quad (\text{A.54})$$

A.6 Mirror-specific derived quantities

A.6.1 Temperatures and confinement time in a beam-heated mirror from Egedal et al 2022 [?]

Electron and ion temperature (keV) via pure beam heating [?]: we must solve a system of equations which considers the power balance of the machine. The ion temperature, given by eq. 22 in [?] is:

$$\frac{3}{2} \frac{T_i}{E_{beam}} = \frac{\exp(-\alpha) - \alpha \Gamma(0, \alpha)}{\Gamma(0, \alpha)} \quad (\text{A.55})$$

Note that eq. 22 in [?] is missing a factor of α in the numerator in front of the Γ function. The electron temperature can be found in terms of T_i and α by rearranging the definition of α (eq 21):

$$\frac{T_e}{E_{beam}} = \left(\frac{T_i}{E_{beam}} \frac{2}{3} \frac{\alpha^2 \ln R_m^2}{(22.4)^2} \right)^{1/3} \quad (\text{A.56})$$

These can be solved for with the help of a power (really energy-per-particle) balance equation (eq. 24 in [?]):

$$E_{beam} + p_{aux} = T_i + 6T_e \quad (\text{A.57})$$

where p_{aux} is the combined sources and losses, such as alpha-particle heating, plasma heat losses, RF heating, radial transport, and so on. By balancing the power lost with auxiliary heating power we can keep $p_{aux} = 0$ to avoid iteratively solving this equation. Each ion loses $T_i + e\Phi \approx T_i + 5T_e$ units of energy and each electron loses $\approx T_e$ units because only hotter electrons can surmount the ambipolar potential. p_{aux} isn't so much a power as it is the energy gained/lost per particle – an actual power would require evaluation of the confinement time (eq 29 in [?]):

$$\tau_p = \tau_{T_i}^{90} \frac{1}{\alpha_1 \lambda_1} \frac{\mathcal{H}}{T_i/E_{beam}} \int_0^1 M_1(\xi) d\xi \quad (\text{A.58})$$

where $\tau_{T_i}^{90}$ is the "scattering reactivity", α_1 , λ_1 , and M_1 are the normalization value, eigenvalue, and eigenfunction of the Lorentz scattering operator (eq 4 in [?]). phil: I can't be bothered to write a differentiable solver for the confinement time right now so we're just going to use the

values of $\tau_{\text{Fowler-Baldwin}}$ for the first rough optimizations (which Cary says will give pessimistic estimates (actually, not sure)). By particle conservation and because NBI will be the dominant fueling mechanism, confinement time relates to density and beam current by:

$$\tau_p = eVn_b/I_{\text{NBI}} \quad (\text{A.59})$$

For ion temperature, Cary's spreadsheet says:

$$T_i = \frac{2}{3}E_{\text{inj}} \quad (\text{A.60})$$

This emerges from the relation that $E = \frac{1}{2}k_B T$ for every degree of freedom. For single particles, we assume 3 degrees of freedom to get $E = \frac{3}{2}T$ where T is expressed in eV. problem: If referencing Egedal et al 2022 [?], this is only true if the electrons are very hot, i.e., $T_e(\log R_M)^{2/3}/E_{\text{inj}} \approx 1$. However, it is also shown in the paper that $T_i/E_{\text{inj}} \sim 0.6$. Assuming 2/3 is more conservative because a higher temperature means a lower reactivity and thus lower total fusion power at temperatures above 70-ish keV.

For electron temperature, Cary's spreadsheet says:

$$T_e = 0.089E_b \log_{10}(R_p)^{0.4} \quad (\text{A.61})$$

$$= 0.089E_b \log_{10}\left(\frac{R_p}{1-\beta}\right)^{0.4} \quad (\text{A.62})$$

which seems to give a roughly 2x higher electron temperature than the reduced model in Egedal 2022 [?], which means that our estimate will be more optimistic. Kunal: Cary said this comes from working through the energy balance of a beam heated mirror device. Apparently it is in their new paper. I will go over this and figure it out. The $1 - \beta$ term is from the finite beta corrections to the mirror ratio.

Particle confinement time (Convention: $R_p = R_m$) found in Baldwin's end-loss paper [?] equations 4.14 and 4.13. The same equation can be applied to tandem mirrors with thermal barriers and plug cells [?]. According to Cary, this number will give pessimistic estimates. Equation 4.14 [?] states:

$$n\tau_{\text{Fowler/Baldwin}} = \kappa \times 10^{10} E_b^{3/2} \log R_{\text{eff}} / \log 10 \quad (\text{A.63})$$

where $[n]$ is cm^{-3} and $[E_b]$ is keV, and

$$R_{\text{eff}} = R_m / (1 + (q\phi / mE_i)) \quad (\text{A.64})$$

For 90ž NBI, κ falls between 2.4 and 2.8 according to Fokker-Planck calculations [?]; it would be ~ 1.7 if the ion distribution did not have a loss-cone hole because the average energy is higher.

problem: Angled injection can impact this significantly (but ignoring for reduced model optimization) **phil:** I don't understand what this $(q\phi / mE_i)$ term is. This is a purely classical number – the main loss of ion energy is to electron drag, followed by ion-ion collisions / scattering into the loss cone (ions lost and accelerated by the ambipolar potential can be recaptured by direct energy conversion, but that is not accounted for here). Electrons are chilled by neutral beam injection and lost out the ends of the mirror if their energy exceeds the ambipolar potential. Converting to $[n]$ in m^{-3} :

$$\tau_{\text{Fowler/Baldwin}} = 2.8 \cdot 10^{16} \frac{E_b^{3/2}}{n_e} \log R_m / \log 10 \quad (\text{A.65})$$

We may also need finite- β corrections to the mirror ratio.

A.6.2 Confinement time given by classical transport

Classical confinement time estimates assumes that transport is dominated by diffusion of gyrocenters via Coulomb collisions (from Chen section 5.8[?]). The diffusivity is:

$$D_{\text{classical}} = \eta_{\perp} n \sum T / B^2 \quad (\text{A.66})$$

where the perpindicular conductivity (for hydrogen) η_{\perp} is (temperatures in eV):

$$\eta_{\perp} = 2 \cdot \eta_{\parallel}, \quad (\text{A.67})$$

$$\eta_{\parallel} = 5.2 \cdot 10^{-5} \frac{Z \ln \Lambda_{ei}}{T_e^{3/2}} \sqrt{\mu} \quad (\text{A.68})$$

The confinement time is then (summing over species):

$$\tau_{\text{classical}} = \frac{nV}{A \cdot \Gamma} \quad (\text{A.69})$$

$$= \frac{na}{-2D_{\text{perp}} \nabla n} \quad (\text{A.70})$$

$$\tau_{\text{classical}} = \frac{aB^2}{-2\eta_{\perp} \nabla n \sum T} \quad (\text{A.71})$$

Again assuming a linear radial density profile with a peak of $3n_i$ to keep the total particle number $n_i \cdot V$:

$$\tau_{\text{classical}} = \frac{a^2 B^2 T_e^{\frac{3}{2}}}{3.12 \cdot 10^{-4} \cdot n Z \sqrt{\mu} \ln \Lambda \sum T} \quad (\text{A.72})$$

The aggregate confinement time is then:

$$\tau_{\text{tot}} = \frac{1}{\frac{1}{\tau_{\text{classical}}} + \frac{1}{\tau_{\text{Fowler/Bladwin}}} \quad (\text{A.73})}$$

A.6.3 End Cells/Plugs

Mirror ratio:

$$R_{\text{plug}} = \frac{B_{p,m}}{B_p} \quad (\text{A.74})$$

Radius at the midplane (mapped from bore radius):

$$a_{\text{plug}} = r_b \sqrt{\frac{B_{p,m}}{B_p}} \quad (\text{A.75})$$

Volume:

$$V_p = L_p \pi a_p^2 \quad (\text{A.76})$$

Total particle number:

$$N_{\text{tot}} = V_p n_{\text{plug}} \quad (\text{A.77})$$

Particles lost per second:

$$\frac{dN}{dt} = \frac{N_{\text{tot}}}{\tau_{\text{Fowler/Baldwin}}} \quad (\text{A.78})$$

Number of gyroradii in the plasma radius:

$$N_{\text{gyro}} = \frac{a_p}{\rho_i} \quad (\text{A.79})$$

Density (m^{-3}) at the β limit:

$$n_{\text{plug}} = B_p^2 \frac{\beta_{\text{limit}}}{2\mu_0|e|(T_{\text{ion}} + T_e)} \quad (\text{A.80})$$

Here, T_{ion} and T_e are expressed in eV. This can be found in Wesson page 115. Rolling all the constants together and with T_i and T_e in keV:

$$n_{20} = n_{\text{plug}}/10^{20} = B_p^2 \frac{\beta_{\text{limit}}}{0.04(T_{\text{ion}} + T_e)} \quad (\text{A.81})$$

NBI Current (A): phil: This should already account for dN/dt caused by fusion reactions if we assume that alphas have a similar confinement time? This is the current that the lost particles are reinjected after filtering out ash. Fusion reactions decrease the number of ions so N will actually be lower at a factor of around 1 – burnup fraction.

$$I_{\text{NBI}} = |e| \frac{dN}{dt} \quad (\text{A.82})$$

The neutral beam current is enough to replace the particles lost by the end plugs. In reality, this number will be larger since the beam neutrals are ionized via charge exchange as well as ion/electron impact.

Electron heating by fast ions (MW):

$$P_{\text{e heating by fast ions}} = 10^{-3} \frac{I_{\text{NBI}} E_b}{\tau_{\text{slow}}} \quad (\text{A.83})$$

Synchrotron radiation power loss (MW) [?]:

$$P_{\text{synch}} = 6 \cdot 10^{-3} V_p n_{20} T_e \gamma^2 B_p^2 \quad (\text{A.84})$$

Bremsstrahlung radiation power loss (MW) [?]:

$$P_{\text{brem}} = 5.35 \cdot 10^{-3} n_{20}^2 Z_{\text{eff}} \sqrt{T_e} V_p \quad (\text{A.85})$$

Power loss from escaping electrons (MW):

$$P_{e,\text{endloss}} = 10^{-3} (I_{\text{NBI}} + I_{\text{cooling}}) \cdot 7T_e \quad (\text{A.86})$$

I_{cooling} is non-zero when there is current in the expander/divertor. The $7T_e$ is because only electrons with an energy greater than the ambipolar potential can escape.

Power loss from escaping fast ions (MW):

$$P_{i,\text{endloss}} = 10^{-3} I_{\text{NBI}} (E_b - T_e) \quad (\text{A.87})$$

Injected NBI Power (MW):

$$P_{\text{NBI}} = 10^{-3} I_{\text{NBI}} E_b \quad (\text{A.88})$$

Injected ECH Power (MW): problem: Roll this into power balance equation (eq 24 in [?]).

But this will take considerable effort. phil: Electron endloss power should already be accounted for in the reduced model, but heating from fast ions is not. Synchotron + fast ion heating + Bremsstrahlung must be included in ECH to have a consistent T_e .

$$P_{\text{ECH}} = \frac{P_{\text{synch}}}{20} + P_{e,\text{endloss}} - (\text{Electron heating from fast ions}) \quad (\text{A.89})$$

Divide by 20 since the plasma recaptures most of the synchrotron losses are reabsorbed.

Lawson Triple Product ($10^{20}\text{keV}\cdot\text{s}/\text{m}^3$):

$$\tau_{\text{Fowler/Baldwin}} n_{20} T_i \quad (\text{A.90})$$

Neutron Flux (MW/m^2): problem: This should include DD and cat-DD neutrons.

$$\frac{14}{17.6} \frac{P_{\text{plug}}}{4\pi a_{\text{wall}}^2} \quad (\text{A.91})$$

phil: Does DD vs DT neutron flux significantly affect breeding ratios? For 400 keV ion temperatures it could lower the DT TBR requirements by like 10% or so – definitely significant when targeting TBRs of like 1.1. This info can be found on <https://www-nds.iaea.org/exfor/endf.htm>

using the targets LI-6; LI-7, reactions MT-105 and 205: N,T;N,XT, and extending the energy above 10 MeV.

phil: Burnup fraction, alpha particle density, and Zeff aren't really used in the optimization anywhere. It'd be tricky to include the effects of alpha particle density because that may change the slowing-down times which effects the power balance of the end plugs and so on. These effects would require time-evolution, which is beyond the scope of this "0D" analysis. We would expect the density and reaction rate error to be on the order of the burnup fraction, because ash can be filtered out and exhausted while the fuel is reinjected.

Burnup fraction:

$$\frac{R_{x,\text{plug,DT}}}{dN/dt} \quad (\text{A.92})$$

α particle density ($10^{20} m^{-3}$):

$$n_\alpha = \frac{I_{\text{NBI}} Q_{\text{plug}} \tau_\alpha E_b}{16 V_p E_\alpha} \quad (\text{A.93})$$

but a more intuitive way of putting it may be **phil:** (need to double check this) :

$$n_\alpha = \frac{\tau_\alpha (R_{x, \text{DT}} + \frac{1}{2} R_{x, \text{DD}})}{V} \quad (\text{A.94})$$

Z_{eff} : (from Wesson section 2.16 [?]) **phil:** We assume no impurities! :

$$Z_{\text{eff}} = \frac{\sum_j n_j Z_j^2}{\sum_j n_j Z_j} = \frac{n + 4n_\alpha}{n + 2n_\alpha} \quad (\text{A.95})$$

Q_{plug} :

$$Q_{\text{plug}} = \frac{P_{\text{plug}}}{P_{\text{injected}}} \quad (\text{A.96})$$

phil: These quantities below are for a simple mirror. These will be duplicated for a tandem system and will be unused in any optimization since simple mirrors are unlikely to make a compelling reactor.

$P_{\text{electric,in}}$:

$$P_{\text{electric,in}} = P_{\text{total}} \left(\frac{1}{\eta_{HS}} - \eta_{DC} \left(1 - \frac{T_e}{E_b} \right) \right) \quad (\text{A.97})$$

$P_{\text{electric,out}}$: phil: The 0.8 represents the heating contribution from neutrons.

$$P_{\text{electric,out}} = 0.8 \eta_{HS} P_{\text{plug}} \quad (\text{A.98})$$

Q^* : phil: The 0.2 represents the alpha particle contribution. Note that

$$Q^* = \frac{Q_{\text{plug}}}{\frac{1}{\eta_{HS}} - \eta_{DC} \left(1 - \frac{T_e}{E_b} + 0.2 Q_{\text{plug}} \right)} \quad (\text{A.99})$$

Q_{electric} :

$$Q_{\text{electric}} = Q^* \cdot 0.8 \cdot \eta_{HS} \quad (\text{A.100})$$

A.6.4 Tandem mirror central cell

Radius at the midplane:

$$a_{cc} = r_b \sqrt{\frac{B_{p,m}}{B_{cc}}} \quad (\text{A.101})$$

Central cell mirror ratio:

$$R_{cc} = \frac{B_{p,m}}{B_{cc}} \quad (\text{A.102})$$

Central cell beta:

$$\beta_{cc} = \frac{2\mu_0|e|n_{cc}(T_{cc,i} + T_{cc,e})}{B_{cc}^2} \quad (\text{A.103})$$

$\beta_{cc} \geq 1$ will lead to an infinite Pastukhov factor, so the β -enhanced mirror ratio $R_{cc,\text{eff}} = R_{cc} \left(\sqrt{1 - \beta_{cc}} \right)^{-\frac{1}{2}}$ will be limited by keeping $\beta_{cc} \leq 0.9$.

In a tandem mirror (without a thermal barrier), we assume that the central cell electrons and plug cell electrons are Maxwellian and in thermal equilibrium, and that the central cell ions are also at the same temperature (Introduction to Tandem Mirror Physics, eq 1-3 (pg 78)):

$$T_{cc,i} = T_{cc,e} = T_{\text{plug},e} \cdot T_{\text{fudge factor}} \quad (\text{A.104})$$

The plug cell electron temperature is reduced by some fudge factor because they are heating the central cell plasma. Since the electrons follow a Maxwellian distribution along field lines, they

follow the Maxwell-Boltzmann relationship, where the potential difference between the plug and central cells are given by:

$$\Phi_i = \Phi_p - \Phi_c = T_{ep} \ln \left(\frac{n_p}{n_c} \right) \quad (\text{A.105})$$

The enhancement in ion confinement time in the central cell is then given by the Pastukhov factor (Pastukhov 1974, eq. 21 [?], Kesner et al. eqs. 1-3 [KGL83]):

$$n_c \tau_i = n_c \tau_{ii} g(R) \frac{\Phi_i}{T_{ic}} \exp \left(\frac{\Phi_i}{T_{ic}} \right) \quad (\text{A.106})$$

where $g(R)$ is a weak function of the mirror ratio. We assume the $g(R)$ is:

$$g(R) = \log \left(2R_{cc} \frac{1}{\sqrt{1-\beta_{cc}}} + 1 \right) \quad (\text{A.107})$$

The ion confinement time is then:

$$\tau_E = \text{Pastukhov} \cdot \tau_{cc,ii} \quad (\text{A.108})$$

$$= \log \left(2R_{cc} \frac{1}{\sqrt{1-\beta_{cc}}} + 1 \right) \frac{T_{ep}}{T_{ic}} \ln \left(\frac{n_p}{n_{cc}} \right) \left(\frac{n_p}{n_{cc}} \right)^{T_{p,e}/T_{c,i}} \cdot \tau_{cc,ii} \quad (\text{A.109})$$

Since $T_{p,e} = T_{c,i}$, this reduces to

$$\tau_E = \log \left(2R_{cc} \frac{1}{\sqrt{1-\beta_{cc}}} + 1 \right) \ln \left(\frac{n_p}{n_{cc}} \right) \left(\frac{n_p}{n_{cc}} \right) \cdot \tau_{cc,ii} \quad (\text{A.110})$$

Thermal barriers are not considered in this analysis, which enhance the central cell confinement by elevating plug electron temperatures instead of only modifying the plug-central cell density ratio (see Post 1987 eq. 10-110[Pos87]). Thermal barriers require additional heating and ion pumpout methods. If estimates of the power requirements of thermal barriers are available, they can be easily included in this analysis and optimization process.

Power lost from the reactor by central cell particles, per meter (MW, T in keV):

$$P_{cc,loss} = 10^{-3} \pi \cdot a_{cc}^2 n_{cc} \cdot e \frac{3}{2} (T_{cc,i} + T_{cc,e}) / \tau_E \quad (\text{A.111})$$

Since this is axial power lost, it's assumed that this power (at least the ion contribution) is recovered by the DECs.

The power lost can be account for by lowering T_e by some fudge factor, or re-heating the electrons back up to the self-consistent temperature by injecting ECH:

$$P_{aux,ECH} = P_{cc,loss} \quad (\text{A.112})$$

The central cell will be fueld using cold gas puffing and is ionized and heated by electrons from the plugs. The fueling current is then:

$$I_{cc,fuel} = \frac{dN_{cc}}{dt} = \pi a_{cc}^2 L_{cc} n_{cc} / \tau_E \quad (\text{A.113})$$

Fusion Power per meter (MW/m): phil: here for legacy reasons. In the actual optimization procedure length will be one of the quantities that is optimized

$$P_{fusion} = 17.6 |e| R_x \quad (\text{A.114})$$

Breakeven length:

$$L_{breakeven} = \frac{2P_{\text{plug,injected}}}{P_{\text{fusion per m}}} \quad (\text{A.115})$$

phil: Cary's spreadsheet solves for L_{cc} given Q but we probably won't want Q directly in the cost function since we'll be optimizing for dollar cost or something else that depends on Q .

Central cell length:

$$L_{cc} = Q \cdot L_{breakeven} \quad (\text{A.116})$$

Total fusion power (MW):

$$P_{\text{total}} = 2P_{\text{plug}} + L_{cc} P_{\text{fusion}} \quad (\text{A.117})$$

A.6.5 Overall power balance and plant power estimates

Total electric power in:

$$P_{\text{electric,in}} = \eta_{ECH} P_{ECH} + \eta_{NBI} P_{NBI} + \eta_{RF} P_{RF} \quad (\text{A.118})$$

Recirculating power:

$$P_{\text{recirculating}} = \eta_{DEC} (P_{\text{fusion,charged}} + P_{cc,i,\text{endloss}} + P_{\text{plug,i,endloss}}) \quad (\text{A.119})$$

Thermal power, ignoring power generated by the blanket (the last term is thermal losses caused by DEC inefficiencies):

$$P_{\text{thermal}} = P_{\text{fusion,neutrons}} + (1 - \eta_{DEC}) \left(\frac{P_{\text{recirculating}}}{\eta_{DEC}} \right) \quad (\text{A.120})$$

Net electric power:

$$P_{\text{electric,net}} = -P_{\text{electric,in}} + P_{\text{recirculating}} + \eta_{\text{thermal}} P_{\text{thermal}} \quad (\text{A.121})$$

Q electric:

$$Q_{\text{electric}} = \frac{P_{\text{recirculating}} + \eta_{\text{thermal}} P_{\text{thermal}}}{P_{\text{electric,in}}} \quad (\text{A.122})$$

A.6.6 Instabilities

DCLC ratio (need to keep $\sim 1,000$) [?, ?]:

$$\text{DCLC ratio} = \left(\frac{f_{pi}}{f_{ci,D}} \right)^2 \quad (\text{A.123})$$

The DCLC ratio must be kept $\sim 1,000$ as the radial density gradient needed to trigger the DCLC instability is very small ($I_{\text{gradient}} < 0.01\rho_{g,i}$ for stability). The above condition keeps the plasma radius large enough to prevent radial gradients that are sharper than those needed to trigger the DCLC instability from forming.

Interchange growth rate (s^{-1}):

$$\gamma_{\text{interchange}} = \frac{v_{Ti}}{L_p} \quad (\text{A.124})$$

Electron temperature gradient... something problem: need to understand

$$\chi_{\text{ETG}} = 0.1 \frac{T_{cc,e}^{3/2}}{B_{cc}} \quad (\text{A.125})$$

$$\tau_{\text{ETG}} = \frac{a_{cc}^2}{\chi_{\text{ETG}}} \quad (\text{A.126})$$

A.7 Costs and economics

A.7.1 Heating

problem: Citations needed

ECH: \$10/W

RF: \$1/W

NBI: \$5/W

A.7.2 Magnets

problem: Citations needed

kA-turns of coil needed for a given field and radius:

$$I_{\text{kA-turns}} = \frac{2 \cdot B \cdot a}{1000 \cdot \mu_0} \quad (\text{A.127})$$

kA-m of superconductor needed:

$$S = 2\pi R \cdot I_{\text{kA-turns}} \quad (\text{A.128})$$

Cost per kA·m = 10^{-4} M\$ / kA·m

Cost of magnet = $S \cdot (\text{cost per kA}\cdot\text{m})$

Radii of magnet coils needed: phil: The numbers below are from Cary's spreadsheet. I can't quite follow the thought process that went into these – the ones with my highlight are the quantities I'm using. problem: Rethink and justify these.

1. Mirror: $r_{\text{bore}} + d_{\text{vv}}$ (0.1m) + d_{blanket} (0.6m)

phil: $r_{\text{bore}} \cdot a_{\text{wall, ratio}} + d_{\text{vv}}$ (0.1m) + d_{blanket} (0.6m)

2. Plug midplane: $(a_{\text{wall, ratio}} \cdot a_{\text{plasma}}) + d_{\text{blanket}} + d_{\text{vv}}$ (0.2m)

phil: This will need to change depending on the length of the plug: we may need a solenoid or Maxwell coil instead of just a simple coil to keep

3. Plug divertor: beta limit + 0.2 problem: Doesn't make sense – ignoring for now

4. Central cell: $(a_{\text{wall, ratio}} \cdot a_{\text{plasma}}) + d_{\text{blanket}}$

phil: $(a_{\text{wall, ratio}} \cdot a_{\text{plasma}}) + d_{\text{vv}} + d_{\text{blanket}}$

For the central cell solenoid we are assuming a spacing of one coil per meter for diagnostic access. This is an adjustable parameter but will not be optimized because that would require energetic particle confinement estimates for coil ripple. For reference, the MARS study [LPG] had 42 central cell magnets spaced 3.16m apart with an inner radius of roughly 2m which led to 6% field ripple, which I assume is tolerable.

1. Solenoid field: $B = \mu_0 \cdot n_{\text{cc,turns}} \cdot I$, where $n_{\text{cc,turns}}$ is number of turns per coil. This becomes

$$B = \mu_0 \cdot I_{\text{kA-turns}}$$

2. kA-m per meter length (or per coil): $S_{\text{cc}} = 2\pi a_{\text{cc}} \cdot \frac{B}{\mu_0} \cdot (1/\text{coil spacing})$

A.8 Optimization constraints

phil: This method doesn't work for constraining the minimum field!

A.8.1 Midplane fields regularization via alpha particle confinement penalties

If we do not regularize field strengths, then the optimizer will bring the central cell (or plug) magnetic fields to 0 or negative. Only the midplane fields of the central cell and plugs will be regularized because the cost functions of interest tend towards higher reactor performance (and/or lower cost), and thus higher mirror ratios (and less HTS tape). The vacuum vessel should be, at minimum, four alpha gyroradii across. If an alpha is produced in the core, it will reach a distance

of two gyroradii if all the energy is perpendicular to the field (aside: this is more likely with spin-polarized fuels). Doubling the vacuum vessel radius to four alpha gyroradii is the safer bet. The 3.5 MeV alpha gyroradius is:

$$r_{\text{Larmor}} = \frac{\sqrt{2mE_{\perp}}}{2eB} = \frac{0.2694\text{cm}}{B} \quad (\text{A.129})$$

This regularization is enforced as a penalty coefficient on charged particle fusion power as an exponential function of the vessel wall:

$$\mathcal{C}_{\text{power penalty}} = \begin{cases} e^{a_{\text{diff}}/r_{\text{Larmor}}} & \text{if } a_{\text{diff}} > 0 \\ 1.0 & \text{otherwise} \end{cases} \quad (\text{A.130})$$

where a_{diff} is the difference between the vessel wall and 4 alpha gyroradii: $a_{\text{diff}} = 4r_{\text{Larmor}}$, 3.5 MeV alphas – a_{vv} . These particle losses depend on the radial plasma profile and should be simulated and implicitly affect the optimization instead of the explicit penalty as done here. Only the 3.5 MeV alpha gyroradius is considered because it's the largest of all the usual fusion products but we apply the penalty to all fusion products. This penalty aims to be a conservative estimate.

A.8.2 Kunal's suggestions

Kunal: If we want to pursue Cary's NBI only reactor design concept, then we need to use $\geq 100\text{keV}$ beams since the DT reaction cross section peaks at a center of mass energy of $\sim 65\text{keV}$. Currently, Cary is using 1MeV beams in his code.

I think we should just assume we are shooting for something that is Q=10 and has a usable power out of 200MW. This should stop our coding analysis from making something dumb like a Q=1,000 reactor which has a total power out of 5W by just using a very low beam current.

Cary calculates a lot of stuff with regards to the growth rate of various instabilities. Do we have/want to take all/some of the them into account in our optimization? For example, keeping the DCLC parameter at 1,000,

Per Kunal's suggestion we'll be operating under the following constraints:

1. Minimum usable power out- 200MW
2. Maximum NBI energy- 1MeV
3. Maximum Central cell length- 300m
4. Maximum plasma radius- 0.6m
5. Maximum field strength- 25T
6. Maximum beta- 0.8
7. Minimum DCLC ratio- 1000

These constraints will be soft either a quadratic or exponential penalty for exceeding them so that the cost function is differentiable.

A.9 Optimizing mirror configurations

A.9.1 Gradient descent using SymPy and JAX

Optimization is performed via gradient descent, that is, taking the gradient of some cost function \mathcal{C} with respect to some input parameter vector \vec{x} :

$$\vec{x} := \vec{x} - \nabla_{\vec{x}} \mathcal{C} \cdot \lambda \quad (\text{A.131})$$

where λ is the step size. Specific input values can be frozen by multiplying the gradient by a mask.

Equations are defined in SymPy, which are then lambdified to JAX expressions and then compiled by JAX's just-in-time (JIT) compiler on first run, or when `jax.jit` is called. JAX [jax] calculates the gradients of \mathcal{C} with respect to \vec{x} automatically. The step size λ may be tuned; larger step sizes may not be able to be used because propagating gradients through exponential functions in the temperature calculations can be unstable. We also use 64-bit floats so that large values of α (in the reduced temperature model from Egedal 2022 [?]) remain calculable.

A.9.2 Example: optimizing Q in a simple mirror

As an example of a simple optimization task, we optimize to increase the Q of a simple mirror with classical radial transport. In this case, Q is just fusion power over NBI and ECH power. ECH power is only used to replace Bremsstrahlung and electron cyclotron losses to maintain self-consistent temperatures without requiring iterative solving. D-D fusion products are assumed to be burned instantly, though this only increases fusion power by roughly 7%.

Because the optimal solution is to decrease B_p until the mirror ratio explodes, we will add a $1/B_p$ penalty term to keep values reasonable. The cost function is then:

$$\mathcal{C} = -Q + 1/B_p \quad (\text{A.132})$$

This cost function has no meaningful physical interpretation.

For this optimization case, we hold constant auxiliary heating power ($p_{aux} = 0$ MW), plasma beta ($\beta = 0.8$), mirror bore radius ($r_b = 0.25$ m), length ($L_p = 20$ m), tritium fraction ($T_{\text{frac}} = 0.5$), and beam energy ($E_b = 1000$ keV) and optimize only the mirror field (B_{pm} , T) and central (midplane) field (B_p , T). Z_{eff} is assumed to be 1. B_p is initialized to 6 T, and eight different values of B_{pm} are initialized between 7 and 20 T.

In this optimization, the step size λ is set to 1. The optimization was run for 1000 steps which was chosen arbitrarily it doesn't converge in that step range (and we don't expect it to in this case).

Plots of the cost function \mathcal{C} and the gradient L2 norm for each different configuration can be seen in fig. A.4. The effects of the optimization on the fields B_{pm} and B_p can be seen in fig. A.5. The optimization favors lowering B_p until the regularization cost becomes significant at around step 60. The dramatic increase in mirror ratio leads to greater axial confinement, which decreases NBI current and power, leading to increased Q and decreased fusion power. Plots of Q and fusion power can be seen in fig. A.6. The effects of this optimization on the temperatures (or average energy in the ion case) can be seen in fig. A.7. The increased confinement time allows the beam ions more time to slow on the background electrons, decreasing T_i and increase T_e . The decreased T_i decreases D-D reactivity but *increases* D-T reactivity at a faster rate, leading to

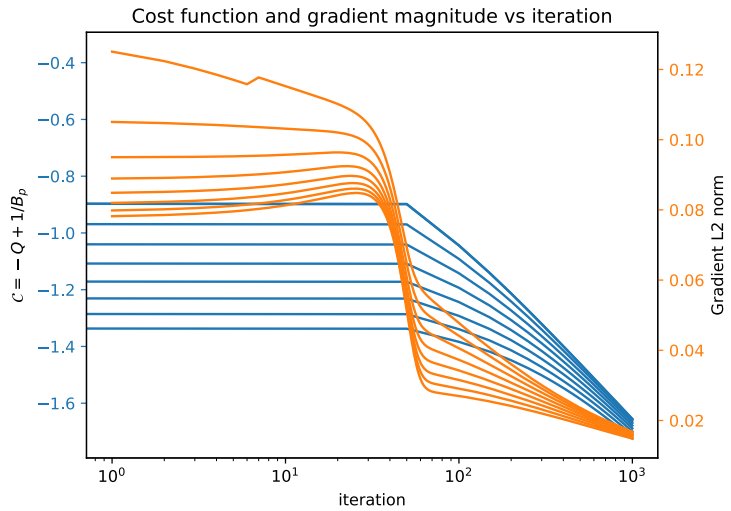


Figure A.4: The cost function and gradient magnitude for each optimization step.

higher fusion power. However, the lower density caused by the lower midplane field (as mandated by the β limit) causes a net *decrease* in fusion power. phil: The increased axial confinement time implies increased confinement of fusion alphas. The estimated total fuel burnup fraction $f_{\text{burnup}} = \frac{2R_x(\text{DT+DD})}{\frac{dN}{dr} + 2R_x(\text{DT+DD})}$ is 24% which may lower fusion power by roughly 42% (since the density would be 24% lower?). Something to think about.

Two insights can be gleaned from this simplified optimization task. Firstly, given optimistic physics, excessively high beam energies, incredibly high field strengths, and ignored impurity and ash accumulation, the reactor still only tops out at Q of around 2.3. This low Q implies that simple mirrors will never be a viable source of electricity. Secondly, Q is a shockingly bad optimization target because it maximizes fusion power *and* minimizes heating power simultaneously, thus high Q's can be obtained at low fusion power as demonstrated here. An expensive, low-power reactor is not useful.

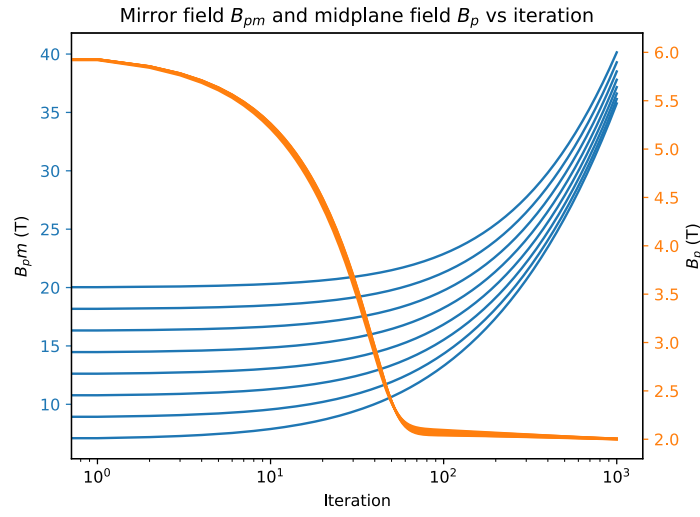


Figure A.5: The mirror and midplane fields for each optimization step. Note the logarithmic x-axis the rate of increase of the mirror field B_{pm} with respect to optimization step decreases with iteration.

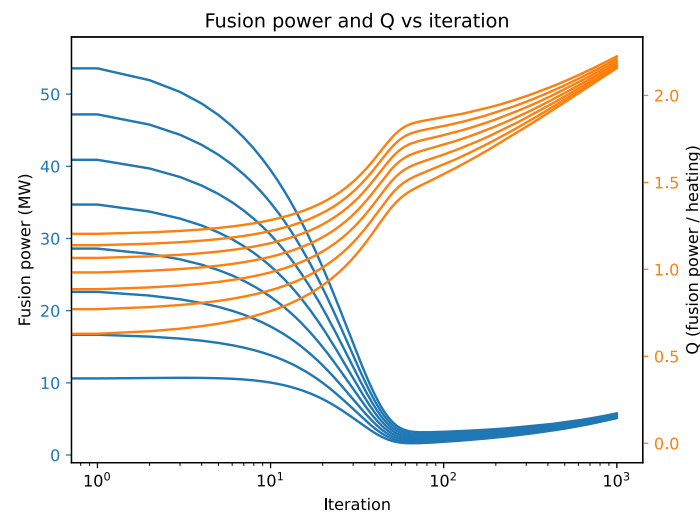


Figure A.6: The total fusion power and Q for each optimization step.

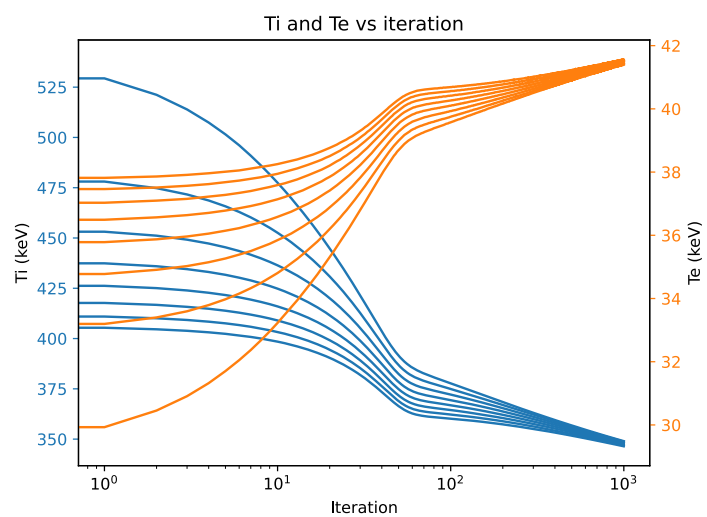


Figure A.7: The ion and electron temperatures for each optimization step

APPENDIX B

Automated Langmuir sweep analysis using machine learning

APPENDIX C

Wisdom acquired

1. Simple stuff goes a long way. Try it first
2. Listen to your advisor
3. Write up as you go along. It helps with the thinking too
4. Wrap up projects (or at least get them to a terminal state) as soon as possible
5. Get a dog
6. Nothing really matters
7. Have two simultaneous projects ongoing, not more, not less
8. Good feedback is hard to find. Seek it out
9. Take risks (see item 6)
10. Don't do solo projects
11. Make lots of friends
12. When life gives you lemons, give them to Mel to make lemon bars

REFERENCES

- [BBC10] Alexei D. Beklemishev, Peter A. Bagryansky, Maxim S. Chaschin, and Elena I. Soldatkina. “Vortex Confinement of Plasmas in Symmetric Mirror Traps.” *Fusion Science and Technology*, **57**(4):351–360, May 2010.
- [BBS07] P.A. Bagryansky, A.D. Beklemishev, and E.I. Soldatkina. “Influence of Radial Electric Field on High-Beta Plasma Confinement in the Gas Dynamic Trap.” *Fusion Science and Technology*, **51**(2T):340–342, February 2007.
- [BGB05] F. Brochard, E. Gravier, and G. Bonhomme. “Transition from flute modes to drift waves in a magnetized plasma column.” *Physics of Plasmas*, **12**(6):062104, June 2005.
- [BKP82] J. M. Beall, Y. C. Kim, and E. J. Powers. “Estimation of wavenumber and frequency spectra using fixed probe pairs.” *Journal of Applied Physics*, **53**(6):3933–3940, 06 1982.
- [BLZ03] P.A. Bagryansky, A.A. Lizunov, A.A. Zuev, E. Yu. Kolesnikov, and A.L. Solomachin. “Experiments with Controllable Application of Radial Electric Fields in GDT Central Cell.” *Fusion Science and Technology*, **43**(1T):152–156, January 2003.
- [BRT91] H. L. Berk, D. D. Ryutov, and Yu. A. Tsidulko. “Temperature-gradient instability induced by conducting end walls.” *Physics of Fluids B: Plasma Physics*, **3**(6):1346–1354, June 1991.
- [CM09] T. A. Carter and J. E. Maggs. “Modifications of turbulence and turbulent transport associated with a bias-induced confinement transition in the Large Plasma Device.” *Physics of Plasmas*, **16**(1):012304, January 2009.
- [CS82] T. A. Casper and Gary R. Smith. “Observation of Alfvén Ion-Cyclotron Fluctuations in the End-Cell Plasma in the Tandem Mirror Experiment.” *Phys. Rev. Lett.*, **48**:1015–1018, Apr 1982.
- [CYK05] T. Cho, M. Yoshida, J. Kohagura, M. Hirata, T. Numakura, H. Higaki, H. Hojo, M. Ichimura, K. Ishii, K. Md. Islam, A. Itakura, I. Katanuma, Y. Nakashima, T. Saito, Y. Tatematsu, M. Yoshikawa, Y. Kojima, S. Tokioka, N. Yokoyama, Y. Tomii, T. Imai, V. P. Pastukhov, and S. Miyoshi. “Observation of the Effects of Radially Sheared Electric Fields on the Suppression of Turbulent Vortex Structures and the Associated Transverse Loss in GAMMA 10.” *Physical Review Letters*, **94**(8):085002, March 2005.
- [EAB23] D. Endrizzi, J.K. Anderson, M. Brown, J. Egedal, B. Geiger, R.W. Harvey, M. Ialovega, J. Kirch, E. Peterson, Yu.V. Petrov, J. Pizzo, T. Qian, K. Sanwalka, O. Schmitz, J. Wallace, D. Yakovlev, M. Yu, and C.B. Forest. “Physics basis for the Wisconsin HTS Axisymmetric Mirror (WHAM).” *Journal of Plasma Physics*, **89**(5):975890501, October 2023.

- [EPC09] E. T. Everson, P. Pribyl, C. G. Constantin, A. Zylstra, D. Schaeffer, N. L. Kugland, and C. Niemann. “Design, construction, and calibration of a three-axis, high-frequency magnetic probe (B-dot probe) as a diagnostic for exploding plasmas.” *Review of Scientific Instruments*, **80**(11):113505, November 2009.
- [FAE24] C.B. Forest, J.K. Anderson, D. Endrizzi, J. Egedal, S. Frank, K. Furlong, M. Ialovega, J. Kirch, R.W. Harvey, B. Lindley, Yu.V. Petrov, J. Pizzo, T. Qian, K. Sanwalka, O. Schmitz, J. Wallace, D. Yakovlev, and M. Yu. “Prospects for a high-field, compact break-even axisymmetric mirror (BEAM) and applications.” *Journal of Plasma Physics*, **90**(1):975900101, February 2024.
- [FCU13] B. Friedman, T. A. Carter, M. V. Umansky, D. Schaffner, and I. Joseph. “Nonlinear instability in simulations of Large Plasma Device turbulence).” *Physics of Plasmas*, **20**(5):055704, 05 2013.
- [FKR79] S. Fornaca, Y. Kiwamoto, and N. Rynn. “Experimental Stabilization of Interchange Mode by Surface Line Tying.” *Phys. Rev. Lett.*, **42**:772–776, Mar 1979.
- [FLM06] A. Fasoli, B. Labit, M. McGrath, S. H. Müller, G. Plyushchev, M. Podestà, and F. M. Poli. “Electrostatic turbulence and transport in a simple magnetized plasma.” *Physics of Plasmas*, **13**(5):055902, May 2006.
- [Fri13] Brett Cory Friedman. *Simulation Analysis of Zero Mean Flow Edge Turbulence in LAPD*. PhD thesis, 2013.
- [FWD83] John R. Ferron, Alfred Y. Wong, Guy Dimonte, and Bernard J. Leikind. “Interchange stability of an axisymmetric, average minimum- B magnetic mirror.” *The Physics of Fluids*, **26**(8):2227–2233, August 1983.
- [GH71] G. E. Guest and E. G. Harris. “Flute Stabilization Via Electrostatically Confined Cold Electrons.” *Phys. Rev. Lett.*, **27**:1500–1503, Nov 1971.
- [Gol95] R.J. Goldston. *Introduction to Plasma Physics*. CRC Press, Boca Raton, 1995.
- [GPL16] W. Gekelman, P. Pribyl, Z. Lucky, M. Drandell, D. Leneman, J. Maggs, S. Vincena, B. Van Compernolle, S. K. P. Tripathi, G. Morales, T. A. Carter, Y. Wang, and T. DeHaas. “The upgraded Large Plasma Device, a machine for studying frontier basic plasma physics.” *Review of Scientific Instruments*, **87**(2):025105, February 2016.
- [HBF84] Jr. Hooper, E. B., D. E. Baldwin, T. K. Fowler, R. J. Kane, and W. C. Turner. “Radial transport reduction in tandem mirrors using endwall boundary conditions.” *The Physics of Fluids*, **27**(9):2264–2267, 09 1984.
- [Hor99] W. Horton. “Drift waves and transport.” *Reviews of Modern Physics*, **71**(3):735–778, April 1999.

- [HPC05] W. Horton, Jean C. Perez, Troy Carter, and Roger Bengtson. “Vorticity probes and the characterization of vortices in the KelvinHelmholtz instability in the large plasma device experiment.” *Physics of Plasmas*, **12**(2):022303, February 2005.
- [IP13] A A Ivanov and V V Prikhodko. “Gas-dynamic trap: an overview of the concept and experimental results.” *Plasma Physics and Controlled Fusion*, **55**(6):063001, may 2013.
- [Jas72] D. L. Jassby. “Transverse Velocity Shear Instabilities within a Magnetically Confined Plasma.” *The Physics of Fluids*, **15**(9):1590–1604, September 1972.
- [jax] “JAX: High-Performance Array Computing.”
- [Kan79] B.I. Kanaev. “Stabilization of drift loss-cone instability (DCI) by addition of cold ions.” *Nuclear Fusion*, **19**(3):347, mar 1979.
- [KGL83] J Kesner, MJ Gerver, BG Lane, BD Vey, RE Aamodt, PJ Catto, DA Ippolito, and JR Myra. “Introduction to tandem mirror physics.” 1983.
- [KHS87] Akio Komori, Yoshiya Higuchi, Yusuke Suetsugu, Akira Yonesu, and Yoshinobu Kawai. “Flute Stabilization of a Mirror-Confining Plasma by a Positive Ambipolar Potential.” *Journal of the Physical Society of Japan*, **56**(8):2607–2610, 1987.
- [Lie85] Paulett C. Liewer. “Measurements of microturbulence in tokamaks and comparisons with theories of turbulence and anomalous transport.” *Nuclear Fusion*, **25**(5):543–621, May 1985.
- [LPG] B G Logan, L J Perkins, and J D Gordon. “Mirror Advanced Reactor Study (MARS): executive summary and overview.”
- [MCT07] J. E. Maggs, T. A. Carter, and R. J. Taylor. “Transition from Bohm to classical diffusion due to edge rotation of a cylindrical plasma.” *Physics of Plasmas*, **14**(5):052507, 05 2007.
- [MII91] A. Mase, A. Itakura, M. Inutake, K. Ishii, J.H. Jeong, K. Hattori, and S. Miyoshi. “Control of the radial electric field and of turbulent fluctuations in a tandem mirror plasma.” *Nuclear Fusion*, **31**(9):1725, sep 1991.
- [MM97] J. E. Maggs and G. J. Morales. “Fluctuations associated with a filamentary density depletion.” *Physics of Plasmas*, **4**(2):290–299, February 1997.
- [MMC05] J. E. Maggs, G. J. Morales, and T. A. Carter. “An Alfvén wave maser in the laboratory.” *Physics of Plasmas*, **12**(1):013103, January 2005.

- [PBD06] F. M. Poli, S. Brunner, A. Diallo, A. Fasoli, I. Furno, B. Labit, S. H. Müller, G. Plyushchev, and M. Podestà. “Experimental characterization of drift-interchange instabilities in a simple toroidal plasma.” *Physics of Plasmas*, **13**(10):102104, October 2006.
- [PMC22] Conor Perks, Saskia Mordijk, Troy Carter, Bart Van Compernolle, Stephen Vincena, Giovanni Rossi, and David Schaffner. “Impact of the electron density and temperature gradient on drift-wave turbulence in the Large Plasma Device.” *Journal of Plasma Physics*, **88**(4):905880405, August 2022.
- [Pos87] R.F. Post. “The magnetic mirror approach to fusion.” *Nuclear Fusion*, **27**(10):1579, oct 1987.
- [Pow74] E.J. Powers. “Spectral techniques for experimental investigation of plasma diffusion due to polychromatic fluctuations.” *Nuclear Fusion*, **14**(5):749, nov 1974.
- [PUC10] P. Popovich, M. V. Umansky, T. A. Carter, and B. Friedman. “Analysis of plasma instabilities and verification of the BOUT code for the Large Plasma Device.” *Physics of Plasmas*, **17**(10):102107, October 2010.
- [QGP23] Yuchen Qian, Walter Gekelman, Patrick Pribyl, Tom Sketchley, Shreekrishna Tripathi, Zoltan Lucky, Marvin Drandell, Stephen Vincena, Thomas Look, Phil Travis, Troy Carter, Gary Wan, Mattia Cattelan, Graeme Sabiston, Angelica Ottaviano, and Richard Wirz. “Design of the Lanthanum hexaboride based plasma source for the large plasma device at UCLA.” *Review of Scientific Instruments*, **94**(8):085104, 08 2023.
- [RBC11] D. D. Ryutov, H. L. Berk, B. I. Cohen, A. W. Molvik, and T. C. Simonen. “Magneto-hydrodynamically stable axisymmetric mirrorsa).” *Physics of Plasmas*, **18**(9):092301, 09 2011.
- [Sch13] David Schaffner. *Study of Flow, Turbulence and Transport on the Large Plasma Device*. PhD thesis, 2013.
- [SCR12] D. A. Schaffner, T. A Carter, G. D. Rossi, D. S. Guice, J. E. Maggs, S. Vincena, and B. Friedman. “Modification of Turbulent Transport with Continuous Variation of Flow Shear in the Large Plasma Device.” *Physical Review Letters*, **109**(13):135002, September 2012.
- [SCR13] D. A. Schaffner, T. A. Carter, G. D. Rossi, D. S. Guice, J. E. Maggs, S. Vincena, and B. Friedman. “Turbulence and transport suppression scaling with flow shear on the Large Plasma Device.” *Physics of Plasmas*, **20**(5):055907, May 2013.
- [Sim76] T. C. Simonen. “Measurements of ion cyclotron instability characteristics in a mirror-confined plasma.” *The Physics of Fluids*, **19**(9):1365–1370, 09 1976.

- [TFM09] G R Tynan, A Fujisawa, and G McKee. “A review of experimental drift turbulence studies.” *Plasma Physics and Controlled Fusion*, **51**(11):113001, November 2009.
- [VG06] Stephen Vincena and Walter Gekelman. “Drift-Alfvén wave mediated particle transport in an elongated density depression.” *Physics of Plasmas*, **13**(6):064503, June 2006.
- [VGP11] B. Van Compernolle, W. Gekelman, P. Pribyl, and C. M. Cooper. “Wave and transport studies utilizing dense plasma filaments generated with a lanthanum hexaboride cathode.” *Physics of Plasmas*, **18**(12):123501, 12 2011.
- [WH84] Masahiro Wakatani and Akira Hasegawa. “A collisional drift wave description of plasma edge turbulence.” *The Physics of Fluids*, **27**(3):611–618, 03 1984.
- [WV82] Michael Wickham and Guy Vandegrift. “Curvature-induced interchange mode in an axisymmetric plasma.” *The Physics of Fluids*, **25**(1):52–58, January 1982.
- [YMM10] M. Yoshikawa, Y. Miyata, M. Mizuguchi, N. Imai, H. Hojo, M. Ichimura, T. Kariya, I. Katanuma, Y. Nakashima, R. Minami, H. Shidara, Y. Yamaguchi, Y. Shima, Y. Ohno, F. Yaguchi, and T. Imai. “Use of a Gold Neutral Beam Probe to Study Fluctuation Suppression During Potential Formation in the GAMMA 10 Tandem Mirror.” *Fusion Science and Technology*, **57**(4):312–319, May 2010.